# Advanced mirror concepts for high-precision metrology

DISSERTATION

zur Erlangung des akademischen Grades

doctor rerum naturalium
– Dr. rer. nat. –

vorgelegt dem Rat der Physikalisch-Astronomischen Fakultät
der Friedrich-Schiller-Universität Jena

von Diplom-Physiker Frank Brückner
geboren am 21.08.1981 in Dresden

**Gutachter**

1. **Prof. Dr. Andreas Tünnermann, Friedrich-Schiller-Universität Jena**

2. **Prof. Dr. Ulf Peschel, Friedrich-Alexander-Universität Erlangen-Nürnberg**

3. **Prof. Dr. Connie Chang-Hasnain, University of California, Berkeley**

**Tag der Disputation: 08.02.2011**

# Contents

# 1 Introduction

In fundamental physics increased research activity is currently taking place on opto-mechanical systems in which a light field is coupled via radiation pressure to the dynamics of a mechanical oscillator [1–6]. The surface of the mechanical device provides the interface between the light field and the solid state matter. Opto-mechanical coupling is widely realized by setting up linear Fabry-Perot resonators with the cavity mirrors being the key object of observation. In particular, cavity mirrors for laser radiation are essential as heavy test masses of space-time for the new field of gravitational wave astronomy [6, 7], as mechanical oscillators for targeting the quantum regime of macroscopic mechanical devices [4, 8–10], and for ultra-high-precision optical clocks designed for researching the nature of fundamental constants [11–14]. Current limitations in such fields are set by the general problem of lacking appropriate cavity mirror qualities.

The purpose of cavity mirrors is to repeatedly retro-reflect laser light such that it constructively interferes with the stored cavity field, yielding maximum field amplitudes and providing an output field of highest phase stability. This requires for cavity mirrors with high reflectivity and a geometrically well defined surface profile. If the mirror surface shows statistical fluctuations, for example driven by Brownian motion of the mirror's molecules, the phase fronts of subsequently reflected waves are slightly different and cannot perfectly interfere constructively. This results in a reduced cavity buildup and, in the most severe cases, in changes of the phase of the output laser beam. Any motion of the mirror surfaces, driven by thermal energy, is known as (*Brownian*) *thermal noise* and is currently a major limiting factor in many research fields targeting fundamental questions of nature as mentioned above [15–17].

The best starting point for the fabrication of low thermal noise mirrors is to employ materials such as fused silica or silicon with high intrinsic mechanical quality factors (Q-factors), low thermal expansion coefficients and low absorption of the laser light at cryogenic temperatures. A useful summary of thermal noise relations can be found in Ref. [18]. In order to achieve high reflectivities for high-finesse setups, dielectric multilayer coatings on the substrate's surface are currently employed and reflectivities up to 99.9998 % have been demonstrated [19]. Typical coating layer materials are $SiO_2$ and $Ta_2O_5$. These two materials show very low optical absorption at the prominent laser wavelength of 1064 nm where ultrastable solid state continuous wave laser sources exist [20], and are therefore frequently used in high-precision experiments. However, recent theoretical and experimental research revealed that these coatings reduce the substrate Q-factors and, most severely, lead to a strong inhomogeneous dissipation and therefore to a rapidly increasing Brownian thermal noise level [15, 21–24].

Thus, new concepts are required that simultaneously provide high optical quality and low mechanical loss. One approach being pursued is to design an alternative multilayer system deviating from the classical quarter wave design and containing less $Ta_2O_5$ [25] which causes the major loss contribution [26]. Doping of $Ta_2O_5$ with $TiO_2$ has also been investigated and a reduction of the mechanical loss by a factor of 1.5 was observed [27]. Besides optimizing multilayer stacks [25–27] or trading off coherent thermal noise sources [17, 28], coating reduced or possibly coating free (i.e. monolithic) mirror concepts are of enormous interest. Previous published approaches, such as corner reflectors [29–31] or whispering gallery mode resonators [32, 33], are based on total internal reflection and significant optical path lengths inside a substrate giving rise to absorption and thermorefractive noise resulting from a temperature dependent index of refraction.

In this thesis the capability of so called *surface relief guided-mode resonant waveguide gratings* (**RWGs**) [34–37] is investigated to provide a solution for the demands mentioned above. Such gratings represent a completely alternative approach for reaching high reflectivity and simultaneously ensure low mechanical loss. The coating thermal noise is reduced due to the fact that the (high mechanical quality) substrate carries only a thin single but corrugated high refractive index layer. A coating related reduction of substrate Q-factors should also be greatly avoided as suggested by first experimental results [24]. The focus of earlier work on waveguide grating structures was centered mainly on narrow-band filtering and switching applications [35]. However, Bunkowski *et al.* [38] theoretically investigated such a device, found parameters for a high-reflection waveguide mirror with broad spectral response, and first proposed to use RWGs instead of conventionally coated mirrors for applications as mentioned above.

The second chapter of this thesis will introduce in more detail the origin and characteristics of coating related thermal noise as well as theoretical basics for the treatment of RWGs in a ray picture and by modal methods, respectively. Based on this, the third chapter shows the experimental realization of nonmonolithic RWGs for tantala supported (working at a 1064 nm wavelength) [39] as well as silicon supported (working at a 1550 nm wavelength) configurations. The latter has been considered because within the past few years silicon rather than fused silica was found to be a more promising candidate for the substrate material of choice [40,41] with an absorption of probably less than $10^{-8}\,\mathrm{cm}^{-1}$ at a 1550 nm wavelength [42] and Q-factors of $10^9$ at cryogenic temperatures [43]. Although these approaches reduce the thick dielectric multilayer stack of conventional mirrors to a thin waveguide layer, at least one additional material has to be added still resulting in an increased mechanical loss. On account of this, chapter four and five theoretically as well as experimentally demonstrate two purely monolithic configurations of RWGs that have been first developed within this thesis [44–48]. Besides presenting extensive rigorous design considerations and a successful grating fabrication, this work also shows the results of the first realization of high-finesse Fabry-Perot cavities incorporating RWG based mirrors. Such setups precisely execute the arrangement in the applications envisioned. These experiments were carried out in close collaboration with the University of Hanover, Germany, in the framework of the German Sonderforschungsbereich/Transregio 7. Chapter six will summarize the results of this thesis in terms of comparing the potential of the different RWG configurations and provides an outlook for planned future work.

# 2 The current state of knowledge

The sensitivity of optical high-precision measurements is limited by several sources of noise. One of which is related to the dielectric coating of high-reflectivity cavity mirrors. This chapter will first introduce this variety of noise sources in terms of their individual origin and impact on the measurement sensitivity. As this work is mainly motivated by the German Sonderforschungsbereich/Transregio 7 "Gravitational Wave Astronomy" we will especially focus on noise aspects in the field of gravitational wave detection [6,7]. As a result of this, coating related thermal noise will be a major sensitivity limitation for next-generation gravitational wave antennae especially in the most sensitive mid-frequency detection band, and will be investigated in the second section of this chapter in more detail. This will teach us possible approaches for a coating thermal noise reduction including the replacement of conventional mirrors by resonant grating structures as proposed by this work. The idea of utilizing such structures and their theoretical treatment is presented in the last section of this chapter.

## 2.1 Thermal noise in high-precision metrology

Fabry-Perot cavities are the key components of optical high-precision measurements whose sensitivity is limited by the geometric definition of the mirror surfaces [15–17]. Any statistical surface motion results in changes of the phase of the output laser beam and thus overrides the detection signal. For gravitational wave detection, a surface fluctuation with a certain frequency mimics the passing of a gravitational wave oscillating with this particular frequency. Besides this mirror surface noise, the laser light itself causes noise which is due to its quantum character and known as quantum noise [52]. The several noise sources known to have a major impact on the sensitivity of gravitational wave detection

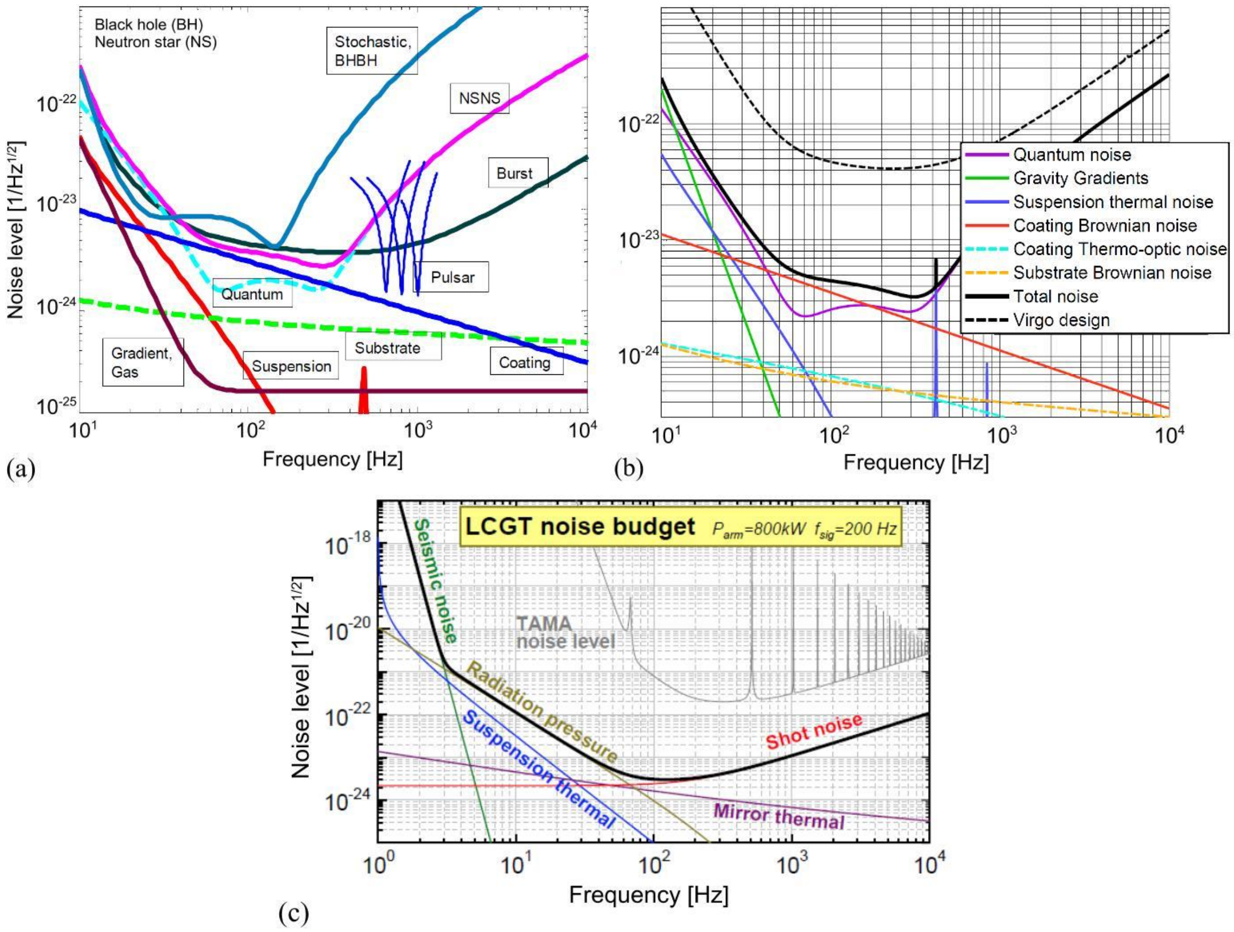

**Fig. 2.1.** Design sensitivity curves for the advanced stages of (a) LIGO (USA) [49] and (b) VIRGO (Italy) [50], and (c) the Japanese gravitational wave antenna LCGT [51]. At low frequencies the sensitivities are limited by seismic noise, at high frequencies by quantum noise and in the mid-detection band by thermal noise.

can be generally classified as follows:

1. Quantum noise (photon shot noise, radiation pressure noise),
2. Seismic noise (seismic motion, gravity gradients),
3. Thermal noise (suspension thermal noise, mirror thermal noise).

Figure 2.1 shows the design sensitivity curves for the advanced stages of the gravitational wave observatories LIGO (USA) [49] and VIRGO (Italy) [50] that are currently set up and the Japanese observatory LCGT [51] that has been recently approved, respectively. Each of these plots reveals three regions that are dominated by different noise sources. For low frequencies the sensitivity is mainly limited by seismic noise that arises from fluctuations in the earth's crust as well as in its gravitational field (gravity gradients) [53]. For frequencies above 150 Hz the curves are governed by quantum noise that is due to the quantum character of the laser light, namely photon shot noise and radiation pressure noise [16, 52]. In the most sensitive mid-detection band the detectors are mainly limited by thermal noise that is driven by thermal fluctuations in the mirror suspensions and mirror test masses [16, 17]. Both plots (a) and (b) already indicate the large impact of coating related thermal noise as being part of the general test mass thermal noise since it is considered separately.

Test mass thermal noise sensed by the circulating laser light at the mirror surface essentially splits into substrate thermal noise and coating thermal noise, each of which splits into Brownian [15,21], thermo-elastic [54] and thermo-refractive noise [55]. Brownian noise stems from any thermally driven motion of the material's molecules and scales linearly with temperature. Any temperature fluctuations in the test mass on the one hand cause local material expansion and compression due to a nonzero thermal expansion coefficient (thermo-elastic noise), and on the other hand result in a local change of the optical path of propagating light due to a temperature dependent index of refraction (thermo-refractive noise). The latter can be neglected for the end test mass substrate itself since the laser light does only interact with the reflecting coated surface.

From the plots (a) and (b) in Fig. 2.1, it can be extracted that the currently used noise models reveal coating noise or rather Brownian coating noise to be the dominant contribution to thermal noise in gravitational wave detection. This applies to most experiments in the field of optical high-precision metrology because of their similar experimental setups. Figure 2.2 exclusively shows the calculated coating thermal noise contribution from an end test mass for Advanced LIGO using current noise models, and was taken from Ref. [56]. As being driven by the same temperature fluctuations, thermo-elastic and thermo-refractive noise can be treated coherently (thermo-optic noise) [56] and are able to compensate to a certain extent [17, 28]. Appearing more critical than that, the dominant source of noise is Brownian motion of the coating materials. This remarkable large impact was found to be dedicated to the large intrinsic mechanical loss of the alternately coated amorphous layers of $SiO_2$ and $Ta_2O_5$ due to internal friction which leads to a strong inhomogeneous energy dissipation [21–24]. This energy dissipation is linked to surface fluctuations via

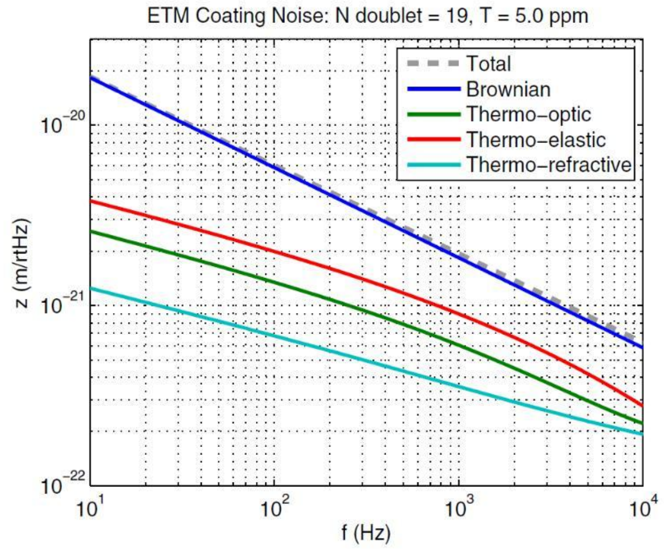

**Fig. 2.2.** Estimated contributions from an Advanced LIGO end test mass (ETM) to the total coating related thermal noise (taken from Ref. [56]). The coherent treatment of thermo-elastic and thermo-refractive noise is known as thermo-optic noise.

the fluctuation-dissipation theorem by Callen and Welton [57], see next section for more detail. In the following a model for the calculation of Brownian noise of a test mass (based on Refs. [15, 21]) is explained which provides all relevant determining factors and, thus, potential approaches for a Brownian noise reduction.

## 2.2 Brownian thermal noise due to dielectric optical coatings

A common way to predict the thermal noise of a test mass is to apply the fluctuation-dissipation theorem [57] which states that the thermal noise power spectrum $S_x(f)$ is proportional to the real part of the mechanical admittance $Y(f)$ of the test mass:

$$S_x(f) = \frac{k_B T}{\pi^2 f^2} \left|\mathrm{Re}\left[Y(f)\right]\right|, \tag{2.1}$$

where $k_B$ is Boltzman's constant, $S_x$ is the spectral density of the thermally induced fluctuations of the test mass surface as read by the laser, $T$ is the temperature of the test mass and $f$ is the frequency of the fluctuations. Levin first proposed to understand the quantity $Y(f)$ as the complex mechanical admittance of the test mass to a generalized Force $F(t)$ having the same spatial distribution as the intensity profile of the interferometer beam [15]:

$$Y(f) \equiv 2\pi i f x(f)/F(f), \tag{2.2}$$

where $x(f)$ is the amplitude of the steady state displacement response. This complex admittance and thus $S_x(f)$ can be calculated by applying a certain cyclic pressure distribution having the same form as the beam profile. For a cyclic force such as $F(t) = F_0 \times \sin(2\pi f t)$, the real part of the mechanical admittance becomes $|\mathrm{Re}\,[Y(f)]| = 2W_{\mathrm{Diss}}/F_0^2$ and describes the coupling of the test mass dissipation to the observable $x(f)$. The power $W_{\mathrm{Diss}}$ is the power that the oscillatory force feeds into the test mass, and that is then dissipated by the test mass. Substituting into Eq. (2.1), we get

$$S_x(f) = \frac{2k_BT}{\pi^2 f^2}\frac{W_{\mathrm{Diss}}}{F_0^2}. \tag{2.3}$$

In order to compute the test mass thermal noise spectral density one needs to work out the average dissipated power $W_{\mathrm{Diss}}$ (under the action of an oscillatory force $F(t)$) which is determined by the mechanical loss angle $\Phi(f)$ of the test mass response to this applied force:

$$W_{\mathrm{Diss}} = 2\pi f U \Phi(f). \tag{2.4}$$

$U$ is the maximum elastic energy stored in the test mass as a result of the excitation at frequency $f$. The loss angle $\Phi$ depends on both, the distribution of losses in the test mass and the deformation of the test mass in response to the applied pressure. If the distribution of losses in the test mass were homogeneous, the loss angle $\Phi$ would be independent of the deformation of the test mass. In that case we could obtain $\Phi$ by simply measuring the loss angle $\Phi = 1/Q$ of a resonant mode of the test mass with $Q$ the mechanical quality factor of this mode. However, due to a strong localized pressure virtually applied to the test mass surface and lossy amorphous materials at this surface, the distribution of losses is strongly inhomogeneous and the easy approach does not work. For a more realistic thermal noise prediction, we must therefore assume the test mass loss angle $\Phi$ to be a sum of the homogeneous and isotropic substrate loss angle $\Phi_{\mathrm{Sub}}$ and the coating loss $\Phi_{\mathrm{Coat}}$. For a loss in the coating being homogeneous and isotropic, yet different from that of the substrate, $\Phi$ becomes

$$\Phi(f) = \Phi = \frac{1}{U}(U_{\mathrm{Sub}}\Phi_{\mathrm{Sub}} + U_{\mathrm{Coat}}\Phi_{\mathrm{Coat}}), \tag{2.5}$$

with $U_{\mathrm{Sub}}$ and $U_{\mathrm{Coat}}$ the portions of the stored energy $U$ in the substrate and the coating, respectively. To simplify the calculation of the energies we assume a force distribution that is constant in time $F(t) = F_0$. This assumption is justified due to the fact that the frequencies where thermal noise dominates interferometer noise budgets are far below the first resonances of the test masses. Since we are in the limit where the coating thickness $h$ is very thin compared to the beam radius and thus the pressure distribution, $U_{\mathrm{Coat}} \approx \delta U h$ with $\delta U$ the energy stored at the test mass surface, integrated over the surface [21]. In accordance, $U_{\mathrm{Sub}} \approx U$ which reformulates Eq. (2.5) to

$$\Phi = \Phi_{\mathrm{Sub}} + \frac{\delta U h}{U}\Phi_{\mathrm{Coat}}. \tag{2.6}$$

However, in reality the coating loss angle will be anisotropic due to its layered structure. Thus, the second term in Eq. (2.6) needs to be expanded by considering a loss angle associated with the energy density in parallel coating strains $\Phi_{\|}$ and a loss angle associated with the density of energy in perpendicular coating strains $\Phi_{\perp}$. The stored energy in the coating $\delta U$ accordingly splits into a portion parallel to the coated surface $\delta U_{\|}$ and a portion perpendicular to the coated surface $\delta U_{\perp}$. Taking the anisotropic layer structure of the coating into account, Eq. (2.6) is replaced by

$$\Phi = \Phi_{\mathrm{Sub}} + \frac{\delta U_{\|} h}{U}\Phi_{\|} + \frac{\delta U_{\perp} h}{U}\Phi_{\perp}. \tag{2.7}$$

In order to obtain an expression for $\Phi$ we need to calculate $\delta U_{\|}$, $\delta U_{\perp}$ and $U$. For this we assume a Gaussian beam profile as proposed to be used in the Advanced gravitational wave detectors:

$$f(r) = \frac{2}{\pi r_0^2} \times \exp\left(\frac{-2r^2}{r_0^2}\right), \tag{2.8}$$

with $r_0$ the beam radius where the light intensity is $1/e^2$ of the maximum. To be a good approximation this beam radius is small compared to the radius of the test mass (to ensure low enough clipping losses of typ. $< 1\,\mathrm{ppm}$), and we can assume a coated half-infinite test mass which is subject to this Gaussian pressure distribution. The stored energies can now be calculated by solving the axially symmetric equations of elasticity which has been done explicitly by Harry *et al.* in 2002 [21]. For a thin coating ($h \ll r_0$) and provided the Poisson's ratio of the coating is not very different from that of the substrate ($\sigma \approx \sigma'$), his calculations resulted in

$$U = \frac{F_0^2(1-\sigma^2)}{2\sqrt{\pi} r_0 E}, \tag{2.9}$$

$$\delta U_{\parallel}/U = \frac{1}{\sqrt{\pi} r_0} \frac{E'(1+\sigma)(1-2\sigma)^2 + E\sigma'(1+\sigma')(1-2\sigma)}{E(1+\sigma')(1-\sigma')(1-\sigma)}, \tag{2.10}$$

$$\delta U_{\perp}/U = \frac{1}{\sqrt{\pi} r_0} \frac{E(1+\sigma')(1-2\sigma') - E'\sigma'(1+\sigma)(1-2\sigma)}{E'(1-\sigma')(1+\sigma)(1-\sigma)}, \tag{2.11}$$

where $E$, $E'$ and $\sigma$, $\sigma'$ are the Young's moduli and Poisson's ratios of the substrate and the coating, respectively. At this stage, the parameters $E'$ and $\sigma'$ of the coating are assumed to be isotropic and the values for the current coating materials $SiO_2$ and $Ta_2O_5$ to be similar. This means that the alternating coating of thickness $h$ in reality is approximated here by just one layer of the same thickness. A correct treatment can be found in Ref. [27] by summing all individual coating values to effective ones. However, our approximation will also provide all essential physics. Substituting Eqs. (2.9), (2.10) and (2.11) into Eq. (2.7) and the result of this together with Eq. (2.9) into Eq. (2.4) gives a new expression for the dissipated power $W_{\mathrm{Diss}}$ under the application of a Gaussian pressure distribution. By a final substitution into the fluctuation-dissipation theorem (Eq. (2.3)) we obtain the power spectral density of the interferometer test mass displacement Brownian thermal noise:

$$\begin{aligned} S_x(f) &= \frac{2k_BT}{\pi^{3/2}f}\frac{1-\sigma^2}{r_0E}\Bigg\{\Phi_{\mathrm{Sub}} + \frac{h}{\sqrt{\pi}r_0}\frac{1}{EE'(1-\sigma'^2)(1-\sigma^2)} \\ &\times \Big[E'^2(1+\sigma)^2(1-2\sigma)^2\Phi_{||} + EE'\sigma'(1+\sigma)(1+\sigma')(1-2\sigma)(\Phi_{||}-\Phi_{\perp}) \\ &+ E^2(1+\sigma')^2(1-2\sigma')\Phi_{\perp}\Big]\Bigg\}. \end{aligned} \tag{2.12}$$

As a matter of fact, this equation is valid only for a major loss contribution that is due to internal friction of the coating materials themselves, and not due to interfacial rubbing between the coating and the substrate, or to rubbing between the coating layers. As the Poisson's ratios of the currently used substrate and coating materials are quite small ($\sigma' \leq 0.25$), Eq. (2.13) is reasonably approximated by setting $\sigma = \sigma' = 0$ and becomes:

$$S_x(f) = \frac{2k_BT}{\pi^{3/2}f}\frac{1}{r_0E}\left\{\Phi_{\mathrm{Sub}} + \frac{h}{\sqrt{\pi}r_0}\left(\frac{E'}{E}\Phi_{||} + \frac{E}{E'}\Phi_{\perp}\right)\right\}. \tag{2.13}$$

As stated above and displayed in the plots of Fig. 2.1, Brownian thermal noise from the substrate itself is less serious than that caused by the coating. We skip this term in Eq. (2.13) and end up with the following expression that can teach us all essential physics of coating related Brownian thermal noise:

$$S_x(f)_{\mathrm{Coat}} = \frac{2k_BTh}{\pi^2 f r_0^2 E}\left(\frac{E'}{E}\Phi_{||} + \frac{E}{E'}\Phi_{\perp}\right). \tag{2.14}$$

Equation (2.14) shows that, in order to explicitly estimate the Brownian thermal noise level of a particular coating, we need to know the material parameters $E$, $E'$, $\Phi_{||}$ and $\Phi_{\perp}$. It also states that for $\Phi_{||} \approx \Phi_{\perp}$ the minimum thermal noise can be reached if the Young's modulus of the coating is matched to that of the substrate. For nonmatched Young's moduli, one of the loss contributions $\Phi_{||}$ or $\Phi_{\perp}$ will be more dominant than the other.

Besides researching coating materials with optimized material parameters and lower mechanical loss [26, 27, 58], Eq. (2.14) provides us further fundamental approaches for a coating thermal noise reduction as $S_x(f)$ also scales with the temperature $T$, the square of the beam radius $r_0^2$, and the coating thickness $h$. The former is planned to be addressed by operating future detectors at cryogenic temperatures. However, the impact of such an environment on the mechanical loss angle of the coating materials is still under investigation [26,58]. Previous results unfortunately indicate a mechanical loss increase with lower temperatures [26]. As larger beam radii suggest lower thermal noise one could simply propose to use larger Gaussian beams. However, this would simultaneously cause larger test mass substrates. Essentially maintaining both, the substrate size and the laser light power, Chelkowski *et al.* proposed to utilize Laguerre-Gauss modes instead of conventional Gauss beams which more homogeneously distribute the laser light over the mirror surface [59].

Finally, the coating thickness $h$ is a crucial factor. One approach being pursued for a coating thickness reduction is to design alternative multilayer systems deviating from the classical quarter wave design and containing less $Ta_2O_5$ [25] which causes the major loss contribution. However, coating reduced or possibly coating free (i.e. monolithic) mirror concepts are of enormous interest. Previous published approaches such as corner reflectors [29–31] or whispering gallery mode resonators [32,33] are based on total internal reflection and significant optical path lengths inside a substrate giving rise to absorption and thermorefractive noise resulting from a temperature dependent index of refraction. The same applies to double or etalon mirrors proposed by Khalili [60]. Within this work we propose to employ guided-mode resonant waveguide gratings as an alternative to conventionally coated mirrors ($h \approx 7\,\mu$m). This suggests a remarkable Brownian thermal noise reduction since they work only with a thin but corrugated dielectric layer ($h \approx$ few hundred nanometers) or even without any dielectric coating ($h = 0\,$nm, see chapter 4) to reach high reflectivity.

## 2.3 Guided-mode resonant waveguide gratings (RWGs)

Resonant waveguide grating structures employ resonant light coupling instead of multiple interference at different layer interfaces to achieve high reflectivity and therefore represent an alternative mirror concept [34–37]. They comprise a periodically nanostructured high refractive index layer attached to a low refractive index substrate. The fundamental principle of waveguide gratings is illustrated in Fig. 2.3(a) and can be understood by a simple ray picture [36,61]. In the case of normal incidence, the three following parameter

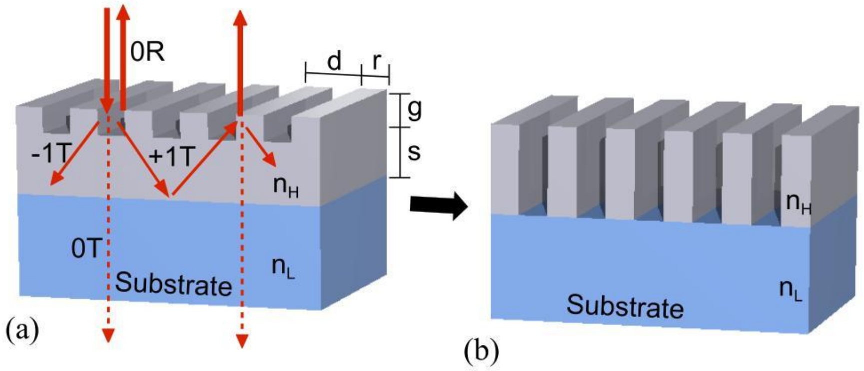

**Fig. 2.3.** (a) Fundamental principle of resonant waveguide gratings in a simplified ray picture which is only valid for a small grating groove depth $g$. Note that in reality the light rays do not correlate with the grating grooves such as suggested in (a). (b) For a groove depth comparable to the waveguide layer thickness $s$ or even vanishing waveguide layer, the ray picture breaks down, see section 2.3.2.

inequalities (which can be derived from the well known grating equation [62]) have to be fulfilled to allow for resonant reflection:

$$d < \lambda \quad \text{(to permit only zeroth order in air)}\,, \tag{2.15}$$

$$\lambda/n_{\mathrm{H}} < d \quad \text{(first orders in high-index layer)}\,, \tag{2.16}$$

$$d < \lambda/n_{\mathrm{L}} \quad \text{(only zeroth order in the substrate)}\,, \tag{2.17}$$

where $d$ is the grating period, $\lambda$ is the light's vacuum wavelength and $n_{\mathrm{H}}$ and $n_{\mathrm{L}}$ are the higher and lower refractive indices, respectively. In this simplified ray picture, the first diffraction orders (-1T, +1T) in the high-index layer experience total internal reflection (at the interface to the low-index substrate) and, thus, excite resonant waveguide modes propagating along the corrugated high-index layer. A part of the light inside the waveguide is coupled out via the grating to both, the transmitted and reflected zeroth order (0T, 0R). If the grating period $d$, the groove depth $g$, the grating fill factor $f$ (ratio between ridge width $r$ and grating period $d$), and the high-index layer thickness $s$ with respect to the refractive index values of the involved materials are designed properly, all transmitted light can be prompted to interfere destructively corresponding to a theoretical 100 % reflectance [36]. A more detailed and quantitative consideration of the phase relations between the rays involved will be provided in the following section.

In contrast to multilayer coated mirrors where perfect reflectivity is possible for an infinite number of dielectric double layers, RWGs can reach reflectivities of exactly 100% if a certain structure is precisely met. This structure corresponds to the condition of complete destructive interference. With decreased coupling efficiency to the waveguide modes the structure behaves more resonant leading to a higher finesse of the single peak reflection spectrum [36]. That property makes such devices suitable for narrowband filtering [35]. However, for applications as mentioned above, a broadband resonance is desired since small deviations from the device's design parameters would dramatically decrease the normal incidence reflectivity for the central wavelength. Additionally, an electric field enhancement inside a high-finesse waveguide might be a problem for high-power laser interferometry due to laser induced damage. The spectral response can be significantly broadened by increasing the diffraction efficiency to the first orders and thus the coupling efficiency to the waveguide modes [61]. This can be done by means of particular grating parameter design and providing a high refractive index contrast between both involved materials, as will also be evident from the following section.

### 2.3.1 Description of RWGs in a ray picture

For our analysis we assume a resonant waveguide grating that comprises a nanostructured high refractive index ($n_\mathrm{H}$) layer attached to a low refractive index ($n_\mathrm{L}$) substrate. The device is surrounded by air with $n_0 = 1$. For validity of the following considerations, the groove depth of our grating $g$ is assumed to be much smaller than the wavelength $\lambda$ and the waveguide thickness $s$: $g \ll \lambda, s$. The geometry and ray propagation in our basic RWG is illustrated in Fig. 2.4. The incident plane wave with the wave vector $k_0$ impinging under an angle of incidence $\theta_0 \neq 0$ at point A is partly transmitted ($k_{\mathrm{H},0}$) with refraction angle $\theta_{\mathrm{H},0}$ and partly diffracted ($k_{\mathrm{H},+1}$) with diffraction angle $\theta_{\mathrm{H},1}$ according to the grating equation

$$n_\mathrm{H} \cdot \sin\theta_{\mathrm{H,m}} = n_0 \cdot \sin\theta_0 + m \cdot \frac{\lambda}{d} \tag{2.18}$$

with m = 1. As mentioned above the diffracted beam experiences total internal reflection at point B (if the grating period $d$ fulfills Ineqs. (2.15)-(2.17)) and is sent back to the

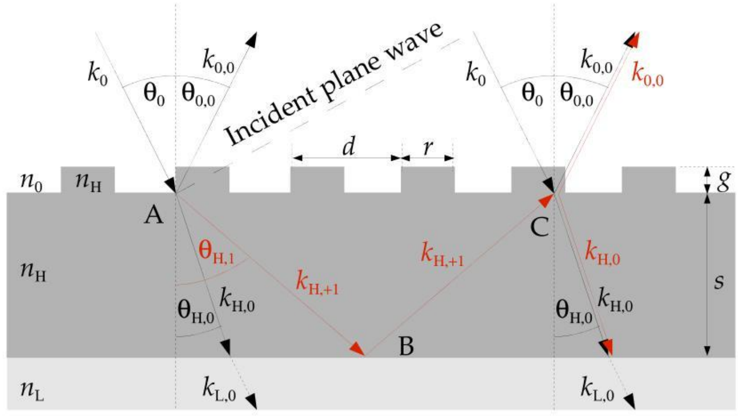

**Fig. 2.4.** Propagation of light rays in a resonant waveguide grating that is illuminated by a plane wave under an angle of incidence $\theta_0 \neq 0$.

grating at point C. This correlates to the excitation of a guided mode. At point C some of the trapped light is diffracted outward by the grating to both the transmitted ($k_{\mathrm{H},0}$) and reflected ($k_{0,0}$) zeroth order as well as experiences total internal reflection (not shown for clarity). Since the corrugation of the waveguide layer causes a certain permanent light dissipation, the guided optical mode needs to be considered as a *leaky* mode [63]. At a specific wavelength and angular orientation of the incident beam the structure resonates; that is, light accumulates in the waveguide and the light diffracted outward has the intensity and the appropriate phase such that complete interference occurs with the directly transmitted portion of the incident beam $k_{\mathrm{H},0}$ and no light is transmitted through the structure. The key feature is the relative phase shift between the incident and the diffracted waves which is calculated in the following.

For resonance, we have to satisfy the phase-matching condition for the propagation of a guided mode with mode number $m$ [64] which is

$$\Phi_{\mathrm{TE/TM}} = m \cdot 2\pi \tag{2.19}$$

with $\Phi_{\mathrm{TE/TM}}$ the accumulated phase during one waveguide circulation of either TE- or TM-polarized light (TE: electric field vector circulating parallel to the grating ridges; TM: electric field vector circulating perpendicular to the grating ridges). For our RWG the accumulated phase for TE- and TM-polarized light is the sum of three terms:

$$\Phi_{\mathrm{TE}} = \Phi_P + \Phi_{\mathrm{TE}}^{\mathrm{HL}} + \Phi_{\mathrm{TE}}^{\mathrm{H0}}, \tag{2.20}$$

$$\Phi_{\mathrm{TM}} = \Phi_P + \Phi_{\mathrm{TM}}^{\mathrm{HL}} + \Phi_{\mathrm{TM}}^{\mathrm{H0}}; \tag{2.21}$$

where $\Phi_P$ is the simple phase accumulation due to light propagation and $\Phi_{\mathrm{TE/TM}}^{\mathrm{HL/HO}}$ are the polarization dependent phase shifts due to total internal reflection at point B and C which is known as the Goos-Hänchen shift [65,66]. These phase shifts can be derived from Fresnel's equations and are in particular for point B [67]:

$$\Phi_{\mathrm{TE}}^{\mathrm{HL}} = -2 \cdot \tan^{-1}\left(\frac{\sqrt{\sin^2\theta_{\mathrm{H},1} - (n_{\mathrm{L}}/n_{\mathrm{H}})^2}}{\cos\theta_{\mathrm{H},1}}\right), \tag{2.22}$$

$$\Phi_{\mathrm{TM}}^{\mathrm{HL}} = -2 \cdot \tan^{-1}\left(\frac{\sqrt{\sin^2\theta_{\mathrm{H},1} - (n_{\mathrm{L}}/n_{\mathrm{H}})^2}}{(n_{\mathrm{L}}/n_{\mathrm{H}})^2 \cdot \cos\theta_{\mathrm{H},1}}\right). \tag{2.23}$$

The phase accumulation due to light propagation $\Phi_P$ can be calculated from the optical path length $P$ inside the waveguide

$$P = 2s \cdot n_{\mathrm{H}} \cdot \cos\theta_{\mathrm{H},1} \tag{2.24}$$

with $s$ the waveguide thickness by multiplying the wave vector $k_0$:

$$\Phi_P = k_0 \cdot P = \frac{4\pi}{\lambda} \cdot n_{\mathrm{H}} \cdot s \cdot \cos\theta_{\mathrm{H},1} = 2k_{\mathrm{H},+1} \cdot s \cdot \cos\theta_{\mathrm{H},1}. \tag{2.25}$$

Using Eqs. (2.22) and (2.23) for point B as well as adapted for point C and Eq. (2.25), the phase accumulation during one waveguide circulation for TE- or TM-polarized light becomes:

$$\begin{aligned}\Phi_{\mathrm{TE}} = \frac{4\pi}{\lambda} \cdot n_{\mathrm{H}} \cdot s \cdot \cos\theta_{\mathrm{H},1} \quad &- \quad 2 \cdot \tan^{-1}\left(\frac{\sqrt{\sin^2\theta_{\mathrm{H},1} - (n_{\mathrm{L}}/n_{\mathrm{H}})^2}}{\cos\theta_{\mathrm{H},1}}\right) \\ &- \quad 2 \cdot \tan^{-1}\left(\frac{\sqrt{\sin^2\theta_{\mathrm{H},1} - (n_0/n_{\mathrm{H}})^2}}{\cos\theta_{\mathrm{H},1}}\right),\end{aligned} \tag{2.26}$$

$$\Phi_{\mathrm{TM}} = \frac{4\pi}{\lambda} \cdot n_{\mathrm{H}} \cdot s \cdot \cos\theta_{\mathrm{H},1} \quad - \quad 2 \cdot \tan^{-1}\left(\frac{\sqrt{\sin^2\theta_{\mathrm{H},1} - (n_{\mathrm{L}}/n_{\mathrm{H}})^2}}{(n_{\mathrm{L}}/n_{\mathrm{H}})^2 \cdot \cos\theta_{\mathrm{H},1}}\right) \quad - \quad 2 \cdot \tan^{-1}\left(\frac{\sqrt{\sin^2\theta_{\mathrm{H},1} - (n_0/n_{\mathrm{H}})^2}}{(n_0/n_{\mathrm{H}})^2 \cdot \cos\theta_{\mathrm{H},1}}\right). \tag{2.27}$$

Due to the double diffraction process at point A and point C each of which is associated with an additional phase shift of $\pi/2$ [68], the relative phase shift between the directly transmitted wave $k_{\mathrm{H},0}$ and the re-transmitted doubly diffracted wave $k_{\mathrm{H},0}$ at resonance is equal to $\pi$ which corresponds to a complete destructive interference. Hence, no light is transmitted to the substrate and the wave $k_{\mathrm{L},0}$ does not carry any intensity. In contrast, the reflected waves $k_{0,0}$ and $k_{0,0}$ are in phase and constructively interfere due to the phase shift of $\pi$ which occurs when the incident wave is directly reflected at point A.

A relatively simple model for analyzing the resonance behavior in RWGs in more detail is based on a multiple interference model similar to that used for analyzing the multiple interference in a Fabry-Perot etalon. In this case the output transmitted and reflected fields are a superposition of all diffracted and outcoupled subwaves. Such a model can help in elucidating the basic mechanisms of the resonance and allows the calculation of the spectral bandwidth of the resonance in these structures. Assuming a grating of infinite size, the transmitted electric field of all interfering subwaves can be written as a geometric series similar to a Fabry-Perot etalon [36, 61]. The ratios of the transmitted $E_T$ and reflected $E_R$ to the incident field amplitudes $E_0$ are as follows:

$$\frac{E_T}{E_0} = 1 - \frac{\eta \cdot e^{i\Delta\Phi}}{1 - (1-\eta) \cdot e^{i\Delta\Phi}}, \tag{2.28}$$

$$\frac{E_R}{E_0} = \frac{\eta \cdot e^{i\Delta\Phi}}{1 - (1-\eta) \cdot e^{i\Delta\Phi}}. \tag{2.29}$$

$\Delta\Phi$ is the polarization dependent dephasing from the phase-matching condition (2.19) introduced by a deviation of the wavelength or the incidence angle from its values at the resonance condition. The parameter $\eta$ with

$$\eta \propto (n_{\mathrm{H}}^2 - n_0^2)^2 \cdot g^2 \tag{2.30}$$

is a polarization independent diffraction coefficient which is correlated to the diffraction efficiency into the first orders exciting the guided mode [36]. The ratio of transmitted to incident intensity $I_T/I_0$ is defined by

$$\frac{I_T}{I_0} = \left(\frac{E_T}{E_0}\right) \cdot \left(\frac{E_T}{E_0}\right)^* = \frac{4(1-\eta)\cdot \sin^2(\Delta\Phi/2)}{\eta^2 + 4(1-\eta)\cdot \sin^2(\Delta\Phi/2)}, \tag{2.31}$$

and gives the correlated relation for the reflected intensity by $I_R = 1 - I_T$:

$$\frac{I_R}{I_0} = \left(\frac{E_R}{E_0}\right) \cdot \left(\frac{E_R}{E_0}\right)^* = \frac{\eta^2}{\eta^2 + 4(1-\eta)\cdot \sin^2(\Delta\Phi/2)}. \tag{2.32}$$

For a small dephasing $\Delta\Phi$, this conforms to a Lorentzian distribution with $\Delta\Phi$ being the dependent variable [69] as illustrated in Fig. 2.5. From Eqs. (2.30) and (2.32) it is evident that the resonance spectral bandwidth of this Lorentzian profile is directly related to the diffraction coefficient $\eta$ in terms of the optical as well as geometrical parameters $n_{\mathrm{H}}$, $n_0$, and $g$. Thus, the resonance spectral bandwidth for given incident wavelength $\lambda$, grating period $d$, and grating fill factor $f$ can be controlled by varying the grating height $g$ and/or the refractive index contrast $\Delta n = n_{\mathrm{H}} - n_0$.

Comparing Eqs. (2.31) and (2.32) with the Airy-functions of a Fabry-Perot (FP) resonator [70], we can find the intensities $I_T$ and $I_R$ of our RWG to be inverted with regard to the Fabry-Perot functions:

$$\left(\frac{I_T}{I_0}\right)_{\mathrm{RWG}} \propto \left(\frac{I_R}{I_0}\right)_{\mathrm{FP}}, \tag{2.33}$$

$$\left(\frac{I_R}{I_0}\right)_{\mathrm{RWG}} \propto \left(\frac{I_T}{I_0}\right)_{\mathrm{FP}}. \tag{2.34}$$

In accordance to a FP resonator we can define a finesse $F$ for a RWG by replacing the reflectivity of the mirrors $R$ by $1 - \eta$:

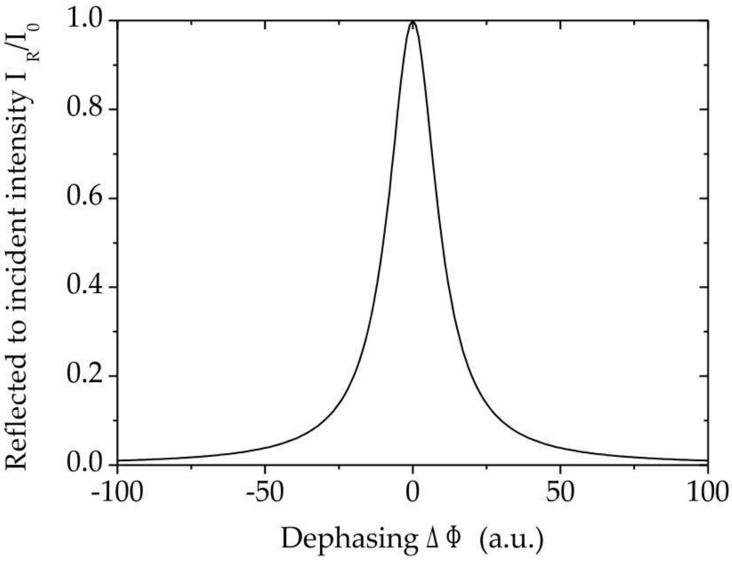

**Fig. 2.5.** Ratio of reflected to incident intensity $I_R/I_0$ as a function of the dephasing from the resonance condition $\Delta\Phi$ for an RWG described in a ray picture.

$$F_{\mathrm{FP}} = \frac{4R}{(1-R)^2} \quad \Rightarrow \quad F_{\mathrm{RWG}} = \frac{4(1-\eta)}{\eta^2}, \tag{2.35}$$

which means the smaller the diffraction efficiency into the first diffraction orders (determined by $\Delta n$ and $g$) the more resonant behaves the RWG leading to a higher finesse $F$ and thus a narrower spectral bandwidth. With the full width at half maximum (FWHM) of the spectral response $\Delta\lambda_{\mathrm{FWHM}}$, Norton *et al.* defined a propagation length of the leaky guided mode at resonance $l_R$ which is typically in the $\mu$m-range and whose reciprocal $\gamma = l_R^{-1}$ is a quantity for the intensity dissipation of the guided mode into the outcoupled diffracted orders [69]:

$$l_R = \gamma^{-1} = \frac{\lambda \cdot d}{\pi} \cdot \frac{1}{\Delta\lambda_{\mathrm{FWHM}}}. \tag{2.36}$$

Please note that for a larger grating depth $g$ such as in the same range as the waveguide thickness $s$ or even for a vanishing waveguide layer thickness (see Fig. 2.3(b)), the simplified ray picture breaks down. However, perfect reflectivity is still possible as will be confirmed by rigorous simulation as well as experimental results in chapter 3. For a theoretical understanding, the diffraction orders involved in the coupling process and described above rather need to be considered as corresponding to discrete grating modes. These modes are propagating through the binary grating region according to the so-called modal method [71].

### 2.3.2 Description of RWGs by the modal method

As outlined in the preceding section, the diffraction problem of RWGs can not be understood by a ray picture once the grating groove depth $g$ reaches dimensions comparable to those of the period $d$ and/or the wavelength $\lambda$. This is due to the fact that for such gratings as shown in Fig. 2.3(b) no diffraction orders exist with respect to their classical definition of propagating light rays. However, for a significant coating thickness reduction, such structures are favorable and will be mainly considered throughout this work. On account of this, we need to make use of a more general theory of diffraction gratings to describe the phenomena of perfect reflection of RWGs: the modal method [71–73]. The basic idea of the modal method is that a plane wave incident upon a deep grating splits into a discrete set of modes propagating in z-direction through the grating region. This is similar to the light propagation in a simple slab waveguide.

Such a slab waveguide is also able to guide a discrete set of modes. The propagation constants of these modes $k_z^m = k_0 \cdot n_{\text{eff}}^m$ with the vacuum wave number $k_0 = 2\pi/\lambda$, or rather their effective indices $n_{\text{eff}}^m$, are characteristics of the waveguide geometry. Modes with $n_{\text{eff}}^2 > 0$ propagate through the waveguide while those with $n_{\text{eff}}^2 < 0$ are evanescent. The more similar the field distributions of the exciting plane wave and the excited mode are at the matching plane, the higher is the excitation efficiency of these modes by the incident field. This *similarity* is expressed by an overlap integral. Furthermore, the difference of the propagation constant of the incident wave $k_{0,z} = k_0 \cdot \cos\theta_0$ relative to $k_z^m$ results in a reflection similar to the Fresnel reflection at the interface of two homogeneous media. Both effects, the overlap and the matching of effective indices, determine how much energy of the incident wave is coupled to a specific mode.

As illustrated in Fig. 2.6, a plane wave incident upon a deep lamellar grating, being nothing else than a periodic waveguide, also excites discrete modes (with x-component $u_m(x)$) comparable to the simple case of a slab waveguide. The efficiency of this excitation,

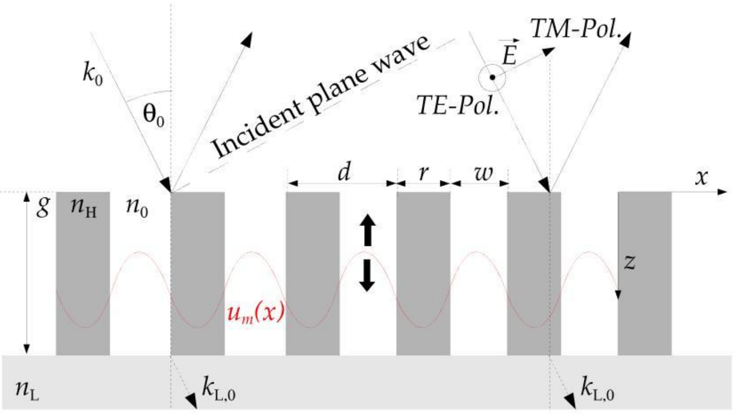

**Fig. 2.6.** Geometry of the diffraction problem of an RWG with zero waveguide layer thickness ($s = 0\,\text{nm}$) and a period $d$ as well as a groove depth $g$ in the range of the wavelength. According to the modal method, an incident plane wave excites discrete grating modes with x-component $u_m(x)$ (schematically illustrated in red) propagating through the grating region instead of diffraction orders.

the up- and downward propagation of the modes through the grating region, and how they couple to the zeroth transmitted diffraction order in the substrate $k_{\text{L},0}$ determine the optical properties of the grating. The propagation constants or effective indices of these modes can be derived according to the following procedure (which is based on Refs. [74, 75]):

Assuming TE-polarized light, the incident plane wave is fully described by an electric field component parallel to the grating ridges in y-direction

$$E_{0,y}(x,z) \propto \exp\left[-ik_0(x \cdot \sin\theta_0 + z \cdot \cos\theta_0)\right]. \tag{2.37}$$

Because of the geometry of the diffraction problem as displayed in Fig. 2.6, the electric field inside the grating region does only have a y-component as well that can be separated into a x-dependent and a z-dependent part:

$$E_y^{grat}(x,z) = u(x) \cdot v(x), \tag{2.38}$$

each of which fulfills the Helmholtz equation for homogeneous media in the grating grooves as well as in the grating ridges. For the z-part it reads

$$\left(\frac{\partial^2}{\partial z^2} + k_z^2\right) v(z) = 0 \tag{2.39}$$

and similar for the x-part

$$\left(\frac{\partial^2}{\partial x^2} + k_{i,x}^2\right) u(x) = 0, \tag{2.40}$$

where $k_{i,x}^2 = k_i^2 - k_z^2$ ($i = r$ in the ridge, $i = w$ in the groove) with $k_i = n_i \cdot k_0$, the wave number in the ridge or the groove, respectively. The propagation constant $k_z = k_0 \cdot n_{\text{eff}}$ is equal in both media. Equations (2.39) and (2.40) can be generally solved in the ridges or the grooves by

$$u_i(x) = A \cdot \cos(k_{i,x}x) + B \cdot \sin(k_{i,x}x). \tag{2.41}$$

Considering the field continuity conditions at the boundaries between the ridges and the grooves results in a transcendent equation for the propagation constant $k_z$ or rather the effective index $n_{\text{eff}}$:

$$F(n_{\text{eff}}^2) = \cos(\alpha d), \tag{2.42}$$

which for TE-polarized light can be written as

$$F_{\text{TE}}(n_{\text{eff}}^2) = \cos\beta r \cdot \cos\gamma w - \frac{\beta^2 + \gamma^2}{2\beta\gamma}\sin\beta r \cdot \sin\gamma w \tag{2.43}$$

with

$$\begin{aligned}
\alpha &= k_{0,x} = k_0 \cdot \sin\theta_0, \\
\beta &= k_{r,x} = k_0\sqrt{n_r^2 - n_{\text{eff}}^2}, \quad n_r^2 = \varepsilon_r (= n_0^2), \\
\gamma &= k_{w,x} = k_0\sqrt{n_w^2 - n_{\text{eff}}^2}, \quad n_w^2 = \varepsilon_w (= n_{\text{H}}^2).
\end{aligned}$$

Here, $r$ and $w$ are the ridge width and groove width, respectively, as shown in Fig. 2.6, $\varepsilon_r$ and $\varepsilon_w$ are their dielectric permittivities. For TM-polarized light, the function $F(n_{\text{eff}}^2)$ can be similarly derived by considering the only component of the magnetic field $H_y$, and Eq. (2.43) becomes

$$F_{\text{TM}}(n_{\text{eff}}^2) = \cos\beta r \cdot \cos\gamma w - \frac{\varepsilon_w^2\beta^2 + \varepsilon_r^2\gamma^2}{2\varepsilon_r\varepsilon_w\beta\gamma}\sin\beta r \cdot \sin\gamma w. \tag{2.44}$$

The functions $F(n_{\text{eff}}^2)$ as expressed in Eqs. (2.43) and (2.44) represent the geometric parameters of the grating region, namely the widths $r$ and $w$ of the grating ridges and grooves and their refractive indices $n_0$ and $n_{\text{H}}$. In contrast, the right hand term of Eq. (2.42) contains the incidence conditions, namely the angle of incidence $\theta_0$ and the period to wavelength ratio. The cosine is 1 in the case of normal incidence and will be assumed as that in the following. The intersections between $F(n_{\text{eff}}^2)$ and $\cos(\alpha d)$ directly lead to discrete values of the effective index $n_{\text{eff}}$ which characterize the discrete grating modes. A solution of Eq. (2.39) is therefore a field composed of upward and downward propagating modes whose z-dependent part $v_m(z)$ is given by

$$v_m(z) = C \cdot \exp(-ik_0 n_{\text{eff}}^m z) + D \cdot \exp(ik_0 n_{\text{eff}}^m z). \tag{2.45}$$

Similar to the characteristics of a simple slab waveguide, all grating modes with $n_{\text{eff}}^2 < 0$ are evanescent and those with $n_{\text{eff}}^2 > 0$ propagate along the z-direction. The effective index of an evanescent mode determines how fast its amplitude decreases with increasing groove depth (z-dependence). In case of a shallow grating, these evanescent modes cannot be neglected, whereas they will play a minor role for deep grooves. The diffraction properties of deep gratings are therefore mainly determined by the propagating modes. Only the intersections between $F(n_{\text{eff}}^2)$ and $\cos(\alpha d)$ and, thus, the parameters $r$, $w$, $n_0$, $n_{\text{H}}$, $\theta_0$, $d$, $\lambda$, and the polarization state determine the amount of propagating modes and their effective indices. The x-dependent amplitude $u_m(x)$ of the $m$th mode can be calculated by inserting the respective effective index into Eq. (2.41) and matching the amplitude at the groove-ridge boundaries. According to the Floquet-Bloch theorem every $u_m(x)$ fulfills the condition of pseudo-periodicity

$$u_m(x+d) = u_m(x)e^{i\alpha d} \tag{2.46}$$

which repeats itself every grating period $d$ in case of normal incidence ($\alpha = 0$). The efficiency of excitation of these modes by the incident wave is, analogous to the waveguide theory, determined by the overlap integral between the field of the incident wave and mode $m$ at the air-grating boundary [76]

$$\langle E_{0,y}(x,0) \leftrightarrow u_m(x)\rangle = \frac{\left|\int E_{0,y}(x,0)\cdot u_m(x)dx\right|^2}{\int \left|E_{0,y}(x,0)\right|^2 dx \cdot \int \left|u_m(x)\right|^2 dx} \tag{2.47}$$

as well as by their Fresnel-like transmission coefficient at this interface which is determined by the change of effective indices (impedance matching). After propagation through the grating region, the modes are partly reflected at the grating-substrate interface and partly transmitted into the substrate. By doing this, every mode distributes its energy to all possible diffraction orders specified by the grating equation (2.18). The coupling efficiency is again defined by the overlap of the fields and the transmission at this interface caused by the change of propagation constants. The contributions of all grating modes interfere and determine the intensity of each diffraction order.

For a deeper understanding of RWGs with large groove depth $g$ or even vanishing waveguide layer $s$, we will now apply the general principles of the modal method to a specific RWG structure. In particular, we will consider a tantala based structure ($n_0 = 1$, $n_\mathrm{H} = 2.1$, $n_\mathrm{L} = 1.45$) working at a wavelength of 1064 nm that had been rigorously simulated and proposed for use in gravitational wave detection [38]. Assuming TM-polarized and normally incident light, the simulations resulted in a set of optimal grating parameters (grating period $d = 700\,\mathrm{nm}$, fill factor $f = 0.5$, groove depth $g = 390\,\mathrm{nm}$, and zero waveguide layer thickness $s = 0\,\mathrm{nm}$) which was the basis of our experimental work presented in paragraph 3.1. According to Ineqs. (2.15) - (2.17) that are derived from the grating equation and determine the period limitation of a RWG for given high-index and low-index material in the ray picture, we have to fulfill $510\,\mathrm{nm} < d < 730\,\mathrm{nm}$. The lower limit defines the smallest period supporting the excitation of higher diffraction orders in the high-index material. For even smaller periods no higher diffraction orders exist.

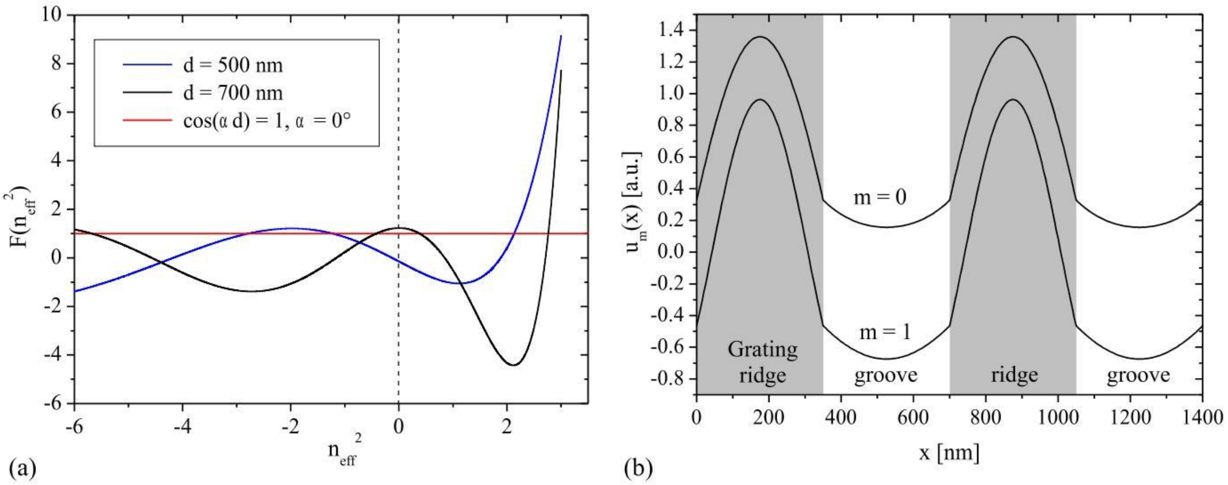

**Fig. 2.7.** (a) $F_{\mathrm{TM}}(n_{\mathrm{eff}}^2)$ for a tantala based RWG with a fill factor of $f = 0.5$ for periods $d = 500\,\mathrm{nm}$ (blue curve) and $d = 700\,\mathrm{nm}$ (black curve). The intersections between $F_{\mathrm{TM}}(n_{\mathrm{eff}}^2)$ and $\cos(\alpha d) = 1$ (red line, for $\alpha = 0$) determine the amount of propagating grating modes and their effective indices. The eigenfunctions $u_0(x)$ and $u_1(x)$ of both grating modes propagating in the 700 nm period grating are shown in (b).

In order to transfer this necessary criterion of potential high RWG reflectivity to the modal method, Fig. 2.7(a) plots the functions $F_{\mathrm{TM}}(n_{\mathrm{eff}}^2)$ for a grating period $d = 500\,\mathrm{nm}$ (blue curve) below the above limitation and a grating period $d = 700\,\mathrm{nm}$ (black curve) as found in Ref. [38] and being well within the limitation. The intersections of these functions with $\cos(\alpha d) = 1$ (red line, for $\alpha = 0$) reveal that for $d = 500\,\mathrm{nm}$ only one propagating mode exists whereas for $d = 700\,\mathrm{nm}$ there are two intersections with $n_{\mathrm{eff}}^2 > 0$. Please note that this is the case not only for a fill factor of $f = 0.5$ (not shown in Fig. 2.7(a)). The x-component of the eigenfunctions of both propagating modes $u_0(x)$ and $u_1(x)$ of the 700 nm period tantala grating with effective indices $n_{\mathrm{eff}}^0 = 1.662$ and $n_{\mathrm{eff}}^1 = 0.619$ are shown in Fig. 2.7(b). They are both symmetric, yet different in their amplitude in the grating ridges and grooves, respectively. While the fundamental mode with $m = 0$ shows a larger field distribution in the grating ridges compared to the first mode with $m = 1$, the first mode does so for the field distribution in the grating grooves. This is evident from the effective index values of both modes. Grating modes with higher effective indices are mainly guided by the high-index ridges while modes with lower indices are bound to the grooves.

As the electric field distribution of an incident plane wave under normal incidence is also symmetric, the overlap integrals for both modes will not vanish. This means that, besides being able to propagate, both modes are indeed excited by the incident wave (overlap integrals were not explicitly calculated). The necessary existence of guided higher diffraction orders in the ray picture now turns into the necessary **excitation and propagation of at least two discrete modes** in the grating region [72, 77]. Moreover, the fundamental grating mode is efficiently coupled to the transmitted zeroth diffraction order because of well matched effective indices ($n_{\mathrm{eff}}^0 \approx n_{\mathrm{L}}$). It is therefore mainly responsible for the energy transfer through the periodic structure. Quite different is the role of the higher order symmetric grating mode. At the interfaces, it is mainly coupled to the evanescent ±1st diffraction orders in the outer media and is therefore reflected back to the grating region. The grating behaves similarly to a Fabry-Perot resonator for this mode. This means that at resonance condition for a certain groove depth $g$ this mode is resonantly excited. In this case the groove depth simultaneously provides a one-way travel phase shift of $\pi$ between the fundamental and the higher order mode [77] which enables for the destructive interference of the fundamental mode outcoupled at the grating-substrate interface. The higher order mode accumulates the energy of the incident wave and returns it to the incidence and transmission media with abrupt amplitude and phase changes which causes high contrast variations of the reflection and the transmission of the RWG.

In summary, if analyzing deep gratings for which the simplified ray picture breaks down, essentially the involved diffraction orders need to be replaced by discrete grating modes. In particular, the zeroth and first diffraction orders correspond to the fundamental and one higher order grating mode, respectively. Their individual behavior and contributions to the high reflection phenomena of RWGs is quite similar which permits a general explanation of different kinds of RWGs independent of their particular grating parameters.

### 2.3.3 Rigorous numerical treatment of RWGs

Even though the theoretical models as presented in the preceding paragraphs provide substantial insight into the working principle of RWGs, they are, however, hardly capable of an analytical grating design process. This means that for a given wavelength and ma-

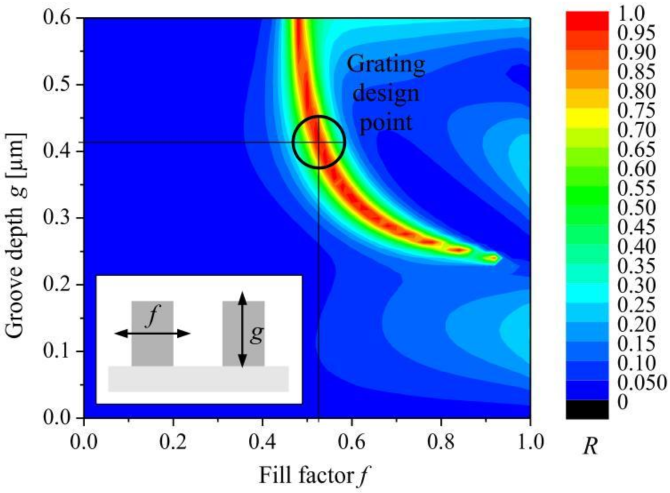

**Fig. 2.8.** Example of a grating parameter design by means of rigorous simulation. Calculated reflectivity of a tantala based RWG ($n_0 = 1$, $n_\mathrm{H} = 2.1$, $n_\mathrm{L} = 1.45$) at a wavelength of 1064 nm for a simultaneous variation of the grating fill factor $f$ and the groove depth $g$, assuming a grating period of $d = 700\,\mathrm{nm}$, a zero waveguide layer thickness $s = 0\,\mathrm{nm}$, and TM-polarized light impinging under normal incidence.

terial choice we cannot easily derive the grating parameters which supply high reflectivity. Very recently, Karagodsky *et al.* showed an analytical model based on the modal method for the description of the very simple configuration of a free-standing high-contrast grating [77]. Fortunately, in order to find appropriate grating parameters independently of any specific layout we can utilize rigorous numerical methods that explicitly solve the Maxwell equations for a particular grating profile, and calculate its reflectivity [78, 79]. However, this implies only a one-way grating design process; that is, we can deduce the reflectivity for certain grating parameters such as the grating period $d$, the fill factor $f$, or the groove depth $g$, vary them, calculate the reflectivity again and so on. After this procedure, the grating parameters resulting in the highest reflectivity as well as the largest fabrication tolerances are being identified as the optimum design structure, and are targeted in the fabrication process. The rigorous methods cannot solve the *inverse diffraction problem* which would directly provide appropriate grating parameters for a specific desired optical function.

Within the past decades, countless different methods have been developed that numerically solve the Maxwell equations in their time dependent (e.g. Finite Difference Time

Domain Method FDTD [80]), integral (e.g. the Generalized Source Method GSM [81]), or differential form (e.g. Fourier Modal Method FMM [78], Rigorous Coupled Wave Analysis RCWA [79]). The latter has turned out to be most suitable for the demand as mentioned above, and it has been numerically implemented in commercially available code such as *UNIGIT* [82] or *GSOLVER* [83]. The idea behind the numerical implementation of the Maxwell equation in the differential form is quite similar to the ideas of the modal method as the incident plane wave is also split into discrete grating modes with individual effective indices. The coupling of these modes to the diffraction orders in the outer media determined by the overlap integrals and the effective index contrasts defines each diffraction efficiency.

Figure 2.8 illustrates the idea of a grating design process where the reflectivity of a tantala based RWG ($n_0 = 1$, $n_\mathrm{H} = 2.1$, $n_\mathrm{L} = 1.45$) at a wavelength of 1064 nm was rigorously simulated using *GSOLVER* for a simultaneous variation of the grating fill factor $f$ and the groove depth $g$ (as sketched at the bottom left hand side). Following the considerations in the above paragraph, we assumed a grating period of $d = 700\,\mathrm{nm}$, a zero waveguide layer thickness $s = 0\,\mathrm{nm}$, and TM-polarized light impinging under normal incidence. The most beneficial grating design point in that case can be found at $f \approx 0.5$ and $g \approx 400\,\mathrm{nm}$, respectively, in agreement with the results in [38]. All grating design considerations presented in this work had been performed in the same manner. However, in most cases the design processes are more complicated due to more than just two degrees of freedom which requires fundamental theoretical background beforehand.

# 3 RWGs for mirror applications

As can be found in literature, the phenomenon of guided-mode resonant reflection from a corrugated waveguide had first been observed in the mid 1980s by Golubenko *et al.* [34]. The first particular application as narrowband filters was proposed and realized by Magnusson and Wang in 1992 [35]. In the following years various groups in the world adopted these devices for their optics research and presented theoretical as well as experimental results covering different grating configurations and material-wavelength combinations [36, 37, 61, 69, 84, 85]. However, due to the complexity of the fabrication process, most of the work was restricted to theoretical and grating design considerations. In the case of experimental realization, the results significantly deviated from the simulated data predicting perfect reflectivity for the resonance wavelength. In light of the rapid progress in microstructure technology during the recent years driven by the semiconductor industry, Bunkowksi *et al.* proposed to employ RWGs as a low thermal noise alternative to conventionally coated cavity mirrors in the field of gravitational wave detection [38]. For this application, reflectivities of the mirrors close to 100 % are required and thus state-of-the-art fabrication technologies are necessary. In the first part of this chapter we show the first experimental realization and characterization of a resonant waveguide grating based high-reflection cavity mirror which is based on tantala as the high-index material and 1064 nm laser light [39]. Moreover, motivated by current findings in the field of thermal noise research (see paragraph 3.2 for more detail), we fabricated different RWGs that are built on silicon and 1550 nm laser light, and achieved high reflectivities in a broad spectral range.

## 3.1 Tantala based RWGs for 1064 nm laser light

Today's and next generation gravitational wave detectors use fused silica as the test mass material ($n_{\mathrm{L}} \approx 1.5$) [6] and Nd:YAG lasers as ultrastable light sources [20] with a central wavelength of $\lambda = 1064\,\mathrm{nm}$. The most common high-index material for this wavelength region is $Ta_2O_5$ (Tantala) with a refractive index of $n_{\mathrm{H}} \approx 2.1$ [21]. In the following we will restrict ourselves to this material combination for the realization of a high-reflectivity RWG working at 1064 nm laser light. The mirror substrate in our case was soda lime glass and carried a single layer grating of tantala with a thickness of 400 nm, and was used as a cavity coupler of a high-finesse standing wave cavity. From the cavity finesse we were able to deduce a reflectivity of $(99.08 \pm 0.05)\,\%$ at the laser wavelength of 1064 nm. This is, to the best of our knowledge, the highest value of resonant reflection that has ever been reported at this wavelength. Moreover, a standing-wave cavity setup has never been utilized to accurately determine a grating based resonant reflectivity before [39].

### 3.1.1 Grating design considerations

According to Ineqs. (2.15) - (2.17) and assuming the above mentioned refractive indices of silica and tantala, the grating period is restricted by $512\,\mathrm{nm} < d < 710\,\mathrm{nm}$. For systematic design considerations in terms of broad resonance behavior, we refer to the work of Bunkowski *et al.* [38] wherein a Rigorous-Coupled-Wave Analysis (RCWA) [79] was used to find appropriate grating parameters with high reflectivity as well as convenient fabrication tolerances. These simulations included three free parameters besides the grating period $d$, namely the groove depth $g$, the waveguide thickness $s$ and the grating fill factor $f$. As a result, assuming TM-polarized light (electric field oscillating perpendicular to the grating ridges) and a rectangular grating profile, for the purpose of a broadband reflection peak, large values for the grating period close to 700 nm are favorable. In this case, the diffraction coefficient $\eta$, as introduced in paragraph 2.3.1 and determining the diffraction efficiency into the first orders, shows its maximum which broadens the resonance peak. Moreover, the simulations showed that high TM-reflectivity can even be found for zero waveguide layer thickness ($s = 0\,\mathrm{nm}$), if the groove depth and the grating fill factor are about $g \approx 400\,\mathrm{nm}$ and $f \approx 0.5$, respectively. As the overall thickness of the high-index coating material is the crucial factor for coating thermal noise, see chapter 2.2, the reduction of the residual waveguide layer down to zero would be highly beneficial [24]. The effective tantala layer thickness in this case ($g = 400\,\mathrm{nm}$, $f = 0.5$) is only about $0.2\,\mu\mathrm{m}$. In contrast a conventional mirror typically comprises an 18 double-layer dielectric stack with an overall tantala thickness of about $3\,\mu\mathrm{m}$. This suggests a significant thermal noise reduction.

Please note that, as described in section 2.3, for a grating with vanishing waveguide layer thickness (see Fig. 2.3(b)), the simplified ray picture breaks down. The diffraction orders that are involved in the coupling process rather need to be considered as corresponding to discrete grating modes propagating through the binary grating region according to the modal method [71]. However, the simulations are based on a RCWA which is still valid for $s = 0\,\mathrm{nm}$.

### 3.1.2 Fabrication process

For the fabrication of the desired waveguide grating, a soda lime glass substrate with an index of refraction of $n_\mathrm{L} = 1.515$ was first coated with a 400 nm tantala layer with an index of refraction of $n_\mathrm{H} = 2.105$ by means of Plasma-Ion-Assisted Deposition (PIAD). With regard to the desired groove depth, soda lime glass was chosen as the substrate material instead of fused silica since it remains nearly unaffected while the tantala etching process. The grating with a period of $d = 690\,\mathrm{nm}$ was defined by the use of electron beam lithography for an area of $(75\,\mathrm{mm})^2$, aiming at a grating fill factor of $f = 0.515$. The final Inductively-Coupled-Plasma (ICP) etching step was adjusted to match the desired grating groove depth of $g = 400\,\mathrm{nm}$ which corresponds to a zero waveguide layer thickness ($s = 0\,\mathrm{nm}$). Figure 3.1 depicts a top view scanning electron microscope (SEM) image of the grating used in the experiment (left hand side) and a cross-sectional view of the resulting grating profile of a grating from the same fabrication process but different fill factor (right hand side), revealing that the actual groove depth was just slightly deviating from the target value.

However, the tantala grating ridges were found to exhibit a trapezoidal shape instead of a rectangular one which had been assumed for the design considerations in Ref. [38]. Most

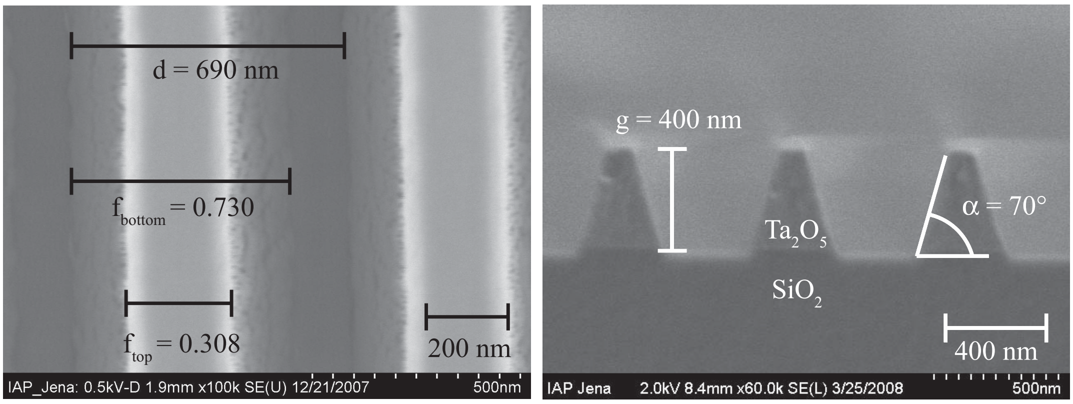

**Fig. 3.1.** Left hand side: Top view of the fabricated resonant waveguide grating with trapezoidal grating profile. The accurate values for the fill factors arose from the spectral fit in Fig. 3.2. Right hand side: Cross-sectional view of a related grating with the same groove depth but different fill factor.

likely the ICP etching process was affected by a crystal formation within the tantala layer during its deposition. Subsequent rigorous simulation using a staircase approximation [86] showed that such a trapezoidal profile is still capable of high reflectivity while the bandwidth remains substantially uneffected.

From the left hand side of Fig. 3.1, we realized an effective fill factor of 0.52 instead of 0.515 which would give a maximum in reflectivity. This leads to a stronger dependence of the reflectivity to variations of the grating parameters over the grating area that occur in the fabrication process.

### 3.1.3 Experimental characterization

The spectral transmittance under near normal incidence $(0 \pm 1)^\circ$ was measured using a fiber based white-light source and a spectrum analyzer with a resolution of 50 pm. The measured data is shown in Fig. 3.2 (black curve) and reveals a minimum transmittance of 0.19 % at a wavelength of $\lambda = 1065.6$ nm and a transmittance of 0.8 % at the central wavelength $\lambda = 1064$ nm. The kink near $\lambda = 1045$ nm is related to the incipient transmission of the first diffracted orders into the substrate material since the condition for total internal reflection is no longer fulfilled at this wavelength, see Ineq. (2.17). The spectral bandwidth of the resonant device shows a rather broad transmission of $\leq 10\,\%$

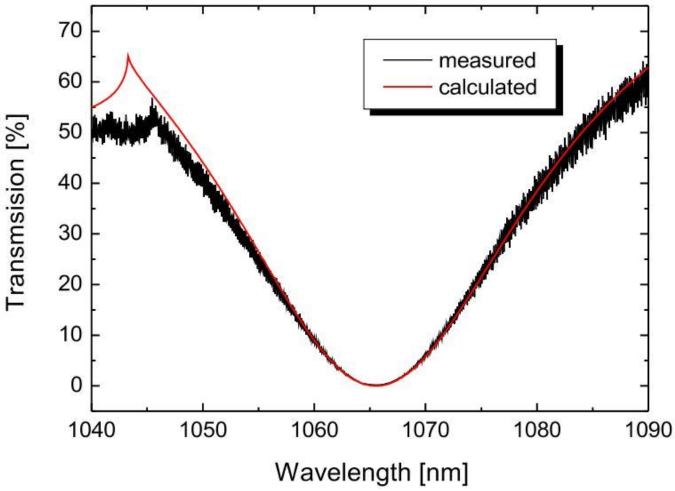

**Fig. 3.2.** Spectral zeroth order transmittance of the resonant grating based cavity coupler under normal incidence and for TM-polarization.

over a wavelength range of 12 nm. Assuming a grating period of $d = 690\,\text{nm}$, a groove depth of $g = 400\,\text{nm}$ ($s = 0\,\text{nm}$) and a side wall angle of $\alpha = 70^\circ$ which can be estimated with the cross-sectional SEM image on the right hand side of Fig. 3.1, the best fitted spectral response was achieved with a top grating fill factor of $f_{\text{top}} = 0.308$, see red curve in Fig. 3.2.

Setting up a linear Fabry-Perot resonator with the waveguide grating as a coupling mirror enabled us to exactly adjust the angle of incidence to be zero degree and was used to determine the reflectivity at a wavelength of 1064 nm. The measurement was carried out at the Institute of Gravitational Physics, University of Hanover, Germany, in close collaboration, and in the following its methods and results are only briefly presented. A simplified sketch of the experimental setup is depicted in Fig. 3.3. The light source was a Nd:YAG laser with a wavelength of 1064 nm. The light was spatially filtered by a ring modecleaner (MC) which was stabilized via the Pound-Drever-Hall (PDH) control scheme [87]. Therefore, a phase modulation was used that was imprinted on the light by means of an electro-optical modulator (EOM). The linear Fabry-Perot resonator was set up with the waveguide grating and a superpolished, high reflectivity end mirror. The length of the cavity $L$ defines its free-spectral range $\text{FSR} = c/2L$. The cavity linewidth (full width at half maximum) $\Delta\nu$ was measured in order to determine the finesse $F = \text{FSR}/\Delta\nu$ and subsequently the reflectivity of the grating device.

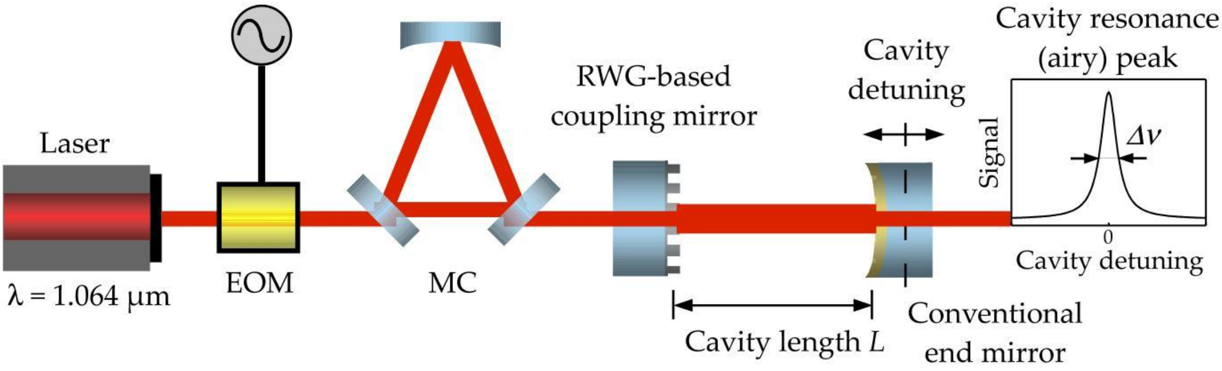

**Fig. 3.3.** Simplified sketch of the experimental setup for the characterization of the tantala based resonant waveguide grating (RWG) as a cavity coupling mirror. Electro-optical modulator (EOM), modecleaner (MC). For more details see [39].

In order to explicitly obtain the cavity linewidth from the signal detected in transmission of the cavity, its detuning around an airy peak was calibrated by using the PDH phase modulation signals as frequency markers. For more details concerning the cavity measurement and the measured data, the reader is referred to [39]. The linewidth was averaged over twenty measurements which resulted in $\Delta\nu = (461 \pm 19)\,\mathrm{kHz}$. Hence, the finesse was $F = 657 \pm 27$. Since the product of the amplitude reflectivities $\rho_1$ and $\rho_2$ of the end mirror and waveguide grating, respectively, is connected to the finesse by

$$\rho_1\rho_2 = 2 - \cos\left(\frac{\pi}{F}\right) - \sqrt{\left(\cos\left(\frac{\pi}{F}\right) - 2\right)^2 - 1}, \tag{3.1}$$

the waveguide grating power reflectivity was found to be $\rho_2^2 = (99.08 \pm 0.05)\,\%$. Here, any resonant reflection phase shift [88] can be neglected since the light source is a single frequency laser. Though the achieved value was a record for measured resonant reflection of 1064 nm laser light at this time, it still does not compete with conventional multilayer mirrors when only regarding optical loss [19]. Please note that the spectral measurement as well as the cavity setup were optimized to lowest transmission by adjusting the beam position on the grating. The reflectivity over the entire grating area was found to be higher than 96 % with a spatial resolution given by the beam radius of $\approx 130\,\mu$m. These variations can be explained by a deviation of the effective fill factor in the range between 0.52 and 0.525. Assuming a fill factor of 0.515, the same deviation would lead to a reflectivity higher than 99.6 % over the whole area.

### 3.1.4 Summary and discussion

For the purpose of pushing highly reflective optical components towards a low thermal noise regime, we demonstrated a coupler for a standing-wave cavity based on a guided-mode resonant grating device for the first time. By periodically structuring a 400 nm tantala layer on top of a soda lime glass substrate we achieved a record reflectivity of 99.08 % for a wavelength of 1064 nm and TM-polarized light. By utilizing strong resonant light coupling a broad spectral bandwidth with a transmission of $\leq 10\,\%$ over a wavelength range of 12 nm could be obtained. Simultaneously, low coating thermal noise can be expected due to a vastly decreased effective tantala layer of only about 0.2 $\mu$m compared to conventional mirrors with an overall tantala thickness of about 3 $\mu$m. A further reflectivity increase towards the theoretical limit of 100 % is possible by means of more tolerant grating parameter design and detailed technology evaluation for a better design-experiment match of the fill factor.

## 3.2 Silicon based RWGs for 1550 nm laser light

In spite of the well established substrate-wavelength combination of fused silica and 1064 nm laser light for high-precision measurements, within the past few years silicon rather than fused silica was found to be a more promising candidate for the future substrate material of choice [40, 41]. This is due to its lower absorption of probably less than $10^{-8}\,\mathrm{cm}^{-1}$ at a 1550 nm wavelength [42] and much higher Q-factors of $10^{9}$ at cryogenic temperatures [43]. Such material parameters are connected to a remarkably reduced substrate thermal noise level [18], and even increase the relative impact of the coating to the total thermal noise budget and, thus, the need for a significant coating thickness reduction. For this reason, the second part of this chapter presents the rigorous modeling and the experimental realization of highly reflective silicon based grating reflectors working at the telecommunication wavelength of 1550 nm. The mirror substrates were standard silicon wafers that carried a (low refractive index) silica layer and a (high refractive index) silicon layer on top which have been periodically structured. For a first sample, the peak reflectivity was located closely to the wavelength of 1.55 $\mu$m with a value of about 98.9 %,

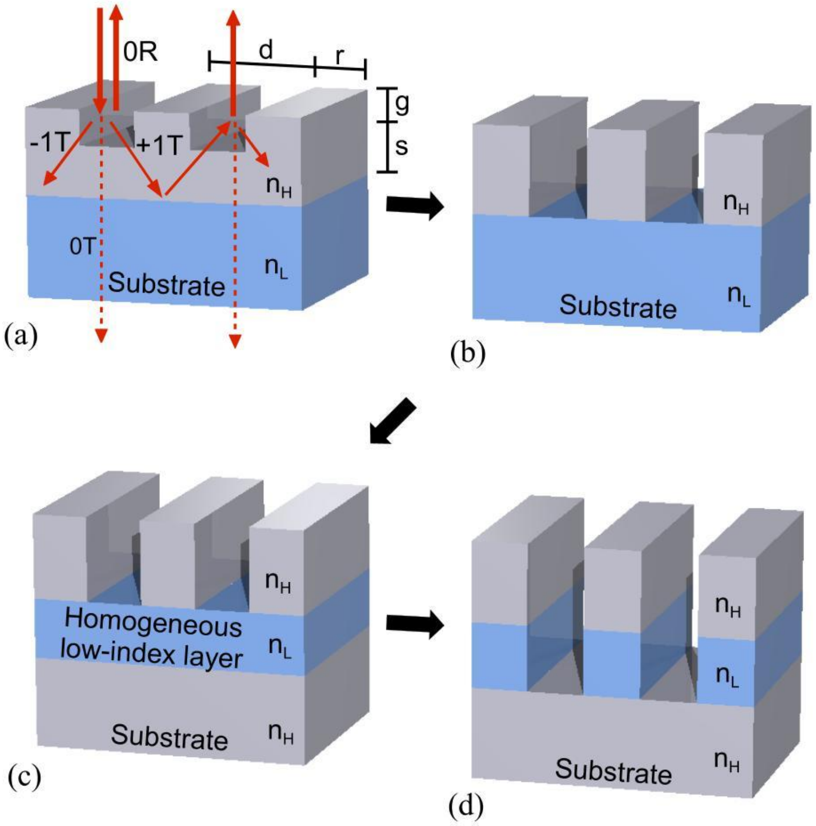

**Fig. 3.4.** Evolution of guided-mode resonant structures. (a) Initial RWG configuration with a high-index layer corrugated at its surface on top of a low-index substrate described in a ray picture (see paragraph 2.3). (b) Stand-alone high-index grating ridges corresponding to a zero waveguide layer thickness ($s = 0$ nm) as assumed for tantala based RWGs (see paragraph 3.1). (c) Reduction of the low-index substrate to a thin layer necessary for silicon based RWGs. (d) Even reduced total effective coating thickness via structuring of the low-index layer down to the substrate.

while for a second one we achieved a value of higher than 96 % for a broad spectral range of at least 110 nm.

### 3.2.1 Grating design considerations

When using silicon ($n = 3.48$) as the substrate material, one cannot find a dielectric material with a higher refractive index serving as the waveguide layer for resonant grating structures as shown in Figs. 3.4(a) and (b). Thus, silicon is also supposed to act as the waveguide material ($n_{\mathrm{H}} = 3.48$), making the introduction of a low refractive index layer

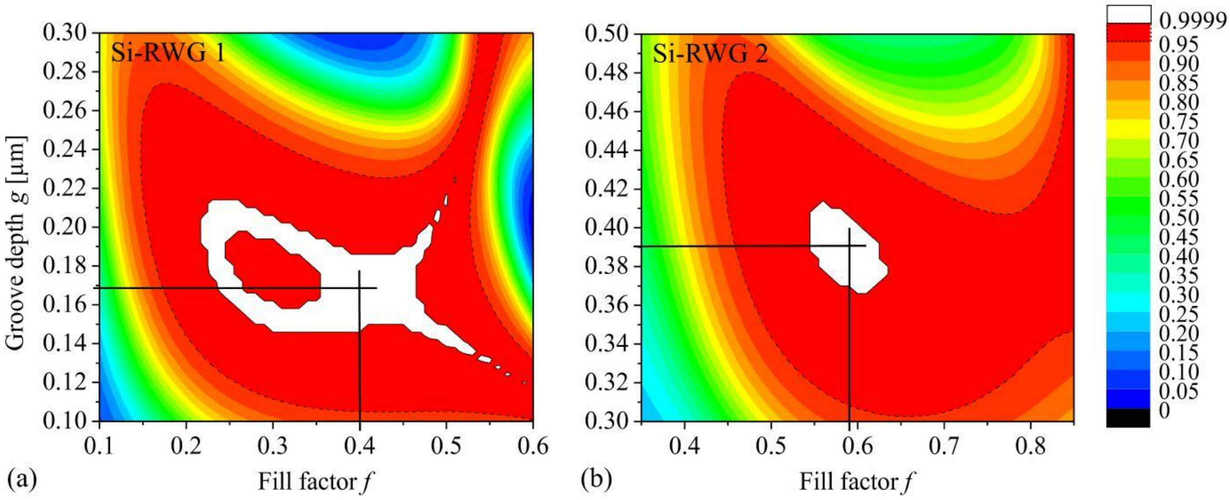

**Fig. 3.5.** Simulated reflectivity for normal incidence over grating fill factor $f$ and silicon grating groove depth $g$ for (a) the Si-RWG 1 shown in element (c) of Fig. 3.4 with a period of $d = 950\,\text{nm}$ and (b) the Si-RWG 2 shown in element (d) of Fig. 3.4 with a period of $d = 653\,\text{nm}$. For (a) TE-polarized and for (b) TM-polarized light was assumed. In (b) the fill factor $f$ applies to both, the top silicon as well as the silica grating beneath. The wavelength is $\lambda = 1.55\,\mu\text{m}$.

beneath the waveguide grating indispensable, see Fig. 3.4(c). This cladding layer must prevent evanescent transmission of higher diffraction orders or rather higher order grating modes to the substrate by exceeding a certain minimum thickness. Here, we chose $SiO_2$ ($n_L = 1.444$) since it is the most frequently used dielectric optical material. In terms of minimizing the necessary total effective coating thickness, we again assumed a zero waveguide layer thickness ($s = 0\,\text{nm}$) as shown in Fig. 3.4(c). In Refs. [37] and [84] it was theoretically as well as experimentally demonstrated that this grating configuration is still capable of efficient resonant reflection.

For an even reduced total effective coating thickness, we propose to also structure the silica layer down to the substrate, see Fig. 3.4(d). Moreover, this suggests an increased refractive index contrast between low-index layer and high-index grating since the structured silica layer will lead to an effective refractive index being smaller than that for a homogeneous layer [89]. This promises a broader spectral performance as determined by Eqs. (2.30) and (2.32). The stepwise transition from the initial waveguide grating layout in Fig. 3.4(a) to the ones assumed for our design considerations ((c) and (d)) is depicted in Fig. 3.4.

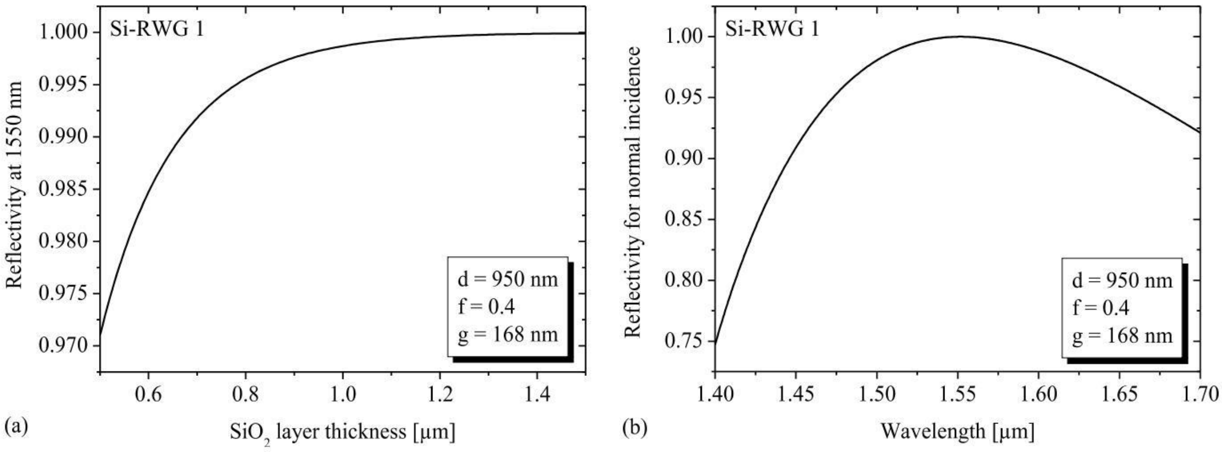

**Fig. 3.6.** Simulated reflectivity for the found design point of Si-RWG 1 over (a) low-index $SiO_2$ layer thickness for $\lambda = 1.55\,\mu$m and normal incidence and over (b) wavelength for normal incidence.

For systematic design considerations in terms of broad resonance behavior, we used a Rigorous-Coupled-Wave Analysis (RCWA) [79] to find appropriate grating parameters with high reflectivity as well as convenient fabrication tolerances. According to Ineqs. (2.16) and (2.17), we find $445\,\text{nm} < d < 1070\,\text{nm}$ for a wavelength of $\lambda = 1550\,\text{nm}$ normally incident onto the grating device.

For the RWG layout in Fig. 3.4(c) (called *Si-RWG 1* in the following), we chose a grating period of $d = 950\,\text{nm}$. Assuming TE-polarized light (electric field oscillating parallel to the grating ridges), Fig. 3.5(a) shows the reflectivity for a simultaneous variation of both, the grating groove depth $g$ and the grating fill factor $f$ ranging from $0.1\,\mu\text{m} < g < 0.3\,\mu\text{m}$ and $0.1 < f < 0.6$, respectively. The silica layer had a start thickness of $2\,\mu$m. The plotted reflectivity reveals a wide range of high reflectivity including regions with a nearly perfect value (99.99 % up to 100 %) indicated by the solid line. A highly beneficial design point is $(g,\ f) = (168\,\text{nm},\ 0.4)$ where high reflectivity as well as convenient fabrication tolerances are found. To examine the necessary minimum thickness of the $SiO_2$ layer beneath the grating, it was varied in the range from $0.5\,\mu$m to $1.5\,\mu$m. Figure 3.6(a) shows the reflectivity for this variation where a $SiO_2$ layer thickness of $1\,\mu$m ensures a reflectivity of higher than 99.96 %. The spectral response of the found design point is illustrated in Fig. 3.6(b), displaying a 95 % reflectivity for a broad wavelength range from $1.47\,\mu\text{m} < \lambda < 1.66\,\mu\text{m}$.

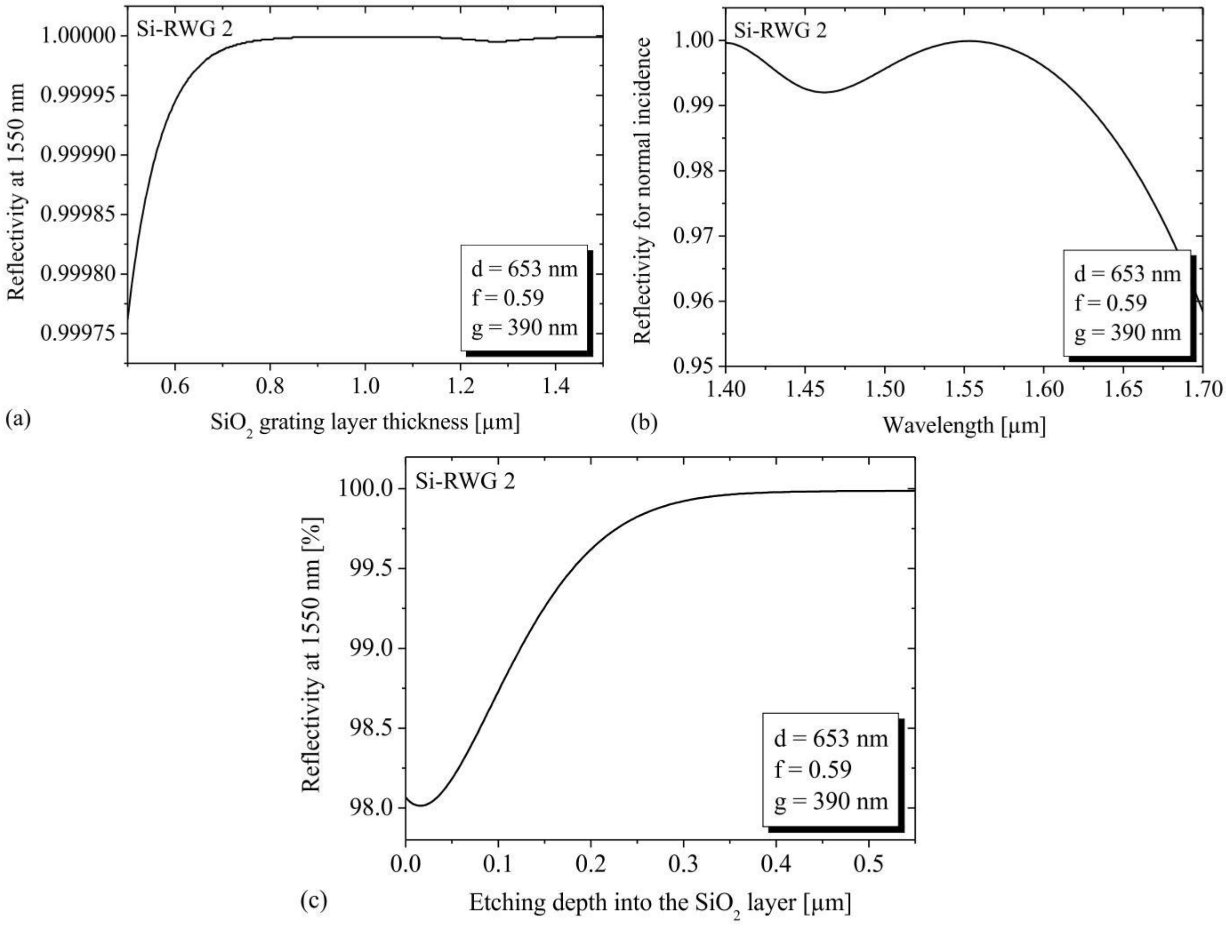

**Fig. 3.7.** Simulated reflectivity for the found design point of Si-RWG 2 over (a) the low-index $SiO_2$ grating layer thickness for $\lambda = 1.55\,\mu$m and normal incidence, over (b) the wavelength for normal incidence, and over (c) the etching depth into the 550 nm thick $SiO_2$ layer for $\lambda = 1.55\,\mu$m and normal incidence.

For the advanced RWG layout in Fig. 3.4(d) (called *Si-RWG 2* in the following), we chose a grating period of $d = 653$ nm and TM-polarized light. Similar to the procedure for the Si-RWG 1, we first calculated the reflectivity for a simultaneous variation of the grating fill factor $f$ from 0.35 to 0.85 and the groove depth of the top silicon grating $g$ from 0.3 to 0.5 $\mu$m. In that case, the same fill factor $f$ applies to both, the top silicon as well as the silica grating beneath. Again, the silica grating layer had a start thickness of 2 $\mu$m. The results are plotted in Fig. 3.5(b) and reveal a highly beneficial design point at ($g$, $f$) = (390 nm, 0.59) with a perfect reflection value (99.99 % up to 100 %) as well as large fabrication tolerances quite similar to those for the Si-RWG 1 in Fig. 3.5(a). In order to identify the minimum silica grating layer thickness providing a certain desired high reflectivity, Fig. 3.7(a) plots the reflectivity of the found design point over a variation of this thickness from 0.5 to 1.5 $\mu$m. Here, a thickness of only 550 nm permits values greater than 99.98 % whereas for the TE-case a thickness of at least 1 $\mu$m is required, see Fig. 3.6(a). This is due to a faster evanescent decay of TM grating modes compared to TE modes as described in literature [71, 73]. The spectral behavior shown in Fig. 3.7(b) is even superior to that of the Si-RWG 1 with reflectivities exceeding 96 % for a rather broad wavelength range from $1.4\,\mu\text{m} < \lambda < 1.7\,\mu\text{m}$.

With regard to the fabrication process of the Si-RWG 2, Fig. 3.7(c) displays the reflectivity for an ongoing etch into the silica layer from zero to 550 nm. It turns out that an etching depth of a few tens of nanometers below the target value is not critical which should be feasible with state-of-the-art etching technologies.

As the overall thickness of the coated layers is the crucial factor for coating thermal noise, our grating devices with effective thicknesses of about 1.1 $\mu$m for the Si-RWG 1 ($[f \times \text{Si grating depth } g] + \text{SiO}_2$ layer) and of only 0.55 $\mu$m for the Si-RWG 2 ($f \times [\text{Si grating } g + \text{SiO}_2 \text{ grating}]$) are expected to significantly reduce the thermal noise level compared to conventional mirrors. The latter typically comprise an 18 double-layer stack with an overall thickness of about 7 $\mu$m [24].

### 3.2.2 Fabrication process

For the fabrication of both silicon RWG layouts, standard silicon wafers with 100 mm in diameter were first coated with a 1 $\mu$m and a 0.55 $\mu$m silica layer, respectively, and subsequently with a 168 nm and a 390 nm silicon layer, respectively, by means of Plasma-Ion-Assisted Deposition (PIAD). The wafer intended to carry the Si-RWG 2 was additionally coated with a 60 nm chromium layer serving as the mask during the silicon and the silica etching processes. Please note that for a total etching depth of only 170 nm for the Si-RWG 1 we can use the resist etching mask, making the involvement of chromium processing for this sample unnecessary. After spin-coating an electron beam sensitive (chemically amplified) resist on top, the gratings with the periods of $d = 950$ nm and $d = 653$ nm were defined by the use of electron beam lithography for the same areas of (7.5 x 12) mm$^2$ aiming at a grating fill factor of $f = 0.4$ for the Si-RWG 1 and of $f = 0.59$ for the

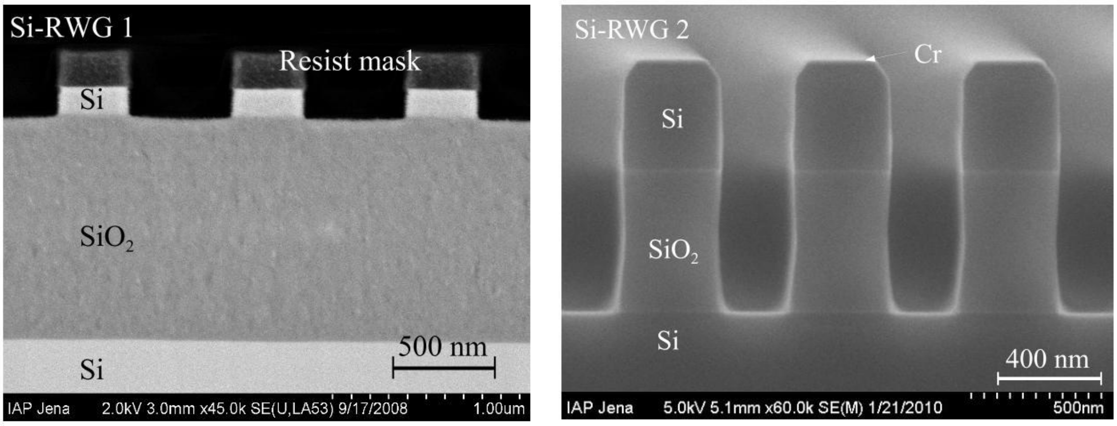

(a) (b)

**Fig. 3.8.** Cross-sectional view SEM images of the fabricated grating profiles with (a) $d = 950\,\mathrm{nm}$, $g = 170\,\mathrm{nm}$, $f = 0.4$, and $SiO_2$ layer thickness of $1\,\mu\mathrm{m}$ and (b) $d = 653\,\mathrm{nm}$, $g = 390\,\mathrm{nm}$, $f = 0.6$, and $SiO_2$ grating layer thickness of $0.55\,\mu\mathrm{m}$. The resist mask in (a) and chromium mask in (b) were removed prior to characterization.

Si-RWG 2. An Inductively-Coupled-Plasma (ICP) silicon etching process was adjusted to match the desired grating groove depths of $g = 168\,\mathrm{nm}$ and $g = 390\,\mathrm{nm}$, respectively, which correspond to a zero waveguide layer thickness ($s = 0\,\mathrm{nm}$). While being finished with the fabrication of the Si-RWG 1, for the realization of the Si-RWG 2, a final silica etching process was conducted to completely structure the coated double layer down to the substrate. For this purpose, a Reactive Ion Beam Etching (RIBE) process was utilized which allows to meet the desired grating profile because of a very high selectivity between silica and silicon etch.

Figure 3.8 depicts cross-sectional view scanning electron microscope (SEM) images of both fabricated and characterized grating profiles. Even though slight deviations can be obtained from the images, all grating parameters for the Si-RWG 1 and 2 ($d, g, f$, and $SiO_2$ layer thickness) are in good agreement with the design values from the preceding paragraph. In particular, the etching processes could be successfully stopped at the layer interfaces. The parameter deviations will be taken into account in more detail within the following experimental section in order to judge the measurement results. The residual resist etching mask in (a) and chromium etching mask in (b) on top of the silicon grating ridges were removed prior to characterization.

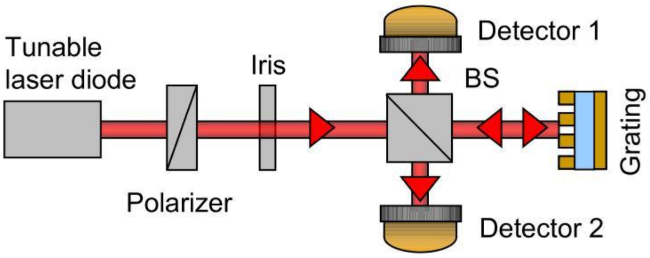

**Fig. 3.9.** Experimental setup for the measurement of the spectral reflectivity of RWGs under normal incidence $(0 \pm 1)^\circ$ with an error of ± 0.5 %. As a reference for the measured intensity a multilayer dielectric mirror rated at $R = 1$ for the available spectral range was used.

### 3.2.3 Experimental characterization

For both samples the spectral reflectivity under normal incidence $(0 \pm 1)^\circ$ was measured using a fiber coupled tunable diode laser. The available spectral range was $1.518\,\mu\text{m} < \lambda < 1.59\,\mu\text{m}$ for the Si-RWG 1 whereas it was $1.52\,\mu\text{m} < \lambda < 1.63\,\mu\text{m}$ for the Si-RWG 2. After the polarized and collimated beam was reflected by the grating, it was deflected onto a photo detector by a beam splitter. As a reference for the measured intensity we used a multilayer dielectric mirror rated at $R = 1$ for the available spectral ranges. The experimental setup is sketched in Fig. 3.9.

The measured data for the Si-RWG 1 is shown in Fig. 3.10(a) and reveals a broadband high reflectivity of greater than 98 % for the entire available spectral range from $1.52\,\mu$m to $1.59\,\mu$m. The peak reflectance is located closely to the wavelength of $1.55\,\mu$m with a value of about 98.9 % where an error of ± 0.5 % needs to be taken into account due to the measurement setup. The measured angular reflectivity is plotted in Fig. 3.10(b) together with a rigorously simulated curve in red which was obtained by iteratively approximating the real grating profile from Fig. 3.8(a) by a rectangular fragmentation. The parameters finally resulting in the red curve and best fitting the measured data were $g = 151$ nm, $f = 0.43$, and a silica layer thickness of $1.187\,\mu$m which are in very good agreement with the deviations obtained from the SEM image. The spectral reflectivity for the same parameters is also included as the red curve in the plot of Fig. 3.10(a). Even though the run of the measured data and simulated curve are similar, a discrepancy of about

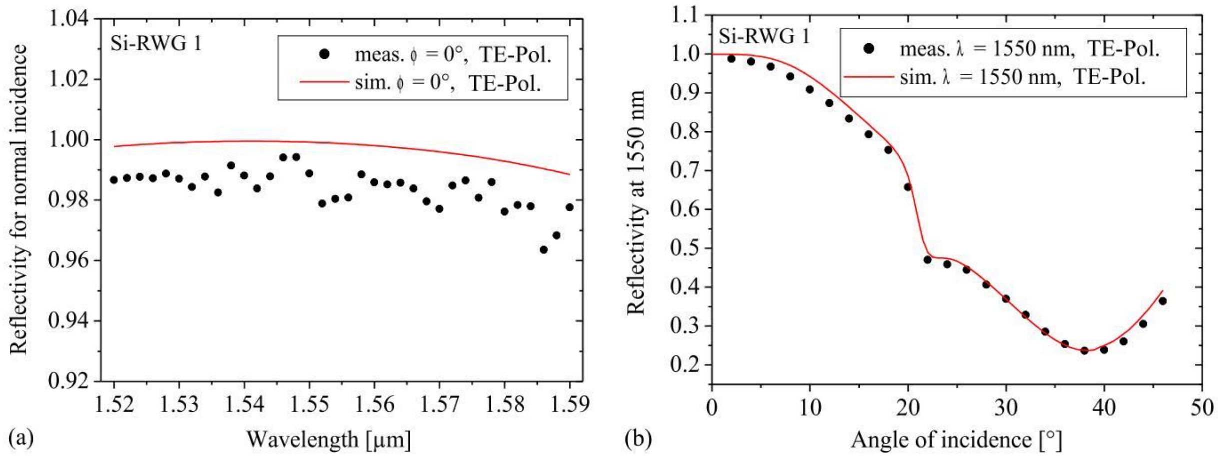

**Fig. 3.10.** Measured (a) spectral reflectivity for normal incidence $(0 \pm 1)^\circ$ and (b) angular reflectivity for a wavelength of 1.55 $\mu$m of the grating in Fig. 3.8(a). The red curves represent rigorously simulated data for grating parameters approximating the real shape.

1 % between them can be found for the entire spectral range. This discrepancy is, most likely, mainly attributed to scattering or absorption losses from any leftovers from the fabrication process. This could, however, not be verified since the rear side of the wafer was unpolished.

Figure 3.11 displays the measured spectral reflectivity and transmittivity for the Si-RWG 2 whose fabricated grating profile is shown in Fig. 3.8(b). The data reveal a nearly constant plateau of high reflectivity around 96 % for a broad spectral range of at least 110 nm. This range is expected to be even broader when extrapolating the run of a virtual curve fitting the experimental data to larger wavelengths. However, in comparison to the Si-RWG 1, the discrepancy between measured and simulated reflectivity (see Fig. 3.7(b)) is increased to a value of about 4 %. Unfortunately, the measured transmittivity of the grating does not provide any helpful information about the missing laser light intensity. Quite the contrary: the data is far below the expected transmission level of about 4 % and, moreover, does not correlate with the reflectivity curve. This indicates again absorption losses since during the measurements scattered light strong enough to account for the missing light was not observed. Such high absorption losses are most likely due to residue of the chromium etching mask whose removal (done by a Reactive-Ion etching process) was either incomplete or caused any re-deposition of chromium. Within the time frame

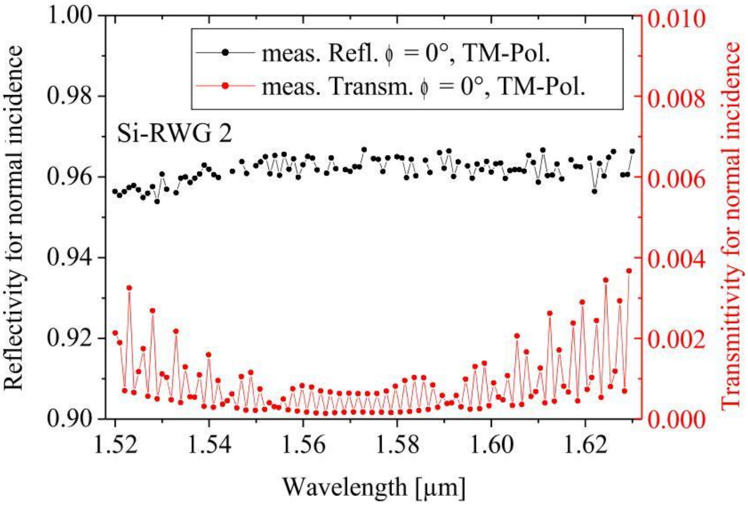

**Fig. 3.11.** Measured spectral reflectivity and transmittivity for normal incidence $(0 \pm 1)^\circ$ of the grating in Fig. 3.8(b).

of this work, an exact explanation could unfortunately not be found.

### 3.2.4 Summary and discussion

Current findings in the field of thermal noise research suggest to employ silicon and 1550 nm laser light as the material-wavelength combination for future high-precision measurements instead of fused silica and a wavelength of 1064 nm. Against this background, silicon supported RWG layouts are required to further reduce thermal noise issues. The rigorous modeling presented in this paragraph showed that if using only a thin corrugated double layer of silica and silicon on top of a silicon substrate, broadband perfect reflection can be achieved with large grating parameter tolerances. To the best of our knowledge, complete structuring of the low-index silica layer down to the substrate of an RWG was first proposed by this work. This approach provides a minimum effective coating thickness which has a value of only 550 nm for a found design structure compared to a conventional mirror with a typical coating thickness of about 7 $\mu$m. Two demonstrators have been successfully manufactured with a nearly perfect match of designed and fabricated grating profile. In good agreement with the simulated data from a grating approximating the real shape, a maximum reflectivity of 98.9 % for the design wavelength was obtained together with a broadband spectral behavior. However, the discrepancy between the measured values and unity is not negligible and is most likely attributed to absorption losses as indicated by transmission measurements. For a better understanding, a deeper investigation is necessary and should involve further characterization instruments supplying information about the grating surface chemistry.

# 4 New approach for monolithic RWGs I - T-shaped grating

Although the approaches as presented in the preceding chapter reduce the thick dielectric multilayer stack of conventional mirrors to a thin waveguide layer, at least one additional material has to be added still resulting in an increased mechanical loss. They cannot provide a complete Brownian coating thermal noise suppression as desired by the community of high-precision metrology. For this purpose, a purely monolithic RWG layout would be of enormous interest. A very intuitive but not practical monolithic implementation of the RWG shown in Fig. 3.4(c) can be obtained by replacing the low-index layer with air ($n_\mathrm{L} = 1$) resulting in grating ridges levitated above the substrate [90–92]. However, this approach appears hardly capable for applications in the field of high-precision measurements due to its fragility and stringent production requirements. Most severely, it is limited to very small grating areas with dimensions in the range of a few hundred microns. In this chapter we propose and realize a highly reflective monolithic dielectric surface mirror which overcomes these limitations. By etching T-shaped grating ridges into the surface of a crystalline material, perfect reflectivity of the surface can be achieved without adding any other material [44, 45]. The first paragraph of this chapter presents the basic idea of this new approach based on the considerations in section 2.3.2 according to the modal method. The second paragraph will report on the first experimental realization of a high-reflectivity cavity mirror that solely consists of a single silicon crystal. In full agreement with rigorous modeling we realized a record reflectivity of $(99.79\pm0.01)\,\%$ at a wavelength of $1.55\,\mu$m, and achieved a cavity finesse of 2784 [46]. Finally, design considerations for such structures in lithium niobate are presented that might offer an efficient combination of resonant light excitation and nonlinear optical effects.

## 4.1 Basic idea

In order to enable the reader to follow our new approach of a purely monolithic RWG configuration, Fig. 4.1 illustrates the stepwise evolution from previous layouts such as the initial one in Fig. 4.1(a) investigated by Golubenko *et al.* in the mid 1980s to finally the new T-shaped structure in Fig. 4.1(d) being the main subject of this work. This evolution does not reflect any chronological order, but rather it provides stepwise modifications that help to understand the basic analogy of different RWG layouts. The initial mirror architecture in Fig. 4.1(a) uses a homogeneous high-index layer corrugated at its surface on top of a low-index substrate and can be easily understood by the ray picture, see paragraph 2.3.1. Aiming at a minimum effective coating thickness, perfect reflectivity can also be achieved without the homogeneous part of the waveguide layer as proposed and realized in paragraph 3.1, see Fig. 4.1(b). In the case of using silicon as the substrate material, the low-index substrate which is necessary for total internal reflection must be reduced to a layer as presented in paragraph 3.2, see Fig. 4.1(c). This layer has to have a certain minimum thickness, for which evanescent transmission of the higher orders is still low. For the elements in Figs. 4.1(b) and (c), the ray picture breaks down, but they can be understood by the modal method as described in paragraph 2.3.2.

Eventually, as shown in Fig. 4.1(d), we propose to replace the remaining homogeneous low-index layer by an *effective* low-index layer to supply a monolithic configuration. This grating layer exhibits the same period but has a lower fill factor (LFF) than the structure on top, and has an effective index $n_{\text{eff}} < n_{\text{H}}$. Since the high fill factor (HFF) grating on top does generate higher diffraction orders, referring to Ineq. (2.16), the realization of the LFF grating as an effective medium without higher diffraction orders is not obvious [89]. Only if the fill factor is sufficiently low, no higher diffraction orders are allowed to propagate as required, according to Ineq. (2.17). This criterion can be understood by applying the modal method as introduced in paragraph 2.3.2, which allows to express the electric field inside this T-shaped structure by discrete grating modes. Depending on both, the incidence conditions and the geometry of the grating, an incident plane wave splits into a finite number of these grating modes propagating up- and downward in the grating regions as well as coupling back to the diffraction orders in the outer media.

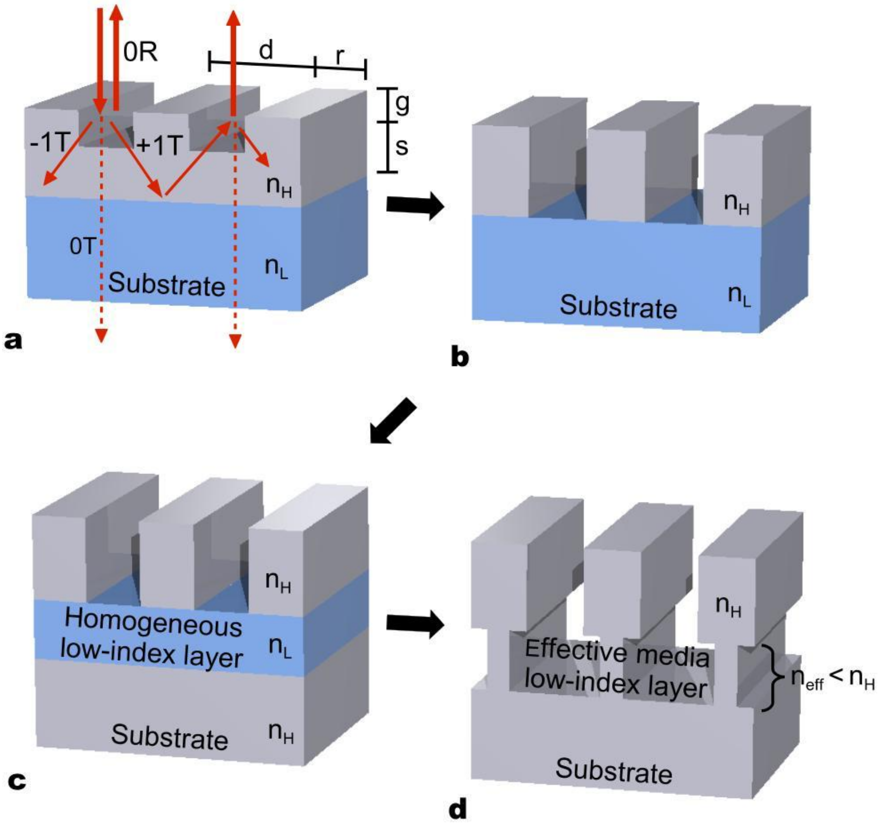

**Fig. 4.1.** Evolution of guided-mode resonant structures. (a) Conventional resonant waveguide grating with a high-index layer corrugated at its surface on top of a low-index substrate. (b) Stand-alone high-index grating ridges corresponding to a zero waveguide layer thickness ($s = 0$ nm). (c) Reduction of the low-index substrate to a thin layer. (d) For the monolithic implementation of the element in (c), the homogeneous low-index layer is replaced by an effective media low-index layer to advance the device to a monolithic reflector.

For grating periods $d$ that fulfill Ineqs. (2.15)-(2.17), we are in a subwavelength regime where only a few discrete grating modes are allowed to propagate as determined by the transcendent Eqs. (2.43) for TE-polarized and (2.44) for TM-polarized light, respectively. Besides the period, these equations also include the widths $r$ and $w$ of both, the grating ridges and grooves, respectively, that can also be expressed by the fill factor $f = r/d$. The larger the ridge width $r$ or rather the fill factor $f$ in Eqs. (2.43) and (2.44) the larger the amount of propagating discrete grating modes. Figure 4.2 illustrates a grating mode formation when a plane wave is incident upon a T-shaped grating with a period in the abovementioned regime. For such a period, it is possible to find a sufficiently low fill

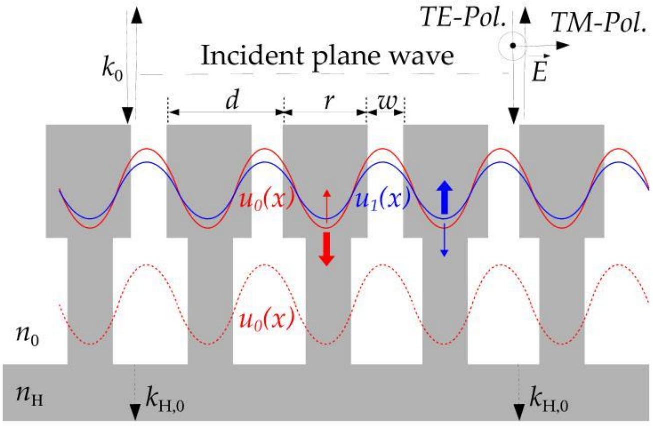

**Fig. 4.2.** Discrete grating modes in a T-shaped subwavelength grating. For resonant reflection, the fill factors of both gratings must be chosen such that the lower grating only supports the fundamental grating mode $u_0(x)$ whereas the upper grating allows for at least one higher order mode $u_1(x)$ to propagate.

factor of the LFF grating so that it only supports the fundamental grating mode $u_0(x)$ (which is related to the zeroth diffraction order in case of a homogeneous layer) whereas for the HFF grating a sufficiently large fill factor indeed allows for one higher order mode $u_1(x)$ to propagate. Due to the change of the modes' effective indices the coupling of this higher order mode to the fundamental mode in the LFF grating will be much weaker than the coupling between both fundamental modes indicated by the arrows. Therefore, the higher order grating mode is mainly reflected back at the interface between both grating regions. It will be resonantly excited which conforms to the necessary conditions of resonant reflection from section 2.3.2. Similar to a conventional homogeneous layer, the remaining fundamental mode can show complete destructive interference for all light transmitted to the LFF grating. For this, the depth of the HFF grating must provide a one-way travel phase shift of $\pi$ between the fundamental and the higher order mode. Thus, the monolithic T-shaped grating, as depicted in Fig. 4.1(d), can reach 100 % reflectivity for some wavelength if the fill factors and the groove depths of both gratings involved meet certain values. As a matter of course, our approach is applicable to all dielectric materials and wavelength regions in theory provided the material is transparent at the desired wavelength.

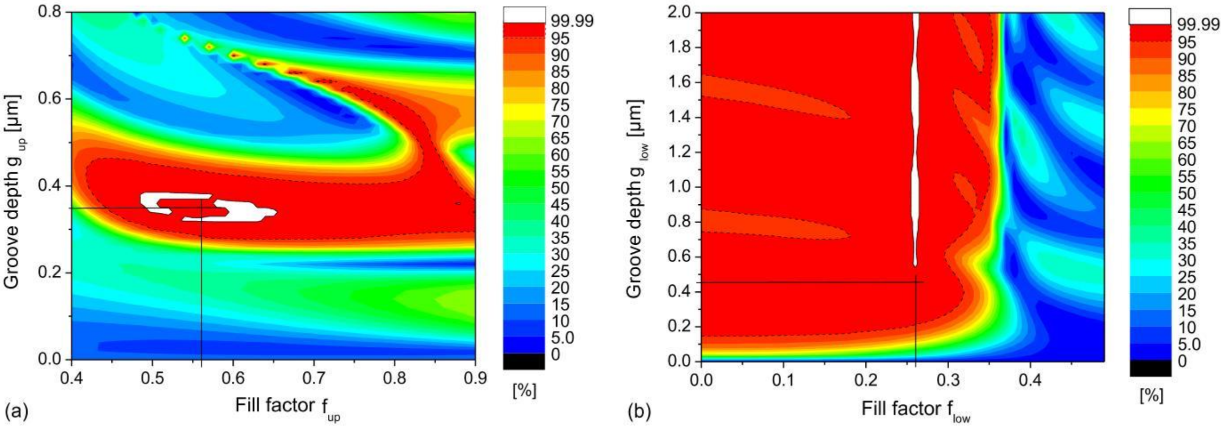

**Fig. 4.3.** (a) Reflectivity over fill factor $f_{\mathrm{up}}$ and groove depth $g_{\mathrm{up}}$ for fixed parameters $f_{\mathrm{low}} = 0.25$ and $g_{\mathrm{low}} = 2\,\mu\mathrm{m}$; (b) reflectivity over fill factor $f_{\mathrm{low}}$ and groove depth $g_{\mathrm{low}}$ for fixed parameters $f_{\mathrm{up}} = 0.56$ and $g_{\mathrm{up}} = 350\,\mathrm{nm}$.

## 4.2 T-shaped grating in silicon for 1550 nm laser light

This paragraph experimentally demonstrates for the first time a monolithic surface mirror, i.e. a single piece of mono-crystalline silicon with a reflectivity high enough to form a laser cavity with a finesse of almost 3000. Since no material is added to the silicon substrate, the currently limiting coating Brownian thermal noise as found in Ref. [15, 21] is completely avoided. A coating related reduction of substrate Q-factors should also be greatly avoided as suggested by first experimental results [24]. Furthermore, our approach uses a *broadband* guided optical mode and therefore does not increase the interaction length of light with matter thus keeping thermorefractive noise as well as absorption low.

### 4.2.1 Grating design considerations

Being the most promising candidate for the substrate material of future high-precision setups, we consider a crystalline silicon surface. We calculate the parameters of a monolithic surface having nearly 100 % reflectivity for TM-polarized light (electric field vector oscillating perpendicular to the grating ridges) at a wavelength of 1550 nm for normal incidence, assuming a refractive index of $n_{\mathrm{H}} = 3.5$. In case of a very low fill factor of the LFF grating, the effective index approaches $n_{\mathrm{eff}} \rightarrow 1$. According to Ineqs. (2.16) and (2.17), we find $443\,\mathrm{nm} < d < 1550\,\mathrm{nm}$. Here, we chose a grating period of $d = 700\,\mathrm{nm}$.

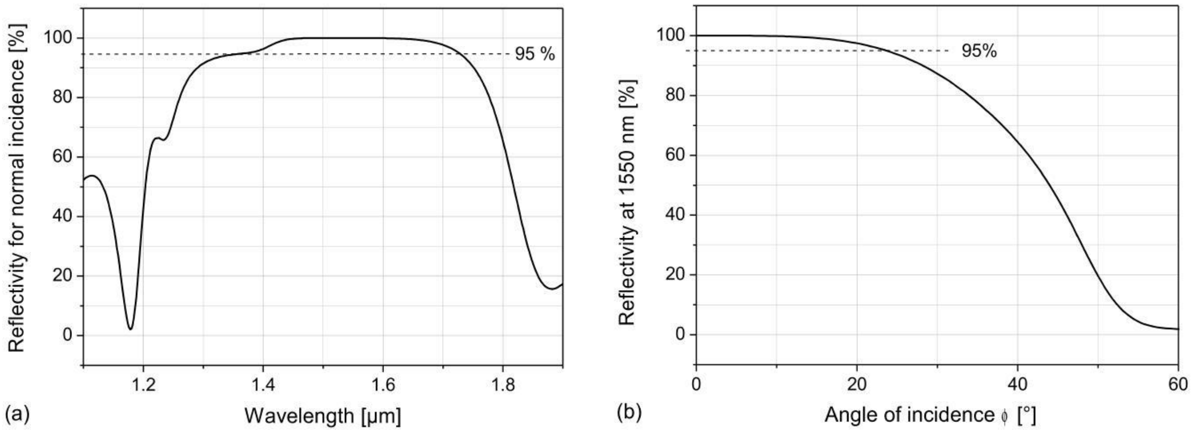

**Fig. 4.4.** (a) Spectral and (b) angular behavior of the reflectivity for the parameters given in Eqs. (4.1).

By means of rigorous simulations [79] the four parameters of both grating regions (fill factor $f_{\mathrm{up}}$ and $f_{\mathrm{low}}$, groove depth $g_{\mathrm{up}}$ and $g_{\mathrm{low}}$) can be derived. The parameter set was further optimized to get a high first-order diffraction efficiency and, thus, broadband guided optical modes as well as large parameter tolerances for the fabrication process.

For fixed start parameters of the lower grating ($f_{\mathrm{low}} = 0.25$, $g_{\mathrm{low}} = 2\,\mu\mathrm{m}$), the upper one was optimized by simultaneously varying $f_{\mathrm{up}}$ and $g_{\mathrm{up}}$ in the ranges from $0.4 < f_{\mathrm{up}} < 0.9$ and $0 < g_{\mathrm{up}} < 800\,\mathrm{nm}$, respectively. The resulting reflectivity is plotted in Fig. 4.3(a), revealing regions with a nearly perfect reflectivity (99.99 % up to 100 %) indicated by the solid line. A highly beneficial design point is $(f_{\mathrm{up}};g_{\mathrm{up}}) = (0.56;350\,\mathrm{nm})$ where high reflectivity as well as convenient fabrication tolerances are found. In order to examine the fabrication tolerances of the lower grating for the found design point, its parameters were varied as well ranging from $0 < f_{\mathrm{low}} < 0.5$ and $0 < g_{\mathrm{low}} < 2\,\mu\mathrm{m}$, respectively. The plotted reflectivity in Fig. 4.3(b) displays a wide range of high reflectivity and supports the theoretical considerations of the preceding paragraphs. For a fill factor smaller than about 0.3, the lower grating only supports the fundamental mode and a minimal groove depth can be found which prevents evanescent transmission of higher grating modes to the substrate. In this case, a depth of $g_{\mathrm{low}} = 430\,\mathrm{nm}$ ensures both, high reflectivity as well as a practical aspect ratio of the grating ridges. The most beneficial parameter values arising from the simulation for TM-polarized light are, at a glance:

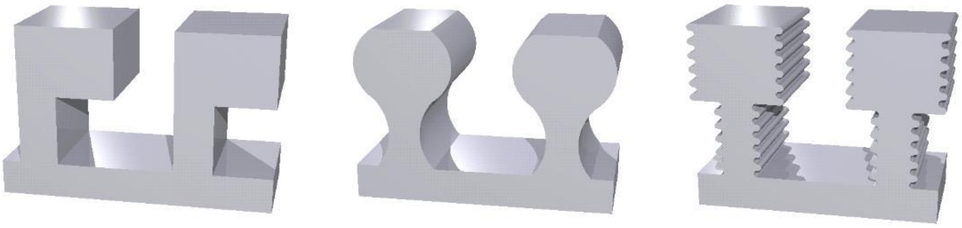

**Fig. 4.5.** Due to the large parameter tolerances which can be extracted from the design results in Fig. 4.3, the grating profile is not severely limited to a rectangular shape. It may vary arbitrarily within the tolerances predicting a certain desired high reflectivity.

$$\begin{array}{rcl} n_\mathrm{H} & = & 3.5 \\ \lambda & = & 1550\,\mathrm{nm} \\ \phi & = & 0^\circ \\ d & = & 700\,\mathrm{nm} \end{array} \quad \Longrightarrow \quad \begin{array}{rcl} f_\mathrm{low} & = & 0.26 \\ g_\mathrm{low} & \geq & 430\,\mathrm{nm} \\ f_\mathrm{up} & = & 0.56 \\ g_\mathrm{up} & = & 350\,\mathrm{nm}. \end{array} \tag{4.1}$$

The simulated angular and spectral properties of the device are shown in Fig. 4.4(a) and (b), revealing a 95 % reflectivity for a broad wavelength range of $(1550 \pm 175)$ nm and an angle of incidence of $\phi = (0 \pm 23)^\circ$. The reflectivity even exceeds a value of 99.99 % for $1.48\,\mu\mathrm{m} < \lambda < 1.58\,\mu\mathrm{m}$ and $\phi = 0^\circ \pm 4.5^\circ$, respectively. These remarkable wide tolerances of both the spectral/angular behavior as well as the design grating parameters, are evident due to the high index contrast between silicon and air as described in section 2.3 by Eqs. (2.30) and (2.32). This leads to a strong coupling into the higher order grating modes and, thus, a large resonance spectral bandwidth.

Accordingly, as a great benefit for the fabrication process (which can be extracted from

| | Deviation from the design values [nm] | | |
|---|---|---|---|
| Reflectivity [%] | groove depth $g_\mathrm{up}$ | ridge width $r_\mathrm{up}$ | ridge width $r_\mathrm{low}$ |
| $> 99.999$ | ± 15 | ± 19 | ± 1.5 |
| $> 99.99$ | ± 22 | ± 30 | ± 3.5 |
| $> 99.9$ | ± 35 | ± 52 | ± 10 |
| $> 99$ | ± 57 | ± 107 | ± 60 |

**Tab. 4.1.** Tolerances for the parameters of the design T-shaped grating as given in Eqs. (4.1).

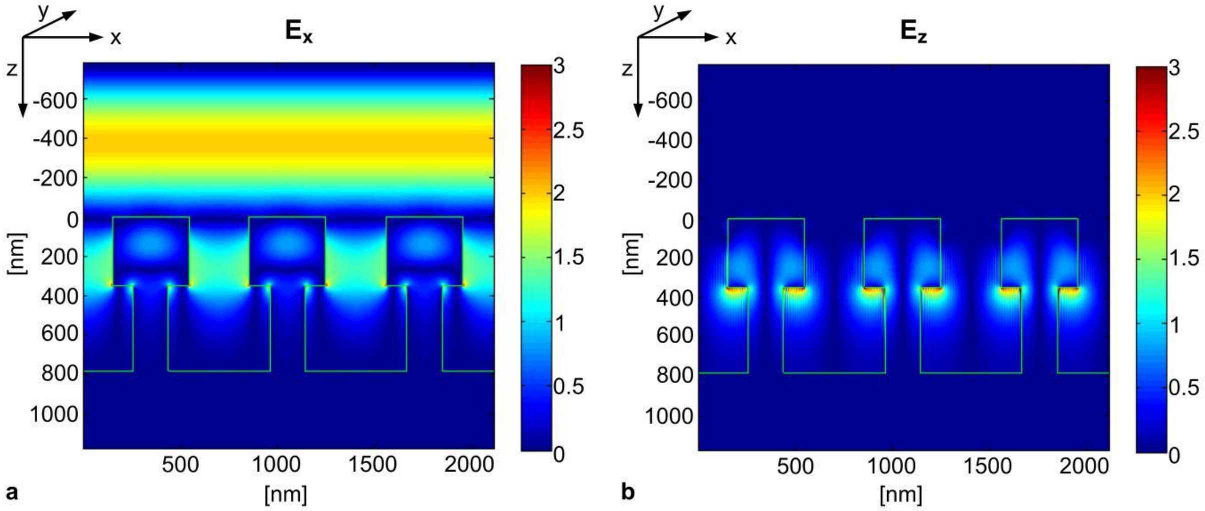

**Fig. 4.6.** Optical near field for the silicon design grating structure. Rigorous-Coupled-Wave Analysis (RCWA) optical near field calculation of the x-component (a) and the z-component (b) of the electric field vector for the design monolithic surface structure. For our simulation, a normally incident plane wave of TM-polarized light with a wavelength of 1550 nm was assumed.

Fig. 4.3 and Tab. 4.1), the grating profile is not severely limited to a rectangular shape. It may vary arbitrarily within the tolerances predicting a certain desired high reflectivity, as indicated by Fig. 4.5. The exact parameter tolerances around the found design point given in Eqs. 4.1 are specified in Tab. 4.1. Here, the deviations of the groove depth $g_{\mathrm{up}}$, the ridge width $r_{\mathrm{up}}$, and the ridge width $r_{\mathrm{low}}$ from their design values which ensure different degrees of high reflectivity ($> 99\,\%$, $> 99.9\,\%$, $> 99.99\,\%$, $> 99.999\,\%$) are calculated in nanometers. As expected from Fig. 4.3(a), the tolerances for both parameters of the upper grating region (groove depth $g_{\mathrm{up}}$ and ridge width $r_{\mathrm{up}}$) are of comparable dimension and are quite large even for a reflectivity higher than 99.999 % with values of ± 15 nm and ± 19 nm, respectively. In contrast, quite low appears the tolerance for the ridge width of the lower grating $r_{\mathrm{low}}$ for reflectivities close to unity. This is most likely due to a very high sensitivity of the resonance condition to the relation between the grating modes' effective indices in both grating regions which are determined by the fill factors. However, once any parameter deviations of a manufactured sample are observed, state-of-the-art etching technologies may serve as a careful post-fabrication treatment to trim the lower grating fill factor with nanometer accuracy.

For the designed T-shaped grating structure that forms the monolithic surface mirror, the optical near field was calculated to demonstrate its theoretical capability of perfectly reflecting normally incident light. This was done by using the numerical implementation of the Rigorous-Coupled-Wave Analysis (RCWA) by L. Li [78] assuming again TM-polarized light with a wavelength of 1550 nm. The incoming light is considered as a plane wave. Figure 4.6(a) shows the x-component of the electric field distribution $E_x$ being the polarization of the incident electric field vector in our case. It reveals the resonantly excited first discrete grating mode to be located at the upper part of each grating ridge whereas the fundamental mode cancels to zero in the substrate ($E_x = 0$). Due to the excitation of "higher diffraction orders" in the upper grating traveling also along the x-direction, $E_z$ is not vanishing. It is displayed in Fig. 4.6(b) with a slight electric field enhancement at the interface of both grating regions but has, however, a value of zero in the substrate corresponding to zero transmission.

### 4.2.2 Fabrication process

For fabrication, a standard silicon wafer with 100 mm in diameter was thermally oxidized with a 1 $\mu$m silica layer and coated with a 80 nm chromium layer, both serving as the mask during the silicon etching process. After spin-coating an electron beam sensitive (chemically amplified) resist on top, the 700 nm period grating was defined by means of electron beam lithography for an area of (7.5 x 13) mm$^2$, aiming at a grating fill factor of 0.56. The developed binary resist profile was then transferred into the chromium layer and subsequently into the oxidized silica layer as well as the silicon bulk substrate by utilizing an anisotropic (i.e. binary) ICP (Inductively-Coupled-Plasma) dry etching process. Here,

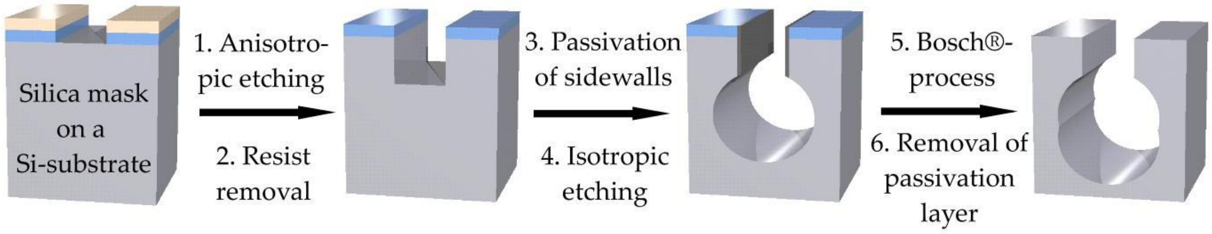

**Fig. 4.7.** Schematic of the stepwise fabrication process for the realization of a subwavelength silicon T-shaped grating.

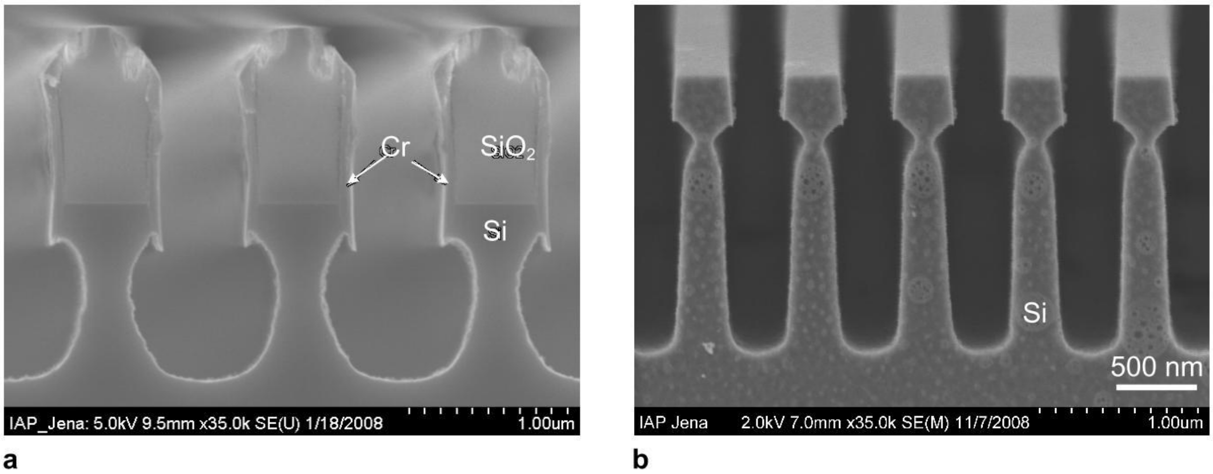

**Fig. 4.8.** Monolithic mirror from a nanostructured single silicon crystal. (a) SEM (scanning electron microscope) cross-sectional view of a grating resulting from the first fabrication trials showing the silica etching mask and the chromium passivation layer at the groove side walls. (b) SEM cross-sectional view of a 700 nm period T-shaped grating in a silicon bulk substrate that forms the monolithic cavity mirror's surface, efficiently reflecting normally incident light with a wavelength of 1.55 $\mu$m.

the etching time was adjusted to match the desired groove depth of the upper silicon grating of about 350 nm. The vertical grating groove side walls were then covered with a thin chromium layer by coating the whole device under an oblique angle. By using this technique, the groove side walls were protected from further ICP etching while the groove bottom remained accessible. A second but this time isotropic (i.e. polydirectional) ICP etching process enabled the undercut of the upper grating to generate the low fill factor grating beneath. For this, a well balanced ratio between horizontal and vertical etching rate played a decisive role to supply a sufficiently low grating fill factor ($< 0.3$) as well as a minimum groove depth of the lower grating of about 500 nm to satisfy the design requirements. Finally, the etching mask materials (silica, chromium, and resist) were removed by means of wet chemical etching baring the mono-crystalline silicon surface structure. The stepwise fabrication process is illustrated in Fig. 4.7.

Figure 4.8(a) depicts an SEM (scanning electron microscope) cross-sectional view on a grating resulting from the first fabrication trials showing the silica etching mask and the chromium passivation layer at the groove side walls. At this stage, we were somehow able to generate a T-shaped profile, yet exhibiting geometric parameters far away from the

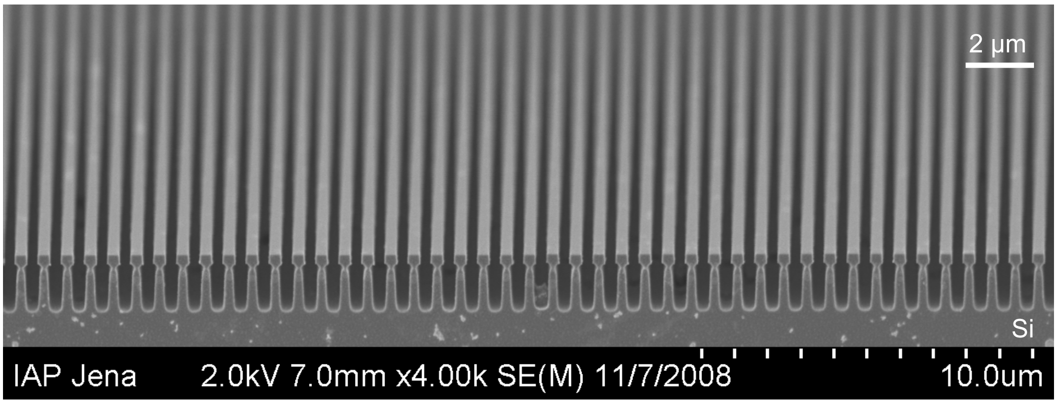

**Fig. 4.9.** The SEM image shows a 32 $\mu$m wide section of the monolithic grating mirror that has been fabricated and characterized within this work. After the 700 nm T-shaped grating was etched into the silicon bulk substrate, the monolithic mirror was fractured into two pieces. The bright spots on the cross-sectional surface arose from debris during fracturing.

design values. After having passed an extensive technology development, Fig. 4.8(b) shows an SEM image on a fabricated mirror surface that has finally been characterized within this work. As expected the shape of the grating ridges was still not strictly rectangular, but it was within the parameter tolerances that predict high reflectivity as will be confirmed by the experimental results in the following section.

The monolithic cavity mirror that has been fabricated and characterized in this work has a nanostructured surface area of (7.5 x 13) mm$^2$. The reflectivity over the complete surface shows a great homogeneity as also outlined in the following experimental paragraph. Figure 4.9 provides a visual impression of the homogeneity of our mirror by showing an SEM picture of a 32 $\mu$m wide cross-section of the mirror surface.

### 4.2.3 Experimental characterization

The first measurement of the mirror's reflectivity was performed under normal incidence $(0 \pm 1)^\circ$ and employed a fiber coupled tunable diode laser together with the experimental setup as described in paragraph 3.2 and displayed in Fig. 3.9. The measured data is shown in Fig. 4.10(a) (black curve) and reveals a reflectivity of higher than 91.5 % for a rather broad spectral range from approximately 1.21 $\mu$m to 1.61 $\mu$m. The peak reflectivity is located close to the design wavelength of 1.55 $\mu$m with a value of almost 100 % where a

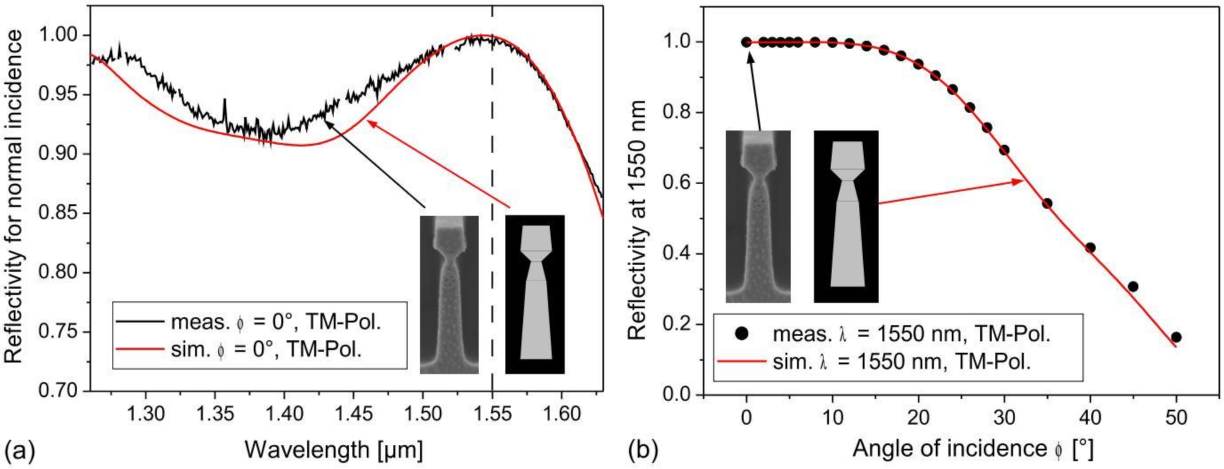

**Fig. 4.10.** Measured (a) spectral reflectivity for normal incidence ($\phi = 0 \pm 1)^\circ$ as well as (b) angular reflectivity at $\lambda = 1550\,\text{nm}$ (black curve and dots) of the grating from Fig. 4.8(b) and rigorously simulated (a) spectral as well as (b) angular reflectivity for a grating profile approximating the real shape by a trapezoidal fragmentation (red curves).

measurement error of $\pm\,0.5\,\%$ needs to be taken into account. Within a second experiment, the reflectivity for incidence angles between 0° and 50° was obtained for a fixed wavelength of 1550 nm and is plotted in Fig. 4.10(b) (black dots). In good agreement with the design curve from Fig. 4.4(b), the reflectivity exceeds a value of 95 % for incidence angles up to 19° and shows its maximum around zero degree with a value close to unity. The red curves in Fig. 4.10 represent a rigorously simulated (a) spectral and (b) angular response for a grating profile that has been formed by a trapezoidal fragmentation in order to approximate the real shape from Fig. 4.8(b) (indicated by the sketches on the bottom of Figs. 4.10(a) and (b)).

In order to demonstrate the high optical quality of the monolithic mirror it was incorporated as the end mirror in a standing-wave Fabry-Perot resonator, see Fig. 4.11 for a simplified sketch of the experimental setup. In analogy to the first cavity measurement of the tantala based RWG whose results are presented in paragraph 3.1, this experiment was performed at the Institute of Gravitational Physics, University of Hanover, in close collaboration. In contrast to the setup in Fig. 3.3, here a conventional high quality multilayer coated mirror served as the coupling mirror. Note that the monolithic mirror substrate had an unpolished rear surface and could not be used as the coupling mirror. By measur-

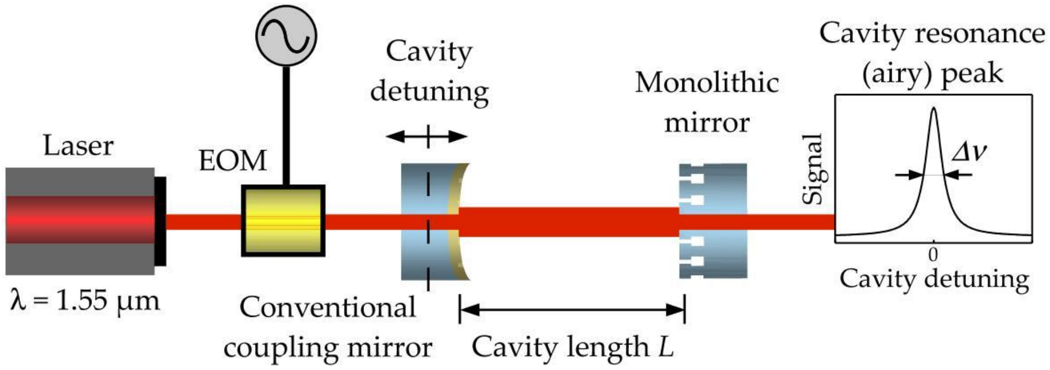

**Fig. 4.11.** Simplified sketch of the experimental setup for the characterization of the monolithic waveguide grating as the end mirror of a high-finesse Fabry-Perot cavity. Electro-optical modulator (EOM). For more details see [46].

ing the cavity's finesse $F$, this setup also enabled us to precisely determine the mirror's reflectivity under an angle of incidence of precisely zero degree at the design wavelength of 1550 nm. Please be reminded that the product of the amplitude reflectivities $\rho_{12} = \rho_1\rho_2$ of coupling mirror and end mirror, respectively, can be calculated from the cavity's finesse according to Eq. (3.1).

In order to obtain the linewidth and subsequently the finesse of the linear Fabry-Perot resonator, again a calibrated detuning of the cavity length around an airy peak was used. Though the rear surface of the monolithic end mirror was unpolished the signal could be measured in transmission of the cavity. The calibration was done via frequency markers around an airy peak using the Pound-Drever-Hall (PDH) technique [87]. Similarly to the cavity setup containing the tantala RWG, a phase modulation was imprinted on the light by an electro-optical modulator (EOM) for this pupose. For more details concerning the cavity measurement and the measured data, the reader is referred to [46]. A total of 25 beam positions on the grating over an area of $4\,\mathrm{mm}^2$ with a beam size radius of $\approx 50\,\mu$m had been investigated. For each position 12 measurements of the linewidth were done which resulted in an averaged value of the power reflectivity of $\bar{\rho}_2^2 = (99.7682 \pm 0.0095)\%$ for the overall area. The smallest linewidth was determined to $\Delta\nu = (2.24 \pm 0.07)$ MHz. Hence, the finesse was found to be $F = 2784 \pm 100$ which corresponds to a waveguide grating power reflectivity of $\rho_2^2 = (99.7945 \pm 0.0086)\%$, referring to Eq. (3.1). Due to the unpolished back side of the substrate only a lower limit on the transmission could be set by means of power measurements of $\tau_2^2 \geq (230 \pm 20)$ ppm and, hence, an upper limit on optical losses due to absorption and scattering of $(1820 \pm 110)$ ppm.

### 4.2.4 Summary and discussion

The optical reflectivity measured here is, to the best of our knowledge, the highest resonant reflection ever realized. The measured reflectivity of slightly below unity is attributed to deviations of the fabricated grating as shown in Fig 4.8(b) from the design parameters. In our case, the fill factor fluctuation of the lower grating can be assumed as the crucial factor according to the tight tolerances from Tab. 4.1. However, the measurements are in very good agreement with our rigorous model based on Maxwell equations that takes these deviations into account (Fig. 4.10). Please note that the same simulations (red curves in Figs. 4.10(a) and (b)) predict a reflectivity maximum for a wavelength of about $1.543\,\mu$m (at angle of incidence 0°) or an angle of incidence of about 7° (at 1550 nm). Unfortunately, a verification in our cavity setup was not possible since neither the laser source was tunable to this wavelength nor the equipment for a stable high-finesse ring cavity was available.

The reflectivity as demonstrated here in principle allows for a coating free linear cavity with a finesse of $\approx 1500$ which already reaches the regime of finesse values used in gravitational wave detectors. For example, the Advanced LIGO Fabry-Perot arm cavities are being designed for a finesse of a few hundred. Our demonstrated monolithic mirror quality may also be already sufficient to provide an impact towards reaching the quantum regime of micro-mechanical oscillators. In Ref. [8] optical cooling of a micro-mechanical oscillator down to 135 mK was achieved with a finesse of only 200. Our demonstrated cavity linewidth of 2.24 MHz is significantly smaller than many typical fundamental oscillator frequencies and the so-called good cavity regime can be reached [9]. Note that the cavity linewidth can be further reduced by increasing the cavity length. For applications in reference cavities and optical clocks [12,13] the reflectivity should be further increased beyond the value demonstrated here. However, we expect that indeed considerable improvements towards a perfect reflectivity are possible with improved electron beam lithography and etching technologies.

## 4.3 T-shaped grating in lithium niobate for 1064 nm laser light

Besides providing high reflectivity, the nature of resonant light excitation in RWGs implies a local electric field enhancement in the high-index corrugated layer or grating ridges, respectively. This can be controlled via the finesse of the RWG (as defined by Eq. (2.35)) or rather the diffraction efficiency into the waveguide modes. Such a local field enhancement might be exploited for light-matter interactions that scale with intensity such as nonlinear optical effects. A common way to localize and intensify electromagnetic fields is to excite plasmons on metal surfaces or particles. Surface plasmons enhance second-harmonic generation (SHG) from solid films by several orders of magnitude [93]. Similarly, metal nanoparticles arranged in ordered patterns can give rise to a nonlinear response due to particle plasmons which can be improved by introducing additional features such as gaps between the particles [94]. However, metallic losses can be problematic when the sample is illuminated by a bright laser beam or transmitted light needs to be detected. In order to provide an all-dielectric and thereby transparent configuration, RWGs have been successfully employed to enhance the weak surface SHG of a fused silica substrate by a factor of up to 5000 [95, 96]. In this case, a silica grating was covered by a high-index titanium dioxide layer, and it was optimized for the fundamental wavelength of 1064 nm. Polarization dependence of the SH response suggested that the enhancement arose from the favorable interaction of the strong local field of the resonant waveguide mode with the inherent surface nonlinearity of the dielectric materials.

In this chapter we propose to combine the local field enhancement of RWGs with inherent strong nonlinearity of an active $\chi_2$-material instead of weak surface nonlinearity as demonstrated in Refs. [95, 96]. This suggests a remarkable increase in total SHG yield. Possessing a high refractive index of $n = 2.23$ for 1064 nm laser light and a large nonlinear coefficient $\chi_2$, lithium niobate appears as a suitable candidate for the high-index as well as nonlinear material of choice. Due to its wide usage in the field of integrated optics, lithium niobate is a well established nonlinear crystalline material with well known optical constants as well as international standards for crystal growth and processing, and is chosen here for the following considerations. For a maximum overlap of resonant light excitation induced local field enhancement and nonlinear matter, we suggest to utilize the monolithic T-shaped grating as introduced within this chapter. Therefore, the following paragraph theoretically investigates the capability of a nanostructured lithium niobate surface of efficiently reflecting 1064 nm laser light with special remarks on the local electric field enhancement in this structure. The final paragraph will present a promising approach for the lithium niobate structuring which is based on a versatile technique called Ion-Beam-Enhanced Etching (IBEE) [97, 98].

### 4.3.1 Grating design considerations

For the rigorous deduction of the design parameters of a monolithic surface having nearly 100 % reflectivity at a wavelength of 1064 nm, we consider a crystalline lithium niobate surface in a similar manner as for the silicon surface in paragraph 4.2.1. Assuming TM-polarized light impinging under normal incidence, the anisotropy of a lithium niobate crystal implies to use the ordinary refractive index with $n_{\mathrm{H}} = 2.23$. In case of a very low fill factor of the LFF grating, the effective index approaches $n_{\mathrm{eff}} \to 1$. According to Ineqs. (2.16) and (2.17), we find $477\,\mathrm{nm} < d < 1064\,\mathrm{nm}$. Again, we chose a grating period of $d = 700\,\mathrm{nm}$. By means of rigorous simulations [79] the four parameters of both grating regions (fill factor $f_{\mathrm{up}}$ and $f_{\mathrm{low}}$, groove depth $g_{\mathrm{up}}$ and $g_{\mathrm{low}}$) can be derived. The parameter set was further optimized to get a high first-order diffraction efficiency and, thus, broadband guided optical modes as well as possibly large parameter tolerances for the fabrication process. Of course, this is contrary to a maximum electric field enhancement and a compromise needs to be found between optical function and technical feasibility.

For fixed start parameters of the lower grating ($f_{\mathrm{low}} = 0.25$, $g_{\mathrm{low}} = 2\,\mu\mathrm{m}$), the upper one was optimized by simultaneously varying $f_{\mathrm{up}}$ and $g_{\mathrm{up}}$ in the ranges from $0.4 < f_{\mathrm{up}} < 0.8$ and $200\,\mathrm{nm} < g_{\mathrm{up}} < 600\,\mathrm{nm}$, respectively. The resulting reflectivity is plotted in Fig. 4.12(a), revealing regions with a nearly perfect reflectivity (99.99 % up to 100 %) indicated by the solid line. A highly beneficial design point is $(f_{\mathrm{up}};g_{\mathrm{up}}) = (0.56;400\,\mathrm{nm})$ where high reflectivity as well as convenient fabrication tolerances are found. In order to examine the fabrication tolerances of the lower grating for the found design point, its parameters were varied as well ranging from $0 < f_{\mathrm{low}} < 0.5$ and $0 < g_{\mathrm{low}} < 2\,\mu\mathrm{m}$, respec-

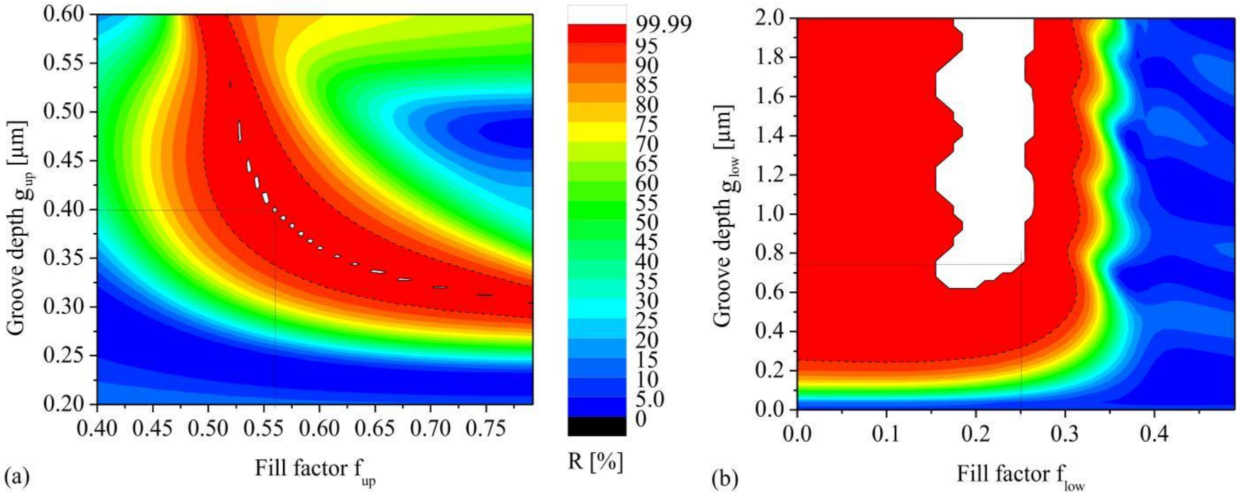

**Fig. 4.12.** (a) Reflectivity over fill factor $f_{\mathrm{up}}$ and groove depth $g_{\mathrm{up}}$ for fixed parameters $f_{\mathrm{low}} = 0.25$ and $g_{\mathrm{low}} = 2\,\mu\mathrm{m}$; (b) reflectivity over fill factor $f_{\mathrm{low}}$ and groove depth $g_{\mathrm{low}}$ for fixed parameters $f_{\mathrm{up}} = 0.56$ and $g_{\mathrm{up}} = 400\,\mathrm{nm}$.

tively. The plotted reflectivity in Fig. 4.12(b) displays a wide range of high reflectivity. For a fill factor smaller than about 0.3, the lower grating only supports the fundamental grating mode and a minimal groove depth can be found which prevents evanescent transmission of higher order grating modes to the substrate. The most beneficial parameter values arising from the simulation for TM-polarized light are, at a glance:

$$\begin{array}{rcl} n_{\mathrm{H}} & = & 2.23 \\ \lambda & = & 1064\,\mathrm{nm} \\ \phi & = & 0^{\circ} \\ d & = & 700\,\mathrm{nm} \end{array} \quad \Longrightarrow \quad \begin{array}{rcl} f_{\mathrm{low}} & = & 0.25 \\ g_{\mathrm{low}} & \geq & 750\,\mathrm{nm} \\ f_{\mathrm{up}} & = & 0.56 \\ g_{\mathrm{up}} & = & 400\,\mathrm{nm}. \end{array} \tag{4.2}$$

Please note that the absolute dimensions of the lithium niobate structure ($\lambda = 1064\,\mathrm{nm}$, $n = 2.23$) given in Eqs. (4.2) are quite similar to those in case of silicon ($\lambda = 1550\,\mathrm{nm}$, $n = 3.5$) as given in Eqs. (4.1). This is not surprising since the wavelength to refractive index ratios are almost equal, and it impressively proves the scalability of the T-shaped grating to other wavelength-material combinations. The simulated angular and spectral properties of the lithium niobate design structure are shown in Figs. 4.13(a) and (b), revealing a 95 % reflectivity for a wavelength range of $(1064 \pm 20)\,\mathrm{nm}$ and an angle of incidence of $\phi = (0 \pm 4)^{\circ}$. In comparison to the silicon structure in paragraph 4.2.1, the tolerances of the lithium niobate surface are significantly smaller which is evident due

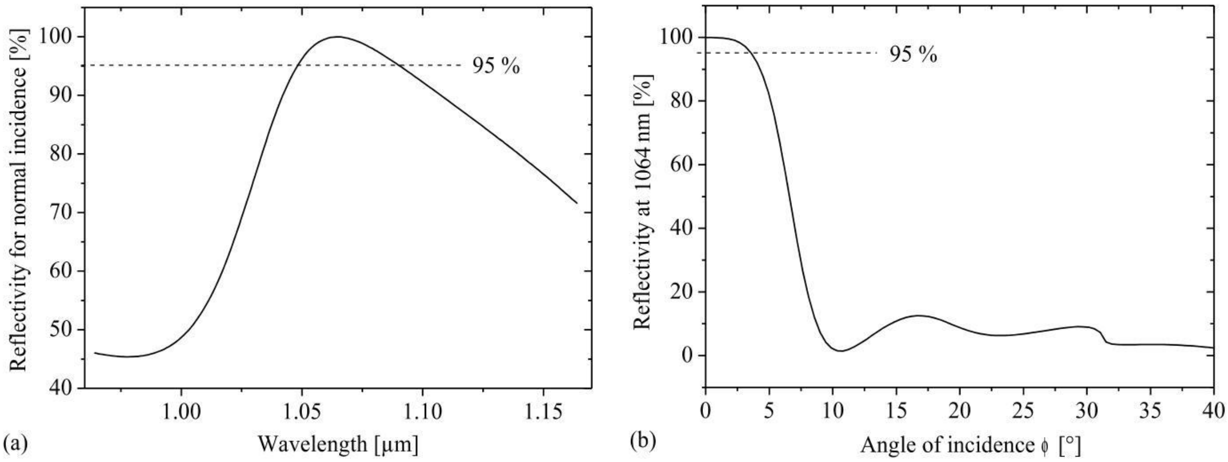

**Fig. 4.13.** (a) Spectral and (b) angular behavior of the reflectivity for the parameters given in Eqs. (4.2).

to the reduced refractive index contrast between lithium niobate and air, as described in section 2.3 by Eqs. (2.30) and (2.32). However, this suggests an increased electromagnetic field enhancement.

For a quantitative evaluation, the optical near field of the design lithium niobate structure was calculated. Similar to the silicon case, this was done by using the numerical implementation of the Rigorous-Coupled-Wave Analysis (RCWA) by L. Li [78], assuming again TM-polarized light with a wavelength of 1064 nm. The incoming light is considered as a plane wave. Figure 4.14(a) shows the x-component of the electric field distribution ($E_x$) being the polarization of the incident electric field vector in our case. It reveals the resonantly excited first discrete grating mode to be located at the upper part of each grating ridge with a local field enhanced by factor of about two, whereas the fundamental mode cancels to zero in the substrate ($E_x = 0$). More interesting with regard to local field enhancement is the part of the electric field vector in the z-direction $E_z$. It is displayed in Fig. 4.14(b) with a local field enhancement factor of about 2.5 in the upper grating ridges and, moreover, a factor of up to four at the interface of both grating regions. Assuming an averaged enhancement of the electric field by a factor of two, the intensity of the SH signal can be increased by a factor of at least 16 compared to a flat reference surface since it scales with the fourth power of the amplitude of the fundamental field.

Please note that the performance of the lithium niobate structure can be improved by using less parameter tolerant designs. For such designs, a likely drop in reflectivity of

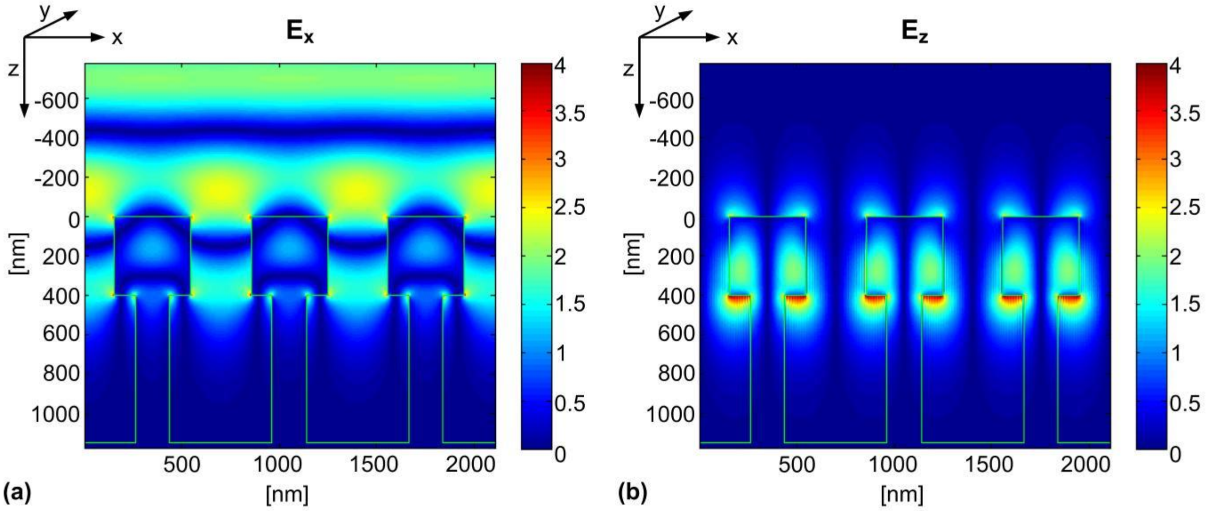

**Fig. 4.14.** Optical near field for the lithium niobate design grating structure. Rigorous-Coupled-Wave Analysis (RCWA) optical near field calculation of the x-component (a) and the z-component (b) of the electric field vector for the design monolithic surface structure. For our simulation, a normally incident plane wave of TM-polarized light with a wavelength of 1064 nm was assumed.

the fundamental field due to a deviation of a fabricated grating from its design profile can be compensated by choosing a different angle of incidence. However, a more detailed analysis goes beyond the scope of this work.

### 4.3.2 Prospects for the fabrication process

Unfortunately, for an experimental realization of a T-shaped grating in lithium niobate, the silicon fabrication procedure as described in paragraph 4.2.2 cannot be applied since an isotropic etch of the perfect crystal is not possible when using standard dry etching recipes. However, in 1979 Kawabe *et al.* found that the etching rate of lithium niobate in diluted HF can be significantly increased when the crystal is damaged by an ion bombardment prior to etching [97]. They proposed to exploit such a contrast in etching rate for structuring the crystal by inducing only local or rather patterned damages. Based on this achievement, a versatile technique for processing lithium niobate crystals has been developed enabling for binary 3D micro- and nanostructures with high resolution and high aspect ratios [99, 100]. The lateral lithium niobate pattern is realized by electron beam

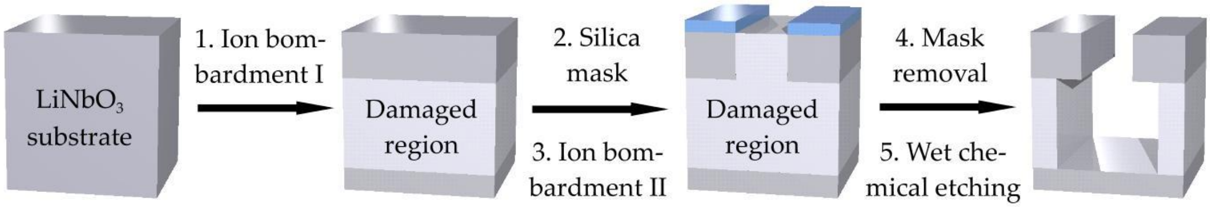

**Fig. 4.15.** Schematic of the stepwise fabrication process for the realization of a subwavelength lithium niobate T-shaped grating.

defined silica or chromium masks of certain minimum thickness that are able to block the incident ions, whereas the vertical profile is controlled by choosing different ion species and/or energies which determine the ion's implantation depth [98]. These findings can in principle be applied to the fabrication of our desired T-shaped grating as displayed in Fig. 4.15 and described in the following:

Starting with a bare lithium niobate substrate, a first ion bombardment should be operated at energies high enough to make the ions travel unaffected for a distance equal to the groove depth of the upper grating. This would cause an ion implantation and thus a homogeneous layer of crystal damage only in a region that is more than about 400 nm below the crystal surface, while the amount of ions absorbed in the upper region is negligible. The range of the ion's implantation depth must be sufficiently large to ensure the minimum groove depth of the lower grating of 750 nm. By means of state-of-the-art deposition, electron beam lithography and etching techniques then a silica mask representing the lateral dimensions of the upper region of the T-shaped grating is attached onto the lithium niobate substrate. The thickness of the silica mask must be chosen such that it is capable of absorbing impinging ions to a certain minimum extent to prevent any crystal damage of the masked regions. Subsequently, a second ion bombardment should be conducted using lower ion energies which results in a crystal damage ranging from the very surface of the crystal down to the bottom of the already damaged layer. The total damaged region will then conform to a layer that embeds unmodified grating ridges. It can be wet chemically etched starting from the top by exposing the lithium niobate substrate to a hydrofluoric (HF) solution. For this process, a well adjusted maximum etching time will be essential in order to prevent a complete underetch of the upper grating ridges. That is, the etching process must be stopped at a point when it touches the bottom interface of the damaged layer to the unmodified bulk crystal. See the picture on the right hand side of Fig. 4.15. For this purpose, a maximum overlap of the irradiated regions of both ion implantation steps is advantageous since the etching rate scales with the degree of crystal damage [98]. Within the lower grating region, this would give a vertical etching rate being larger then the horizontal one which helps reaching the targeted etching profile. After the removal of the silica mask, the lithium niobate surface structure is obtained. Finally, the irradiated ridges of the lower grating that survived the etching process get annealed by exposing the sample to high temperatures of about 500°C in order to recover the optical constants of the bulk material [101].

Please note that the described process is composed of binary substructures which implies to use two ion implantation steps for the realization of an undercut grating such as the T-shape. However, recent findings in the field of lithium niobate structuring promise to get along with only one implantation step after the silica mask (representing the dimensions of the upper grating) had been attached onto the lithium niobate substrate. For this purpose, the ion-matter interaction of the one and only ion implantation step should be modeled such that it generates an undercut profile of the irradiated regions [101]. In this case, an increasing ion scattering with increased ion energy can be exploited. Hence, the larger is the implantation depth, the larger is the width of the damaged region at this depth as desired.

# 5 New approach for monolithic RWGs II - Encapsulated grating

Within the previous chapter we proposed and successfully realized monolithic high-reflection waveguide mirrors with a nanostructured surface to reduce the thermal noise in interferometric measurements. However, the highly complicated grating profile implies a challenging fabrication process as well as severe restrictions in the device handling. Such nanostructured surfaces unfortunately show a very high susceptibility to damage and pollution. In this chapter we propose and demonstrate a second monolithic mirror architecture that is formed by an encapsulated subwavelength grating and also avoids the thick dielectric stack of conventional mirrors [47]. Such a device also creates a resonant waveguide structure but with a flat and robust surface. This configuration offers new benefits for the handling and the fabrication process. Once fabricated the device is protected against mechanical damage and also against contamination since its surface can be cleaned in the same manner as a conventional polished surface. This approach for a monolithic mirror has, to the best of our knowledge, never been suggested before. After presenting the basic idea of this approach in the following section, paragraph 5.2 shows rigorous simulations for a grating that is based on silicon, and demonstrates a first quasi-monolithic encapsulated grating reflector. We measured a promising high reflectivity of 93 % for a wavelength of $\lambda = 1.55\,\mu$m under normal incidence [47]. Finally, a new type of a monolithic narrowband filter in fused silica is proposed whose single resonance wavelength peak can be tuned within a large NIR region by translating the incident beam relative to the grating which has a varying period [48].

## 5.1 Basic idea

Similar to the explanation of the T-shaped grating structure in chapter 4, we use the illustration in Fig. 5.1 to help the reader to understand the theoretical capability of an encapsulated grating of reaching perfect resonant reflection. It shows the stepwise transition from the initial surface corrugated resonant waveguide mirror (a) to, finally, our flat surface grating waveguide mirror as introduced in this chapter. Figure 5.1(b) depicts a configuration of a resonant reflector for a high refractive index material such as silicon ($n = 3.48$ at the wavelength of 1550 nm). In this situation, a low refractive index layer beneath the waveguide grating is indispensable, as presented in paragraph 3.2. This cladding layer needs to have a certain minimum thickness in order to prevent evanescent transmission of higher diffraction orders to the substrate. The waveguide grating in Fig. 5.1(b) can be changed to a flat surface configuration by simply moving the top grating region beneath the waveguide layer as shown in Fig. 5.1(c). In contrast to the elements in (a) and (b), here the resonant waveguide modes are excited by reflected higher diffraction orders as indicated by the light rays.

Similar to the approach in chapter 4, in Fig. 5.1(d) we propose to replace the homogeneous low-index layer in (c) by an *effective* low-index layer (which has an effective index $n_{\mathrm{eff}} < n_{\mathrm{H}}$) thereby enabling a truly monolithic configuration of a resonant reflector with a flat, uncorrugated surface. This effective low-index grating layer needs to exhibit the same period as the grating in Fig. 5.1(c) in order to fulfill Ineqs. (2.15)-(2.17) that allow for resonant reflection in principle. Since it is supposed to generate higher diffraction orders (in reflection), the realization of the introduced grating as an effective medium is not obvious [89]. Here, the same modal description as for the effective layer in the T-shaped grating applies. Only if the grating fill factor is sufficiently low, no higher order discrete grating modes (corresponding to higher diffraction orders) are allowed to propagate to the substrate material as required, according to the transcendent Eqs. (2.43) for TE-polarized and (2.44) for TM-polarized light, respectively, from paragraph 2.3.2. Moreover, the grating layer has to have a certain minimum thickness $g$ to suppress any evanescent transmission of the higher diffraction orders to the substrate that are guided in the cover layer with thickness $s$. Thus, only the fundamental mode in the grating is able to carry

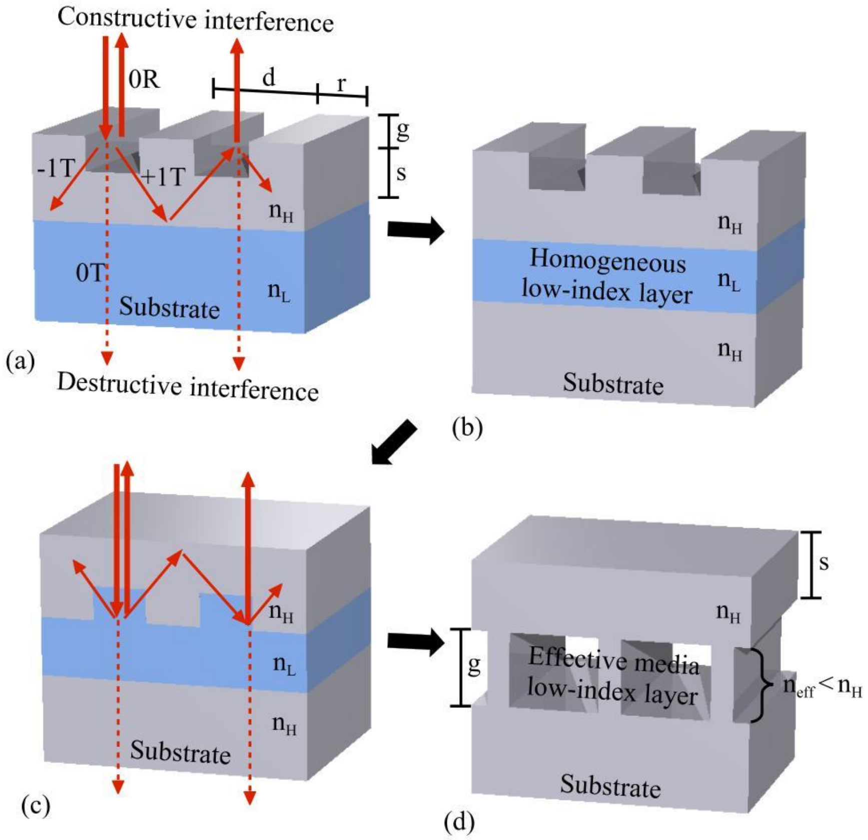

**Fig. 5.1.** (a) Initial waveguide grating configuration and its fundamental principle in a simplified ray picture, (b) reduction of the low-index substrate to a low-index layer, (c) movement of the grating region beneath the waveguide layer to supply a flat surface, (d) replacement of the homogeneous by an effective media low-index layer to provide a purely monolithic mirror architecture. The light rays in (c) illustrate how the waveguide modes are excited in reflection when the grating is beneath the waveguide layer (light rays have been omitted in (b) and (d) for clarity).

some energy to the substrate which, however, interferes destructively at the resonance condition. It should be possible to optimize the monolithic encapsulated grating, as depicted in Fig. 5.1(d), to create 100 % reflectivity.

Please note that, in contrast to the T-shaped monolithic structure, the effective low-index layer of the encapsulated grating mirror plays a double role. On the one hand it acts as the low-index layer suppressing any downward propagation of higher diffraction orders to the substrate, while on the other hand in backward direction it excites waveguide modes propagating through the homogeneous cover layer. From a direct comparison of both monolithic RWG layouts as proposed in this thesis, it is evident that for the encapsulated grating this excitation will be significantly weaker than that for the T-shaped structure. This is due to the weak perturbation of the waveguide layer in case of the encapsulated grating, and will lead to a narrower resonance spectral as well as angular bandwidth (determined by the diffraction coefficient $\eta$) compared to that reached by the T-shaped structure. However, by providing a large refractive index contrast a sufficiently wide bandwidth as well as appropriate fabrication tolerances should be possible.

## 5.2 Encapsulated grating in silicon for 1550 nm laser light

In accordance to the latest findings of thermal noise research, we first consider silicon as the substrate material and 1550 nm laser light in order to realize a monolithic highly reflective mirror for potential application in future high-precision setups. In this paragraph we present a grating design that is based on rigorous simulations, and show that perfect reflectivities are possible in theory. A first demonstrator fabricated from silicon is realized, and our measurement results revealed a promising high reflectivity of 93 % for normal incidence at the design wavelength of $\lambda = 1550$ nm.

### 5.2.1 Grating design considerations

The design parameters of our encapsulated grating reflector were optimized for a broad resonance behavior and for large fabrication tolerances using a Rigorous-Coupled-Wave Analysis (RCWA) [79]. In case of a very low fill factor of the encapsulated grating, the effective index approaches $n_{\text{eff}} \to 1$. According to Ineqs. (2.15)-(2.17), the grating period $d$ has to be greater than 443 nm and smaller than 1550 nm since we are interested in a high reflectivity of laser light with the wavelength of $\lambda = 1550$ nm impinging under normal incidence. We chose a grating period of $d = 800$ nm being well within this regime and TE-polarized light (electric field vector oscillating parallel to the grating ridges). Figure 5.2(a) shows the calculated reflectivity of the encapsulated grating reflector versus the thickness of the top waveguide layer $s$ ranging from 300 nm to 390 nm for fixed values of the fill factor ($f = 0.4$) and the groove depth ($g = 2\ \mu$m). The plot reveals a reflectivity of

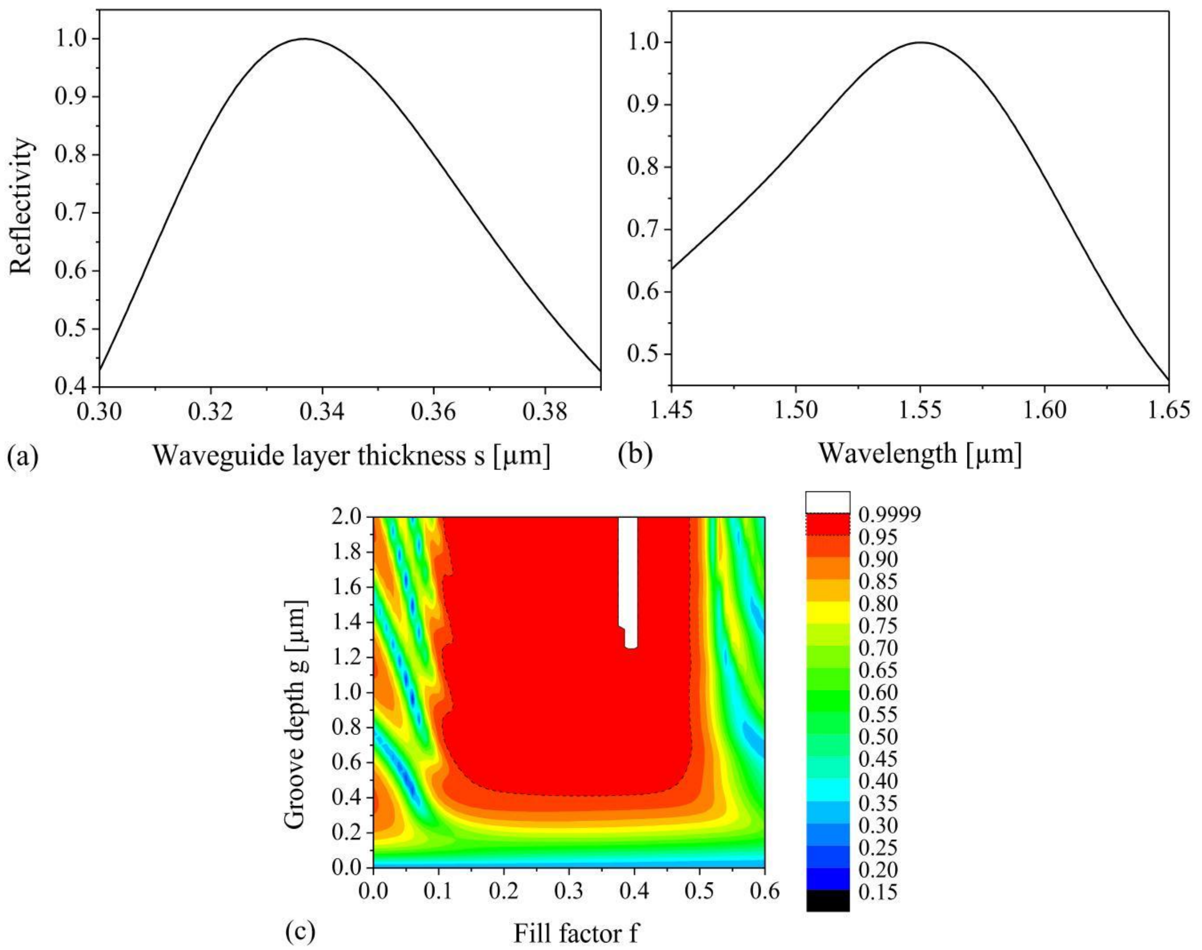

**Fig. 5.2.** (a) Calculated reflectivity versus thickness of the top waveguide layer $s$ for fixed values of $d = 800\,\text{nm}$, $f = 0.4$, and $g = 2\ \mu\text{m}$, assuming TE-polarization and normal incidence of light at $\lambda = 1550\,\text{nm}$. (b) Calculated spectral reflectivity for the grating design parameters given in Eqs. (5.1). (c) Calculated reflectivity over fill factor $f$ and groove depth $g$ for $s = 337\,\text{nm}$.

greater than 95 % in the range of $327\,\text{nm} < s < 347\,\text{nm}$ and a value of close to unity ($>$ 99.99 %) for a thickness of $s = 337\,\text{nm}$. Since in our case the coupling efficiency to the waveguide modes by reflected higher diffraction orders is pretty weak, the tolerance of the top high-index layer thickness $s$ is rather low.

In order to optimize the fabrication tolerances of the encapsulated grating for the design thickness of $s = 337\,\text{nm}$, fill factor and groove depth were varied simultaneously ranging from $0 < f < 0.6$ and $0 < g < 2\ \mu\text{m}$, respectively. The plotted reflectivity in Fig. 5.2(c) reveals a wide range of high reflectivity with values $> 95\,\%$ as indicated by the dashed line.

Values even exceeding 99.99 % are within the white area. This plot clearly supports the theoretical considerations of the preceding paragraph. For a fill factor smaller then about 0.5, the grating only supports the fundamental mode and a minimal groove depth can be found which is required in order to prevent evanescent transmission of higher grating modes to the substrate. If the fill factor is approaching 0.1, the excitation of waveguide modes is too weak to allow for a high resonant reflection.

The optimum encapsulated grating parameter values arising from our rigorous calculations are, at a glance:

$$\begin{array}{rcl} n_{\mathrm{H}} & = & 3.48 \\ \lambda & = & 1550\,\mathrm{nm} \\ \phi & = & 0^\circ \\ d & = & 800\,\mathrm{nm} \end{array} \quad \Longrightarrow \quad \begin{array}{rcl} f & = & 0.4 \\ g & = & 1300\,\mathrm{nm} \\ s & = & 337\,\mathrm{nm}. \end{array} \tag{5.1}$$

Figure 5.2(b) shows the simulated spectral response of the design grating device, revealing a 95 % reflectivity for a rather broad wavelength range of 1550 nm ± 25 nm. For the designed encapsulated grating structure, the optical near field was calculated to demonstrate its theoretical capability of perfectly reflecting normally incident light. This was done by using a Rigorous-Coupled-Wave Analysis (RCWA) [78] assuming TE-polarized light with a wavelength of 1550 nm. The incoming light is considered as a plane wave. Figure 5.3 shows the y-component of the electric field distribution $E_y$ being the polarization of the incident electric field vector in our case. As expected it reveals the resonantly excited first discrete grating modes to be located at the homogeneous waveguide layer, whereas the fundamental mode cancels to zero in the substrate ($E_y = 0$).

### 5.2.2 Fabrication process

For the realization of our encapsulated grating, first a conventional surface relief grating was fabricated which was then covered by a homogeneous layer of a certain thickness (superstrate). The superstrate can either be realized by applying wafer direct bonding techniques [102–104] or by a controlled material deposition without filling the grating grooves [105]. For our device we used the latter approach. A standard silicon wafer

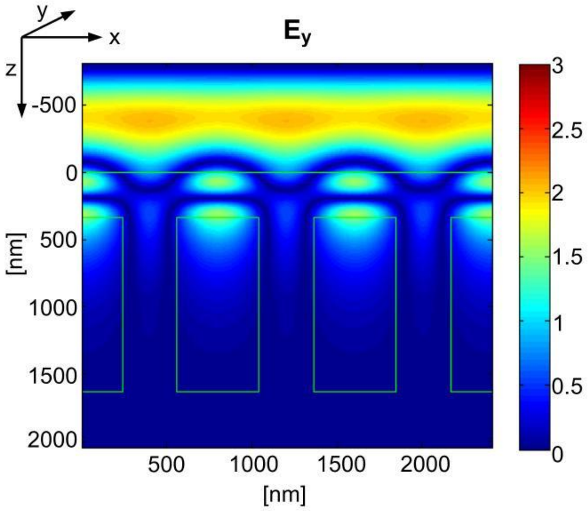

**Fig. 5.3.** Optical near field for the design encapsulated grating structure. Rigorous-Coupled-Wave Analysis (RCWA) optical near field calculation of the y-component of the electric field vector for the design monolithic surface structure. For our simulation, a normally incident plane wave of TE-polarized light with a wavelength of 1550 nm was assumed.

with 100 mm in diameter was first coated with a 80 nm chromium layer, serving as the mask during the silicon etching process. After spin-coating an electron beam sensitive (chemically amplified) resist on top, the 800 nm period grating was defined by means of electron beam lithography for an area of (7.5 x 50) $\mathrm{mm}^2$, aiming at a grating fill factor of 0.4. The developed binary resist profile was then transferred into the chromium layer and subsequently into the silicon bulk substrate by utilizing an anisotropic (i.e. binary) ICP (Inductively-Coupled-Plasma) dry etching process. Here, the etching time was adjusted to match the desired groove depth of about 1300 nm. The surface relief grating was then entirely covered by the use of Plasma-Ion-Assisted Deposition (PIAD) under an oblique and fixed angle of about 70° to minimize groove filling. Since the periodic profile is transferred to the coated surface, a final CMP (Chemical-Mechanical Polishing) step was utilized to planarize the surface and, moreover, to adjust the homogeneous waveguide layer thickness $s$.

Figure 5.4(a) depicts a cross-sectional view scanning electron microscope (SEM) image of the fabricated and characterized grating profile. Due to the coating process, it strongly deviates from the rectangular design structure. However, the high tolerances of our design

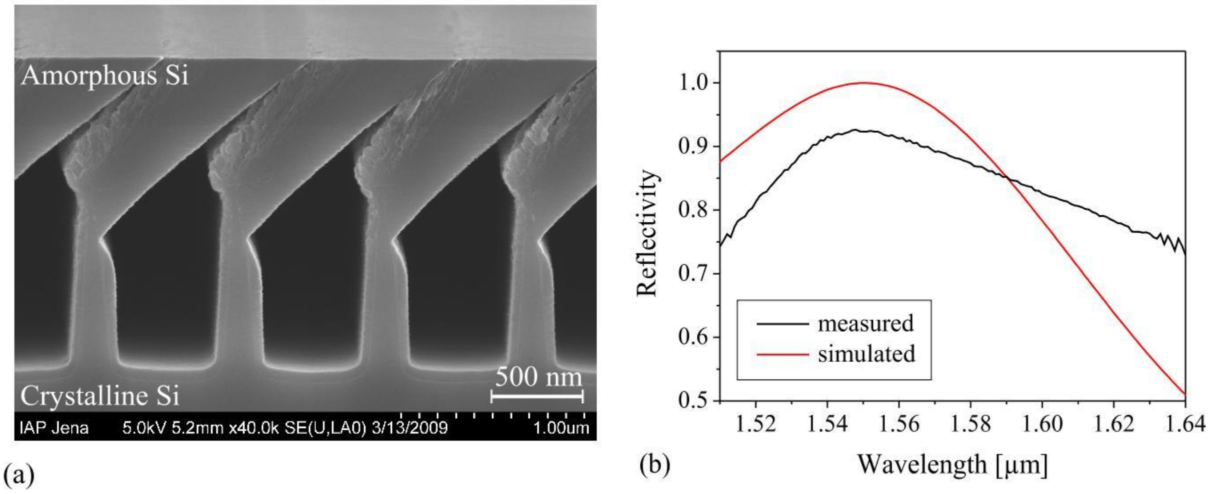

**Fig. 5.4.** (a) SEM (scanning electron microscope) cross-sectional view of the fabricated 800 nm period encapsulated grating in silicon that forms a quasi-monolithic surface mirror, efficiently reflecting normally incident light with a wavelength of 1.55 $\mu$m. (b) Measured spectral reflectance (black curve) of the fabricated grating for normal incidence $(0 \pm 1)^\circ$ (red curve represents simulation from Fig. 5.2(b)).

parameters $f$ and $g$ may still ensure a high reflectivity as demonstrated in the next section. We note that the fabrication technique used here only provides a *quasi-monolithic* grating since the cover layer has an amorphous structure, see Fig. 5.4(a). However, in contrast to conventional waveguide gratings our device consists of only one material which suggests a significantly reduced mechanical loss [24].

### 5.2.3 Experimental characterization

The spectral reflectivity under normal incidence $(0 \pm 1)^\circ$ was measured using a fiber coupled tunable diode laser with a spectral range of $1.51\,\mu\text{m} < \lambda < 1.64\,\mu\text{m}$, incorporated into the measurement setup from Fig. 3.9. After the polarized and collimated beam was reflected by the grating, it was deflected onto a photo detector by a beam splitter. As a reference for the measured intensity we used a multilayer dielectric mirror rated at $R = 1$ for the available spectral range. The measured data is shown in Fig. 5.4(b) (black curve) and reveals a reflectivity of higher than 80 % for a broad spectral range from 1.52 $\mu$m to 1.61 $\mu$m. The difference between the measured and the simulated data (red curve) is not surprising since the actual fabricated profile also shows substantial differences from the designed profile. Nevertheless, the measured peak reflectivity is located closely to the design wavelength of 1.55 $\mu$m with a value of about 93 % where a measurement error of ± 0.5 % needs to be taken into account. The discrepancy between simulated and measured peak reflectivity of about 7 % is, most likely, mainly attributed to a deviation of the top waveguide layer thickness from its optimum value $s = 337$ nm. From the SEM image in Fig. 5.4(a), a thickness of 300 nm was estimated. Variations in all the design parameter values might also contribute here. We expect that a major part of the missing 7 % is transmitted through the device. However, this could not be verified since the rear side of the wafer was unpolished. The parameter variations result from inhomogeneities within the various steps of fabrication and need to be further improved by means of technology evaluation.

### 5.2.4 Summary and discussion

Our rigorous modeling has shown that a monolithic flat surface mirror with perfect reflectivity is theoretically possible. Such a reflector comprises an encapsulated subwavelength grating with a flat polished surface and, thus, overcomes the limitations of the T-shaped structure in terms of mechanical stability and device handling. Based on the current understanding of the underlying mechanism of coating thermal noise, such a device should be able to increase the sensitivity in ongoing and future high-precision laser interferometric measurements. We were able to fabricate a first demonstrator of our reflector that consists of a nanostructured crystalline silicon wafer of 100 mm in diameter covered by an amorphous and polished silicon top layer. Our demonstrator showed a high reflectivity of 93 % at the design wavelength of 1550 nm and represents the first experimental demonstration of a robust, large-area high-reflectivity quasi-monolithic surface. We expect that improvements towards a perfect reflectivity are possible with improved electron beam lithography and other fabrication steps involved. Moreover, we propose to use a wafer direct bonding technique to contact a crystalline top layer (superstrate) onto a crystalline nanostructured substrate, thereby realizing a truly monolithic flat surface reflector.

## 5.3 Encapsulated grating in fused silica

As outlined at the beginning of this chapter, an encapsulated grating reflector inherently provides just a weak perturbation of the waveguide layer which gives a small diffraction efficiency into the waveguide modes and thus a narrow resonance spectral bandwidth according to Eqs. (2.30) and (2.32). This effect will even be amplified when using fused silica as the bulk material due to a very low refractive index contrast to air ($\Delta n \approx 0.5$). Hence, such a fused silica encapsulated grating would not be suitable for mirror applications as mainly described by this work, but represents a new type of a monolithic narrowband notch filter whose spectral reflectivity linewidth can be expected to be in a range of only a few nanometers. Since fused silica is widely transparent from UV to NIR, the working wavelength can be freely defined in this range by choosing appropriate grating parameters such as the period $d$ or the waveguide layer thickness $s$. Consequently, a linear spatial variation of one of these parameters over a given grating length should offer a tunabilty of the resonance peak over a wide spectral range by simply translating the laser beam relative to the grating [106]. In the following we will theoretically investigate such a new type of a narrowband tunable bandstop filter working in a wide NIR band ($800\,\mathrm{nm} < \lambda < 1600\,\mathrm{nm}$) by means of rigorous simulation, and present possible routes for a fabrication process.

### 5.3.1 Design considerations for a narrowband tunable NIR bandstop filter

For our design considerations, we assume the grating period to be the spatially varying parameter while the waveguide layer thickness stays constant. Such a configuration seems more suitable for state-of-the-art fabrication techniques since a variation of the grating period can be accurately controlled during electron beam lithography (see next section for more detail). Whereas the cover layer thickness will be nearly constant after applying a wafer direct bonding or a material deposition/CMP approach, respectively. Figure 5.5 shows on the left hand side the basic idea of our proposed monolithic narrowband tunable filter where the resonance peak position is controlled by the grating period ranging from

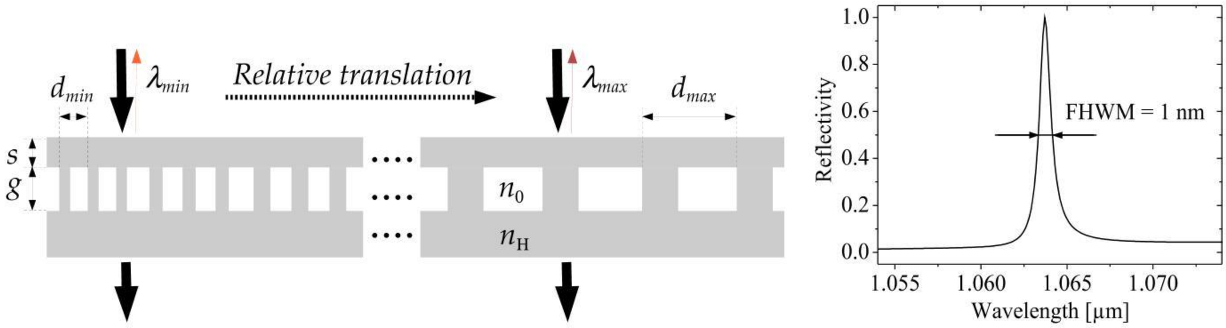

**Fig. 5.5.** Encapsulated grating with varying period as a monolithic narrowband tunable bandstop filter. By translating the laser beam relative to the grating device the resonance wavelength is shifted. For a fused silica encapsulated grating with period $d = 797$ nm, cover layer thickness $s = 700$ nm, groove depth $g = 1500$ nm and fill factor $f = 0.4$ (assuming TM-polarized light under normal incidence), the resonance peak is located at $\lambda = 1064$ nm with a full width at half maximum (FWHM) of only 1 nm.

$d_{\text{min}}$ to $d_{\text{max}}$. The tuning of the narrowband reflected wavelength peak between $\lambda_{\text{min}}$ and $\lambda_{\text{max}}$ can thus be realized by translating the laser beam relative to the grating or vice versa. For a fused silica encapsulated grating with fixed parameters such as a period of $d = 797$ nm, a cover layer thickness of $s = 700$ nm, a groove depth of $g = 1500$ nm, and a fill factor of $f = 0.4$ (assuming TM-polarized light under normal incidence), the right hand side of Fig. 5.5 shows its resonance peak which is in this case located at $\lambda_{\text{res}} = 1064$ nm with a full width at half maximum (FWHM) of only 1 nm. Such a small linewidth is ideal for filter applications [35,85]. Moreover, the contrast between resonance and off-resonance reflectivity exceeds a value of 20 which should be sufficient for most experiments.

Aiming at a tunable wavelength range in the NIR region with $\lambda_{\text{min}} \approx 800\,\text{nm} < \lambda < \lambda_{\text{max}} \approx 1600\,\text{nm}$, including prominent laser emission spectra around 800 nm (Ti:Sapphire), 1030 nm (Yb:YAG), 1064 nm (Nd:YAG), and 1550 nm (InGaAsP), Ineqs. (2.15)-(2.17) determine a grating period variation ranging from $d_{\text{min}} = 570$ nm to $d_{\text{max}} = 1300$ nm to allow for resonant reflection in principle. By means of rigorous simulation [79] the reflectivity from a fused silica encapsulated grating was calculated for a simultaneous variation of the wavelength and the grating period ranging from 780 nm to 1600 nm and 570 nm to 1400 nm, respectively, and is plotted in Fig. 5.6. For this calculation, a constant cover layer thickness of $s = 700$ nm, a groove depth of $g = 1500$ nm, a fill factor of $f =$

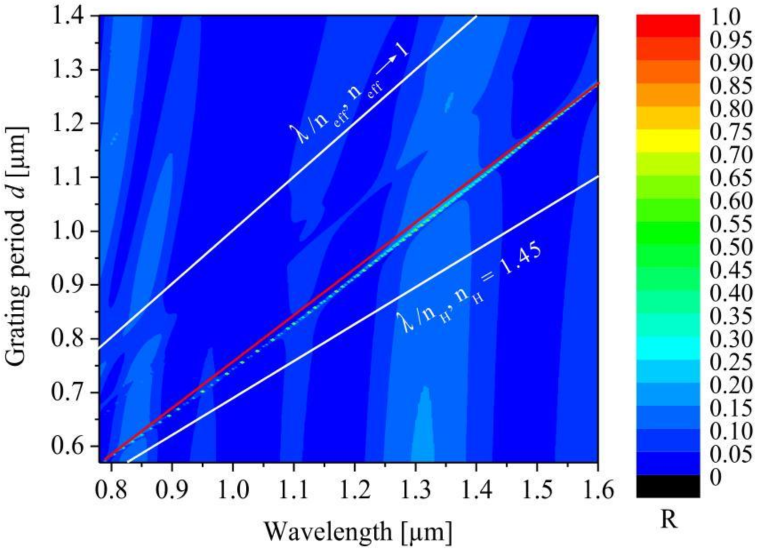

**Fig. 5.6.** Reflectivity plotted against the wavelength $\lambda$ and the period $d$ for a fused silica encapsulated grating with cover layer thickness $s = 700\,\text{nm}$, groove depth $g = 1500\,\text{nm}$ and fill factor $f = 0.4$, assuming TM-polarized light under normal incidence. The single resonance peak moves linearly through the entire NIR wavelength region by varying the period from $d_{\text{min}} = 570\,\text{nm}$ to $d_{\text{max}} = 1300\,\text{nm}$. The resonance line is interrupted due to the discretization of the parameter grid.

0.4, and TM-polarized light impinging under normal incidence had been assumed. As desired a single resonance peak moves almost linearly through the entire NIR wavelength region upon the grating period variation as chosen above. The found wavelength shift of the resonance peak $\Delta\lambda$ [nm] is almost equal to the change in period $\Delta d$ [nm]. Thus, the dependency of the resonance wavelength $\lambda_{\text{res}}$ on the grating period $d$ can be well approximated by the linear function (red line):

$$\lambda_{\text{res}}\,[\text{nm}] = 1.15 \cdot d\,[\text{nm}] + 135\,\text{nm}. \tag{5.2}$$

The white lines indicate the boundaries of the parameter region where resonant reflection is possible for a given wavelength, according to Ineqs. (2.15)-(2.17) and assuming an effective index approaching $n_{\text{eff}} \rightarrow 1$. Please note that the resonance line in Fig. 5.6 appears interrupted only due to the discretization of the parameter grid. In order to show its continuity in peak reflectivity and linewidth over the entire tuning interval, Figs. 5.7(a)-(c) plot the resonance peaks for a slight variation around three very prominent

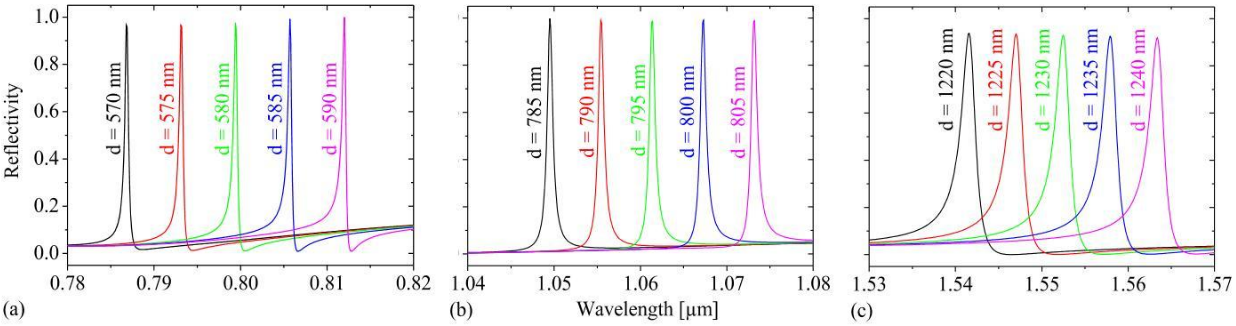

**Fig. 5.7.** Tuning of the spectral reflectivity resonance peak around frequently used NIR wavelengths of (a) 800 nm, (b) 1060 nm, and (c) 1550 nm by varying the grating period in an appropriate range.

laser wavelengths: (a) 800 nm, (b) 1060 nm, and (c) 1550 nm. Even though the resonance linewidths as well as the ratios between resonance and off-resonance reflectivity are not perfectly constant throughout the entire tuning interval, the filter performance for such a wide spectral range of $d_{\max} - d_{\min} = 800\,\text{nm}$ is impressive and has not been reported before. An expansion of the tuning interval to even shorter or larger wavelengths without affecting the filter performance is not possible. This is because for shorter wavelengths a second waveguide mode arises in the waveguide layer leading to a second resonance peak, while for larger wavelengths the mode matching becomes worse resulting in a decrease of the peak reflectivity. This behavior is attributed to the choice of the thickness $s$ of the waveguide layer which is able to support the propagation of a single waveguide mode only for a limited wavelength range. Our waveguide layer thickness of $s = 700\,\text{nm}$ was hence not chosen arbitrarily but rather for an optimum performance in the particular NIR region targeted.

## 5.3.2 Prospects for the fabrication process

For fabrication of our fused silica tunable filter, we can in principle employ the same approach as realized for the encapsulated grating fabricated from silicon in paragraph 5.2. After etching a conventional surface relief grating into a fused silica substrate, a thin and flat surface cover layer can be subsequently obtained either by applying wafer direct bonding techniques or by a controlled material deposition without filling the grating grooves followed by a final CMP step. All fabrication techniques potentially involved such as wafer direct bonding or CMP are also suitable for fused silica processing [107,108]. As stated above, a superstrate realized by a wafer direct bond should be preferred since it would provide a rectangular grating profile (as assumed during the rigorous simulations) as well as a widely homogeneous cover layer thickness $s$.

The desired grating period variation that enables the tuning of the resonance peak is realized by state-of-the-art electron beam lithography which is part of the surface relief grating fabrication. In contrast to holographic or photo-lithography, during each electron beam exposure step the lateral grating parameters such as the period or the fill factor can be freely controlled with a resolution down to 50 nm. The electron beam facility used at the Institute of Applied Physics (IAP), University of Jena, is a Vistec SB350 OS that allows to adjust the grating period with an increment of 1 nm. In our case, this corresponds to a fundamental minimum shift of the resonance peak of about 1 nm as well, according to Eq. (5.2). For the entire wavelength range from 800 nm to 1600 nm, a period variation between 580 nm and 1275 nm is necessary (see Fig. 5.6), which for a desired minimum shift of 1 nm would cause 695 variation steps of the grating period during electron beam exposure. The overall required grating length will finally be defined by the laser beam radius since the beam must hit a grating spot having only one particular period to gain the theoretically predicted narrow linewidth. For instance, a laser beam diameter of 1 mm and an amount of 695 variation steps (providing a minimum wavelength shift increment of 1 nm) result in a minimum overall grating length of 69.5 cm. Of course, such a wide grating must be split into sub-gratings in order to be patterned onto a single standard fused silica substrate. In summary, both the available laser beam size and the desired increment of the resonance wavelength shift determine the necessary grating dimensions in practice.

# 6 Conclusions and outlook

Thermally driven motion of mirror surfaces provides a contribution to thermal noise in high-precision metrology and is a limiting factor for the sensitivity of laser based gravitational wave detectors. For dielectrically coated test mass mirrors, the thermal noise is mainly caused by the mechanical loss of the several $\mu$m thick multilayer coating stack and the related Q-factor reduction of the test mass substrate. Typical high-reflectivity coatings consist of up to 40 alternating layers of $SiO_2$ and $Ta_2O_5$ where the major loss contribution stems from the latter. In order to reduce coating thermal noise new concepts are required that simultaneously provide high optical quality and low mechanical loss.

This work proposed to apply thin surface relief guided-mode resonant waveguide structures instead of conventionally coated mirrors. With these structures the thermal noise introduced by the coating is expected to be significantly reduced due to the fact that the surface of the (high mechanical quality) substrate only carries isolated grating ridges of less than a $\mu$m height. Reflectivities of exactly 100% are possible for these grating devices if a certain grating profile is precisely met.

As a first experimental proof of this idea, we fabricated a resonant waveguide grating based high-reflection mirror. The mirror substrate in this case was silica and carried a single layer grating of $Ta_2O_5$ (Tantala) with a thickness of 400 nm. We characterized this device as a cavity coupler of a high-finesse standing-wave cavity. From the cavity finesse we were able to deduce a waveguide grating power reflectivity of $(99.08 \pm 0.05)\,\%$ at the laser wavelength of 1064 nm. At that time this was, to the best of our knowledge, the highest value of resonant reflection that has ever been reported for 1064 nm laser light. Moreover, a standing-wave cavity setup had never been utilized to accurately determine a grating based resonant reflectivity before.

Besides fused silica as a high mechanical quality test mass material, within the past few years silicon was found to be a very promising candidate, and was proposed for use in the field of high-precision measurements together with 1550 nm laser light. Following this suggestion, we also transferred the idea of this work to this combination of substrate material and laser wavelength, and realized different silicon supported RWG layouts. The spectral reflectance under normal incidence $(0 \pm 1)^\circ$ for a fabricated sample revealed a value of higher than 98 % for a broad spectral range from $1.52\,\mu$m to $1.59\,\mu$m. The peak reflectance was located closely to the wavelength of $1.55\,\mu$m with a value of about 98.9 %.

Although all approaches mentioned so far reduce the thick dielectric multilayer stack of conventional mirrors to a thin waveguide layer, at least one additional material has to be added to the substrate which may still result in an increased mechanical loss. Thus, a truly coating free (i.e. monolithic) mirror concept is of enormous interest. For this purpose, this work theoretically proposed as well as experimentally demonstrated for the first time a monolithic high-reflectivity surface mirror, i.e. a single piece of mono-crystalline silicon, that is also based on guided-mode resonances and reaches 100% reflectivity in principle. Since no material is added to the silicon substrate, the currently limiting coating Brownian thermal noise is avoided. Furthermore, our approach uses a broadband guided optical mode and therefore does not increase the interaction length of light with matter thus keeping thermo-refractive noise as well as absorption low. The monolithic implementation was done by replacing the remaining $SiO_2$ low-index layer of the abovementioned RWG layouts by an *effective* silicon low-index layer. Such a T-shaped grating was successfully fabricated and incorporated into a standing-wave cavity as the end mirror together with a conventional coupling mirror. The finesse of this cavity was found to be $F = 2784 \pm 100$ which corresponds to a grating reflectivity of $(99.7945 \pm 0.0086)\,\%$. The measured optical reflectivity is, to the best of our knowledge, the highest resonant reflection ever realized and in principle allows for a coating free linear cavity with a finesse of $\approx 1500$ which already reaches the regime of finesse values used in gravitational wave detectors. These results are considered to be the major achievement of this thesis.

In addition to the monolithic high-reflectivity waveguide mirrors on the basis of T-shaped grating profiles, alternatives with less demands in the fabrication process and in the device handling have been investigated. We proposed and demonstrated a quasi-monolithic mirror architecture that is formed by an encapsulated subwavelength grating. Such a device also creates a resonant waveguide structure but with a flat and robust surface. We presented a design and a first demonstrator fabricated from silicon. Our measurement results revealed a promising high reflectivity of 93 % for normal incidence at the design wavelength of $\lambda = 1550\,\mathrm{nm}$.

Having demonstrated the first monolithic surface mirrors ever, future work should aim for the realization of even higher reflectivities. Although we achieved record values of resonant reflection of up to 99.8%, this value cannot compete yet with reflectivities from conventional multilayer coatings required for applications in reference cavities and optical clocks [12, 13]. A perfect reflectivity for a certain wavelength is possible if the grating parameters meet certain values and the grating profile conforms to the one assumed during simulation. As already outlined in paragraph 4.2.4, we expect to obtain a higher reflectivity for the already fabricated monolithic T-shaped grating for a wavelength or an incidence angle slightly deviating from the design parameters. Furthermore, we plan to optimize the fabrication processes to enable a precise matching of designed and fabricated grating profile. We expect that considerable improvements towards a perfect reflectivity are possible with improved electron beam lithography and etching technologies. Moreover, the grating designs will be further optimized to provide larger and thus more convenient parameter tolerances for the fabrication process.

In order to provide stable Fabry-Perot setups, at least one of the cavity mirrors needs to exhibit a surface with a certain radius of curvature. As confirmed by first experimental trials done in collaboration with the Fraunhofer Institute of Applied Optics and Precision Engineering (IOF) in Jena, the used fabrication techniques can also be adapted to substrates with large radii of curvature as required for long arm cavities. The first demonstration of an all-grating based and thus coating free cavity is scheduled for the near future. Very recently, it has been theoretically as well as experimentally shown that by only spatially varying the grating period and/or the fill factor of a high-contrast subwavelength reflector the output phase of the reflected beam can be manipulated such that it is focused similarly as if by a regular lens [109, 110]. However, the maintenance of very high reflectivities upon grating parameter variations is very challenging due to the limited tolerances.

As many future high-precision experiments will be operated at very low temperatures it is necessary to precisely characterize the reflectivities of our waveguide mirrors at cryogenic temperatures. In this regard, the temperature dependency of the index of refraction needs be considered during the grating design process. It is interesting to note that from first estimates we expect that due to this temperature dependent index of refraction the reflectivity of the already fabricated monolithic T-shaped grating can be increased towards its theoretical limit when working at a temperature of about 100°C.

The current understanding of coating noise mechanisms suggests that the monolithic, single crystalline waveguide mirror should not show any Brownian coating thermal noise which is the dominant coating thermal noise in conventional mirrors. In such a monolithic mirror the only Brownian thermal noise in the detection band of gravitational wave detectors stems from the substrate and is expected to be rather low if the substrate's quality factor (Q-factor) is high. This consideration is supported by a previous experiment proving that a substrate Q-factor of $10^8$ was not reduced by nanostructuring the substrate's surface [24]. However, an in-situ experimental confirmation that the thermal noise of our mirror concepts is for fundamental reasons much lower than any other high-reflectivity mirror concept has not been adduced yet. In collaboration with the University of Hanover, it is planned to perform an experiment to directly verify the coating thermal noise reduction in monolithic and single layer waveguide mirrors. From this we like to proof the advantage of waveguide gratings compared to multilayer coatings in terms of their individual thermal noise contributions. This experiment should even provide the possibility to distinguish between different thermal noise mechanisms of waveguide gratings, and allows to investigate these devices at very high displacement sensitivities. Previous experiments [23, 111] showed that the Brownian coating thermal noise level of conventional mirrors is below $10^{-17}\,\mathrm{m}/\sqrt{\mathrm{Hz}}$ at $1\,\mathrm{kHz}$. In order to achieve such interferometer sensitivities multiple noise sources need to be suppressed. In particular, laser frequency noise and seismic noise are a problem and have to be reduced using a long reference cavity with low bandwidth and suspended optics under vacuum conditions. The basic idea is to set up a cavity that can incorporate either a waveguide grating or a conventional mirror as the coupling mirror. In order to achieve a displacement sensitivity that is dominated by coating thermal noise, optical as well as mechanical parameters have to be optimized.

For instance, the beam size on the waveguide grating should be as small as possible to enhance the effect of coating thermal noise. Furthermore, it was recently shown that substrate dimensions affect the coating thermal noise level [112] and can be designed to maximize coating thermal noise with respect to substrate thermal noise.

In light of the encouraging results of this thesis and foreseen progress in the near future, the author of this work anticipates that its achievements will open the avenue to new generations of a variety of high-precision experiments targeting fundamental questions of physics.

# Bibliography

[1] P. F. Cohadon, A. Heidmann, and M. Pinard. Cooling of a mirror by radiation pressure. *Phys. Rev. Lett.*, **83**(16):3174–3177, 1999.

[2] T. Corbitt, Y. Chen, E. Innerhofer, H. Müller-Ebhardt, D. Ottaway, H. Rehbein, D. Sigg, S. Whitcomb, C. Wipf, and N. Mavalvala. An all-optical trap for a gram-scale mirror. *Phys. Rev. Lett.*, **98**(15):150802, 2007.

[3] S. Mancini, V. Giovannetti, D. Vitali, and P. Tombesi. Entangling macroscopic oscillators exploiting radiation pressure. *Phys. Rev. Lett.*, **88**(12):120401, 2002.

[4] H. Müller-Ebhardt, H. Rehbein, R. Schnabel, K. Danzmann, and Y. Chen. Entanglement of macroscopic test masses and the standard quantum limit in laser interferometry. *Phys. Rev. Lett.*, **100**(1):013601, 2008.

[5] H. J. Kimble, Y. Levin, A. B. Matsko, K. S. Thorne, and S. P. Vyatchanin. Conversion of conventional gravitational-wave interferometers into quantum nondemolition interferometers by modifying their input and/or output optics. *Phys. Rev. D*, **65**(2):022002, 2001.

[6] P. Aufmuth and K. Danzmann. Gravitational wave detectors. *New J. Phys.*, **7**:202, 2005.

[7] J. R. Smith and for the LIGO Scientific Collaboration. The path to the enhanced and advanced ligo gravitational-wave detectors. *Class. Quantum Grav.*, **26**(11):114013, 2009.

[8] D. Kleckner and D. Bouwmeester. Sub-kelvin optical cooling of a micromechanical resonator. *Nature (London)*, **444**:75–78, 2006.

[9] A. Schliesser, O. Arcizet, R. Rivière, G. Anetsberger, and T. J. Kippenberg. Resolved-sideband cooling and position measurement of a micromechanical oscil-

lator close to the heisenberg uncertainty limit. *Nature Phys.*, **5**:509–514, 2009.

[10] F. Marquardt, J. P. Chen, A. A. Clerk, and S. M. Girvin. Quantum theory of cavity-assisted sideband cooling of mechanical motion. *Phys. Rev. Lett.*, **99**(9):093902, 2007.

[11] Th. Udem, R. Holzwarth, and T. W. Hänsch. Optical frequency metrology. *Nature (London)*, **416**:233–237, 2002.

[12] B. C. Young, F. C. Cruz, W. M. Itano, and J. C. Bergquist. Visible lasers with subhertz linewidths. *Phys. Rev. Lett.*, **82**(19):3799–3802, 1999.

[13] C. Braxmaier, O. Pradl, H. Müller, A. Peters, J. Mlynek, V. Loriette, and S. Schiller. Proposed test of the time independence of the fundamental constants $\alpha$ and $m_e/m_p$ using monolithic resonators. *Phys. Rev. D*, **64**(4):042001, 2001.

[14] K. Numata, A. Kemery, and J. Camp. Thermal-noise limit in the frequency stabilization of lasers with rigid cavities. *Phys. Rev. Lett.*, **93**(25):250602, 2004.

[15] Y. Levin. Internal thermal noise in the LIGO test masses: A direct approach. *Phys. Rev. D*, **57**(2):659–663, 1998.

[16] V. B. Braginsky, M. L. Gorodetsky, and S. P. Vyatchanin. Thermodynamical fluctuations and photo-thermal shot noise in gravitational wave antennae. *Phys. Lett. A*, **264**(1):1–10, 1999.

[17] M. L. Gorodetsky. Thermal noises and noise compensation in high-reflection multilayer coating. *Phys. Lett. A*, **372**(46):6813–6822, 2008.

[18] R. Nawrodt, S. Rowan, J. Hough, M. Punturo, F. Ricci, and J.-Y. Vinet. Challenges in thermal noise for 3rd generation of gravitational wave detectors. *Gen. Relativ. Gravit.*, **43**(2):593–622, 2011.

[19] G. Rempe, R. J. Thompson, H. J. Kimble, and R. Lalezari. Measurement of ultralow losses in an optical interferometer. *Opt. Lett.*, **17**(5):363–365, 1992.

[20] F. Seifert, P. Kwee, M. Heurs, B. Willke, and K. Danzmann. Laser power stabilization for second-generation gravitational wave detectors. *Opt. Lett.*, **31**(13):2000–2002, 2006.

[21] G. M. Harry, A. M. Gretarsson, P. R. Saulson, S. E. Kittelberger, S. D. Penn, W. J. Startin, S. Rowan, M. M. Fejer, D. R. M. Crooks, G. Cagnoli, J. Hough, and

N. Nakagawa. Thermal noise in interferometric gravitational wave detectors due to dielectric optical coatings. *Class. Quantum Grav.*, **19**(5):897, 2002.

[22] D. R. M. Crooks, P. Sneddon, G. Cagnoli, J. Hough, S. Rowan, M. M. Fejer, E. Gustafson, R. Route, N. Nakagawa, D. Coyne, G. M. Harry, and A. M. Gretarsson. Excess mechanical loss associated with dielectric mirror coatings on test masses in interferometric gravitational wave detectors. *Class. Quantum Grav.*, **19**(5):883, 2002.

[23] E. D. Black, A. Villar, K. Barbary, A. Bushmaker, J. Heefner, S. Kawamura, F. Kawazoe, L. Matone, S. Meidt, S. R. Rao, K. Schulz, M. Zhang, and K. G. Libbrecht. Direct observation of broadband coating thermal noise in a suspended interferometer. *Phys. Lett. A*, **328**(1):1–5, 2004.

[24] R. Nawrodt, A. Zimmer, T. Koettig, T. Clausnitzer, A. Bunkowski, E.-B. Kley, R. Schnabel, K. Danzmann, S. Nietzsche, W. Vodel, A. Tünnermann, and P. Seidel. Mechanical Q-factor measurements on a test mass with a structured surface. *New J. Phys.*, **9**(7):225, 2007.

[25] J. Agresti, G. Castaldi, R. DeSalvo, V. Galdi, V. Pierro, and I. M. Pinto. Optimized multilayer dielectric mirror coatings for gravitational wave interferometers. *Adv. in Thin-Film Coatings for Opt. Appl. III, Proc. SPIE Int. Soc. Opt. Eng.*, **6286**:628608, 2006.

[26] I. Martin, H. Armandula, C. Comtet, M. M. Fejer, A. Gretarsson, G. Harry, J. Hough, J.-M. M. Mackowski, I. MacLaren, C. Michel, J.-L. Montorio, N. Morgado, R. Nawrodt, S. Penn, S. Reid, A. Remillieux, R. Route, S. Rowan, C. Schwarz, P. Seidel, W. Vodel, and A. Zimmer. Measurements of a low-temperature mechanical dissipation peak in a single layer of $Ta_2O_5$ doped with $TiO_2$. *Class. Quantum Grav.*, **25**(5):055005, 2008.

[27] G. M. Harry, H. Armandula, E. Black, D. R. M. Crooks, G. Cagnoli, J. Hough, P. Murray, S. Reid, S. Rowan, P. Sneddon, M. M. Fejer, R. Route, and S. D. Penn. Thermal noise from optical coatings in gravitational wave detectors. *Appl. Opt.*, **45**(7):1569–1574, 2006.

[28] H. J. Kimble, B. L. Lev, and J. Ye. Optical interferometers with reduced sensitivity

to thermal noise. *Phys. Rev. Lett.*, **101**(26):260602, 2008.

[29] G. Cella and A. Giazotto. Coatingless, tunable finesse interferometer for gravitational wave detection. *Phys. Rev. D*, **74**(4):042001, 2006.

[30] S. Goßler, J. Cumpston, K. McKenzie, C. M. Mow-Lowry, M. B. Gray, and D. E. McClelland. Coating-free mirrors for high precision interferometric experiments. *Phys. Rev. A*, **76**(5):053810, 2007.

[31] V. B. Braginsky and S. P. Vyatchanin. Corner reflectors and quantum-non-demolition measurements in gravitational wave antennae. *Phys. Lett. A*, **324**(5-6):345–360, 2004.

[32] A. B. Matsko, A. A. Savchenkov, N. Yu, and L. Maleki. Whispering-gallery-mode resonators as frequency references. I. Fundamental limitations. *J. Opt. Soc. Am. B*, **24**(6):1324–1335, 2007.

[33] I. S. Grudinin, V. S. Ilchenko, and L. Maleki. Ultrahigh optical Q factors of crystalline resonators in the linear regime. *Phys. Rev. A*, **74**(6):063806, 2006.

[34] G. A. Golubenko, A. S. Svakhin, V. A. Sychugov, and A. V. Tishchenko. Total reflection of light from a corrugated surface of a dielectric waveguide. *Sov. J. Quantum Electron.*, **15**(7):886, 1985.

[35] R. Magnusson and S. S. Wang. New principle for optical filters. *Appl. Phys. Lett.*, **61**(9):1022–1024, 1992.

[36] A. Sharon, D. Rosenblatt, and A. A. Friesem. Resonant grating–waveguide structures for visible and near-infrared radiation. *J. Opt. Soc. Am. A*, **14**(11):2985–2993, 1997.

[37] C. F. R. Mateus, M. C. Y. Huang, Y. Deng, A. R. Neureuther, and C. J. Chang-Hasnain. Ultrabroadband mirror using low-index cladded subwavelength grating. *IEEE Photonics Technol. Lett.*, **16**(2):518–520, 2004.

[38] A. Bunkowski, O. Burmeister, D. Friedrich, K. Danzmann, and R. Schnabel. High reflectivity grating waveguide coatings for 1064 nm. *Class. Quantum Grav.*, **23**(24):7297, 2006.

[39] F. Brückner, D. Friedrich, T. Clausnitzer, O. Burmeister, M. Britzger, E.-B. Kley, K. Danzmann, A. Tünnermann, and R. Schnabel. Demonstration of a cavity coupler

based on a resonant waveguide grating. *Opt. Express*, **17**(1):163–169, 2009.

[40] S. Rowan, R. L. Byer, M. M. Fejer, R. K. Route, G. Cagnoli, D. R. Crooks, J. Hough, P. H. Sneddon, and W. Winkler. Test mass materials for a new generation of gravitational wave detectors. *Gravitational-Wave Detection, Proc. SPIE Int. Soc. Opt. Eng.*, **4856**(1):292–297, 2003.

[41] R. Schnabel, M. Britzger, F. Brückner, O. Burmeister, K. Danzmann, J. Dück, T. Eberle, D. Friedrich, H. Lück, M. Mehmet, R. Nawrodt, S. Steinlechner, and B. Willke. Building blocks for future detectors: Silicon test masses and 1550 nm laser light. *J. Physics: Conf. Ser.*, **228**:012029, 2010.

[42] M. A. Green and M. J. Keevers. Optical properties of intrinsic silicon at 300 K. *Prog. Photovolt. Res. Appl.*, **3**:189–192, 1995.

[43] D. F. McGuigan, C. C. Lam, R. Q. Gram, A. W. Hoffman, D. H. Douglass, and H. W. Gutche. Measurements of the mechanical Q of single-crystal silicon at low temperatures. *J. Low Temp. Phys.*, **30**:621–629, 1978.

[44] F. Brückner, E.-B. Kley, and T. Clausnitzer. Monolithischer dielektrischer Spiegel. *German Patent Application*, DE 10 2007 047 681.9, 2007.

[45] F. Brückner, T. Clausnitzer, O. Burmeister, D. Friedrich, E.-B. Kley, K. Danzmann, A. Tünnermann, and R. Schnabel. Monolithic dielectric surfaces as new low-loss light-matter interfaces. *Opt. Lett.*, **33**(3):264–266, 2008.

[46] F. Brückner, D. Friedrich, T. Clausnitzer, M. Britzger, O. Burmeister, K. Danzmann, E.-B. Kley, A. Tünnermann, and R. Schnabel. Realization of a monolithic high-reflectivity cavity mirror from a single silicon crystal. *Phys. Rev. Lett.*, **104**(16):163903, 2010.

[47] F. Brückner, D. Friedrich, M. Britzger, T. Clausnitzer, O. Burmeister, E.-B. Kley, K. Danzmann, A. Tünnermann, and R. Schnabel. Encapsulated subwavelength grating as a quasi-monolithic resonant reflector. *Opt. Express*, **17**(26):24334–24341, 2009.

[48] F. Brückner, S. Kroker, D. Friedrich, E.-B. Kley, and A. Tünnermann. Widely tunable monolithic narrowband grating filter for near-infrared radiation. *Opt. Lett.*, **33**(4):436–438, 2011.

[49] D. Shoemaker and for the LIGO Scientific Collaboration. Advanced LIGO reference design. *Internal working note of the LIGO Lab. LIGO-M060056-v1*, https://dcc.ligo.org/cgi-bin/DocDB/ShowDocument?docid=1507, 2009.

[50] G. Losurdo and for the Advanced Virgo Team. Advanced Virgo preliminary design. *Internal working note of the Virgo Coll. VIR089A08*, http://wwwcascina.virgo.infn.it/advirgo/docs.html, 2008.

[51] LCGT noise budget. *LCGT project home page, http://gw.icrr.u-tokyo.ac.jp/lcgt.*

[52] A. Nishizawa, S. Kawamura, and Sakagami M. Quantum noise in differential-type gravitational-wave interferometer and signal recycling. *J. Phys.: Conf. Ser.*, **122**(1):012019, 2008.

[53] S. A. Hughes and K. S. Thorne. Seismic gravity-gradient noise in interferometric gravitational-wave detectors. *Phys. Rev. D*, **58**(12):122002, 1998.

[54] M. M. Fejer, S. Rowan, G. Cagnoli, D. R. M. Crooks, A. Gretarsson, G. M. Harry, J. Hough, S. D. Penn, P. H. Sneddon, and S. P. Vyatchanin. Thermoelastic dissipation in inhomogeneous media: loss measurements and displacement noise in coated test masses for interferometric gravitational wave detectors. *Phys. Rev. D*, **70**(8):082003, 2004.

[55] V. B. Braginsky, M. L. Gorodetsky, and S. P. Vyatchanin. Thermo-refractive noise in gravitational wave antennae. *Phys. Lett. A*, **271**(5-6):303–307, 2000.

[56] M. Evans, S. Ballmer, M. Fejer, P. Fritschel, G. Harry, and G. Ogin. Thermo-optic noise in coated mirrors for high-precision optical measurements. *Phys. Rev. D*, **78**(10):102003, 2008.

[57] H. B. Callen and T. A. Welton. Irreversibility and generalized noise. *Phys. Rev.*, **83**(1):34–40, 1951.

[58] I. W. Martin, E. Chalkley, R. Nawrodt, H. Armandula, R. Bassiri, C. Comtet, M. M. Fejer, A. Gretarsson, G. Harry, D. Heinert, J. Hough, I. MacLaren, C. Michel, J.-L. Montorio, N. Morgado, S. Penn, S. Reid, R. Route, S. Rowan, C. Schwarz, P. Seidel, W. Vodel, and A. L. Woodcraft. Comparison of the temperature dependence of the mechanical dissipation in thin films of $Ta_2O_5$ and $Ta_2O_5$ doped with $TiO_2$. *Class. Quantum Grav.*, **26**(15):155012, 2009.

[59] S. Chelkowski, S. Hild, and A. Freise. Prospects of higher-order Laguerre-Gauss modes in future gravitational wave detectors. *Phys. Rev. D*, **79**(12):122002, 2009.

[60] F. Y. Khalili. Reducing the mirrors coating noise in laser gravitational-wave antennae by means of double mirrors. *Phys. Lett. A*, **334**(1):67–72, 2005.

[61] D. Rosenblatt, A. Sharon, and A. A. Friesem. Resonant grating waveguide structures. *IEEE J. Quantum Electron.*, **33**:2038–2059, 1997.

[62] E. G. Loewen and E. Popov. *Optical Engineering. Ed. 58: Diffraction Gratings and Applications*. New York : Marcel Dekker, 1997. ISBN 0-8247-9923-2.

[63] M. Neviere, D. Maystre, and P. Vincent. Determination of the leaky modes of a corrugated waveguide: Application to the study of anomalies of dielectric coated gratings. *J. Opt.*, **8**:231–242, 1977.

[64] R. G. Hunsperger. *Integrated Optics : Theory and Technology*. Springer-Verlag (Advanced Texts in Physics), 5. edition, 2002. ISBN 3-540-43341-4.

[65] F. Goos and H. Hänchen. Ein neuer und fundamentaler Versuch zur Totalreflexion. *Annalen der Physik*, **436**:333–346, 1947.

[66] F. Goos and H. Lindberg-Hänchen. Neumessung des Strahlversetzungseffektes bei Totalreflexion. *Annalen der Physik*, **440**:251–252, 1949.

[67] M. Born and E. Wolf. *Principles of Optics : Electromagnetic Theory of Propagation, Interference and Diffraction of Light*. Cambridge University Press, 7. edition, 1999. ISBN 0-521-64222-1.

[68] A. Sommerfeld. *Vorlesungen über theoretische Physik. Bd. 4: Optik*. Leipzig: Akademische Verlagsgesellschaft Geest & Portig, 1964.

[69] S. M. Norton, T. Erdogan, and M. G. Morris. Coupled-mode theory of resonant-grating filters. *J. Opt. Soc. Am. A*, **14**:629–639, 1997.

[70] C. Fabry and A. Pérot. Théorie et applications d´une nouvelle méthode de spectroscopie interférentielle. *Annales de Chimie et de Physique*, **16**:115–144, 1899.

[71] I. C. Botten, M. S. Craig, R. C. McPhedran, J. L. Adams, and J. R. Andrewartha. The dielectric lamellar diffraction grating. *J. Mod. Opt.*, **28**:413–428, 1981.

[72] A. V. Tishchenko. Phenomenological representation of deep and high contrast lamel-

lar gratings by means of the modal method. *Opt. Quantum Electron.*, **37**:309–330, 2005.

[73] P. Lalanne, J. P. Hugonin, and P. Chavel. Optical properties of deep lamellar gratings: A coupled bloch-mode insight. *J. Lightwave Technol.*, **24**(6):2442, 2006.

[74] T. Clausnitzer. *Kontrolle der Beugungseffizienzen dielektrischer Gitter*. PhD thesis, Friedrich-Schiller-University Jena, Germany, 2007.

[75] T. Clausnitzer, T. Kämpfe, E.-B. Kley, A. Tünnermann, U. Peschel, A. V. Tishchenko, and O. Parriaux. An intelligible explanation of highly-efficient diffraction in deep dielectric rectangular transmission gratings. *Opt. Express*, **13**(26):10448–10456, 2005.

[76] A. Yariv. Coupled mode theory for guided-wave optics. *IEEE J. Quantum Electron.*, **9**:919–933, 1973.

[77] V. Karagodsky, F. G. Sedgwick, and C. J. Chang-Hasnain. Theoretical analysis of subwavelength high contrast grating reflectors. *Opt. Express*, **18**(16):16973–16988, 2010.

[78] L. Li. New formulation of the fourier modal method for crossed surface-relief gratings. *J. Opt. Soc. Am. A*, **14**(10):2758–2767, 1997.

[79] M. G. Moharam and T. K. Gaylord. Rigorous coupled-wave analysis of planar-grating diffraction. *J. Opt. Soc. Am.*, **71**(7):811–818, 1981.

[80] A. Taflove and S. C. Hagness. *The Finite-Difference Time-Domain Method.* rtech House, Norwood, 2000.

[81] A. V. Tishchenko. Generalized source method: New possibilities for waveguide and grating problems. *Opt. Quantum Electron.*, **32**:971–980, 2000.

[82] http://www.unigit.com/.

[83] http://www.gsolver.com/.

[84] C. F. R. Mateus, M. C. Y. Huang, L. Chen, C. J. Chang-Hasnain, and Y. Suzuki. Broad-band mirror (1.12-1.62 $\mu$m) using a subwavelength grating. *IEEE Photonics Technol. Lett.*, **16**(7):1676–1678, 2004.

[85] T. Clausnitzer, A. V. Tishchenko, E.-B. Kley, H.-J. Fuchs, D. Schelle, O. Parriaux,

and U. Kroll. Narrowband, polarization-independent free-space wave notch filter. *J. Opt. Soc. Am. A*, **22**(12):2799–2803, 2005.

[86] E. Popov, M. Nevière, B. Gralak, and G. Tayeb. Staircase approximation validity for arbitrary-shaped gratings. *J. Opt. Soc. Am. A*, **19**(1):33–42, 2002.

[87] R. W. P. Drever, J. L. Hall, F. V. Kowalski, J. Hough, G. M. Ford, A. J. Munley, and H. Ward. Laser phase and frequency stabilization using an optical resonator. *Appl. Phys. B*, **31**:97–105, 1983.

[88] B. A. Usievich, V. A. Sychugov, J. K. H. Nurligareev, and O. Parriaux. Multilayer resonances sharpened by grating waveguide resonance. *Opt. Quantum Electron.*, **36**:109–117, 2004.

[89] P. Lalanne and D. Lemercier-Lalanne. On the effective medium theory of subwavelength periodic structures. *J. Mod. Opt.*, **43**:2063–2085, 1996.

[90] M. C. Y. Huang, Y. Zhou, and C. J. Chang-Hasnain. A surface-emitting laser incorporating a high-index-contrast subwavelength grating. *Nature Phot.*, **1**(2):119–122, 2007.

[91] J. S. Ye, Y. Kanamori, F.-R. Hu, and K. Hane. Self-supported subwavelength gratings with a broad band of high reflectance analysed by the rigorous coupled-wave method. *J. Mod. Opt.*, **53**:1995–2004, 2006.

[92] E. Bisaillon, D. Tan, B. Faraji, A. Kirk, L. Chrowstowski, and D. V. Plant. High reflectivity air-bridge subwavelength grating reflector and fabry-perot cavity in AlGaAs/GaAs. *Opt. Express*, **14**(7):2573–2582, 2006.

[93] H. J. Simon, C. Huang, J. C. Quail, and Z. Chen. Second-harmonic generation with surface plasmons from a silvered quartz grating. *Phys. Rev. B*, **38**:7408–7414, 1988.

[94] B. K. Canfield, H. Husu, J. Laukkanen, B. Bai, M. Kuittinen, J. Turunen, and M. Kauranen. Local field asymmetry drives second-harmonic generation in noncentrosymmetric nanodimers. *Nano Lett.*, **7**:1251–1255, 2007.

[95] M. Siltanen, S. Leivo, P. Voima, M. Kauranen, P. Karvinen, P. Vahimaa, and M. Kuittinen. Strong enhancement of second-harmonic generation in all-dielectric resonant waveguide grating. *Appl. Phys. Lett.*, **91**:111109, 2007.

[96] A. Saari, G. Genty, M. Siltanen, P. Karvinen, P. Vahimaa, M. Kuittinen, and

M. Kauranen. Giant enhancement of second-harmonic generation in multiple diffraction orders from sub-wavelength resonant waveguide grating. *Opt. Express*, **18**:12298–12303, 2010.

[97] M. Kawabe, S. Hirata, and S. Namba. Ridge waveguides and electro-optical switches in $LiNbO_3$ fabricated by ion-bombardment-enhanced etching. *IEEE Trans. Circuits Syst.*, **26**:1109–1113, 1979.

[98] F. Schrempel, T. Gischkat, H. Hartung, E.-B. Kley, and W. Wesch. Ion beam enhanced etching of $LiNbO_3$. *Nucl. Instrum. Methods Phys. Res. B*, **250**(1-2):164–168, 2006.

[99] H. Hartung, E.-B. Kley, A. Tünnermann, T. Gischkat, F. Schrempel, and W. Wesch. Fabrication of ridge waveguides in zinc-substituted lithium niobate by means of ion-beam enhanced etching. *Opt. Lett.*, **33**(20):2320–2322, 2008.

[100] H. Hartung, E.-B. Kley, T. Gischkat, F. Schrempel, W. Wesch, and A. Tünnermann. Ultra thin high index contrast photonic crystal slabs in lithium niobate. *Opt. Mater.*, **33**(1):19–21, 2010.

[101] H. Hartung. *Mikro- und Nanostrukturierung von Lithiumniobat.* PhD thesis, Friedrich-Schiller-University Jena, Germany, 2010.

[102] Q.-Y. Tong, Q. Gan, G. Hudson, G. Fountain, and P. Enquist. Low-temperature hydrophobic silicon wafer bonding. *Appl. Phys. Lett.*, **83**:4767–4769, 2003.

[103] T. Clausnitzer, T. Kämpfe, F. Brückner, R. Heinze, E.-B. Kley, and A. Tünnermann. Reflection-reduced encapsulated transmission grating. *Opt. Lett.*, **33**(17):1972–1974, 2008.

[104] S. Pélissier, G. Pandraud, A. Mure-Ravaud, A.V. Tishchenko, and B. Biasse. Fabrication of buried corrugated waveguides by wafer direct bonding. *J. Lightwave Technol.*, **18**(4):540–545, 2000.

[105] J. Nishii, K. Kintaka, and T. Nakazawa. High-efficiency transmission gratings buried in a fused-$SiO_2$ glass plate. *Appl. Opt.*, **43**(6):1327–1330, 2004.

[106] J. S. Ye, Y. Kanamori, F.-R. Hu, and K. Hane. Narrow-band tunable optical filters using the self-suspended subwavelength grating. *J. Mod. Opt.*, **54**:827–832, 2007.

[107] B. Olbrechts, X. Zhang, Y. Bertholet, T. Pardoen, and J.-P. Raskin. Effect of

interfacial $SiO_2$ thickness for low temperature $O_2$ plasma activated wafer bonding. *Microsyst. Technol.*, **12**:383–390, 2006.

[108] S. T. S. Bukkapatnam, P. K. Rao, W.-C. Lih, N. Chandrasekaran, and R. Komanduri. Process characterization and statistical analysis of oxide CMP on a silicon wafer with sparse data. *Appl. Phys. A*, **88**:785–792, 2007.

[109] D. Fattal, J. Li, Z. Peng, M. Fiorentino, and R. G. Beausoleil. Flat dielectric grating reflectors with focusing abilities. *Nature Phot.*, **4**:466–470, 2010.

[110] F. Lu, F. G. Sedgwick, V. Karagodsky, C. Chase, and C. J. Chang-Hasnain. Planar high-numerical-aperture low-loss focusing reflectors and lenses using subwavelength high contrast gratings. *Opt. Express*, **18**(12):12606–12614, 2010.

[111] K. Numata, M. Ando, K. Yamamoto, S. Otsuka, and K. Tsubono. Wide-band direct measurement of thermal fluctuations in an interferometer. *Phys. Rev. Lett.*, **91**(26):260602, 2003.

[112] K. Somiya and K. Yamamoto. Coating thermal noise of a finite-size cylindrical mirror. *Phys. Rev. D*, **79**(10):102004, 2009.

# Acknowledgements

This thesis arose out of years of research that has been done since I came to the Microstructure Technology/Microoptics group of Dr. Ernst-Bernhard Kley at the Institute of Applied Physics led by Prof. Andreas Tünnermann. By that time, I have worked with a great number of people whose contribution in assorted ways to the research and the making of the thesis deserved special mention. It is a pleasure to convey my gratitude to them all in my humble acknowledgment.

In the first place I would like to record my gratitude to Dr. **Ernst-Bernhard Kley** for his supervision, advice, and guidance from the very early stage of this research as well as giving me extraordinary experiences through out the work whilst allowing me the room to work in my own way. Above all and the most needed, he provided me unflinching encouragement and support in various ways. His truly scientist intuition has made him as a constant oasis of ideas.

My special thanks go to the head of the Institute of Applied Physics of the Friedrich-Schiller University Jena, Prof. **Andreas Tünnermann** for his substantial contribution to a highly inspiring and eminently respected research environment as can be found at the Institute of Applied Physics, and for giving me the opportunity to work on such a challenging research project.

I gratefully acknowledge Prof. **Roman Schnabel** from the University of Hanover for his advice, supervision, and crucial contribution, which made him a major backbone of this research and so to this thesis. I am much indebted to him for his zealous support in publishing the results of this thesis.

It is my deep pleasure to thank Dr. **Tina Clausnitzer**. I will always be thankful for her inspiration, support and honest concerns. The progression of this thesis benefited notably

from her experience and enthusiastic interest in the topic of diffraction gratings. She was a fantastic colleague, but moreover, she became a really good friend.

I would also like to acknowledge my project co-workers **Stefanie Kroker, Daniel Friedrich, Michael Britzger**, and Dr. **Ronny Nawrodt** for their advice and their willingness to share their bright thoughts with me, which were very fruitful for shaping up my ideas and research as well as this thesis. In particular, I thank Daniel Friedrich for being such a reliable and pleasant project companion working hard for our research progress, and for carrying out the cavity measurements at the University of Hanover, Germany.

Collective and individual acknowledgments are also owed to all my colleagues of the Microstructure Technology/Microoptics group for giving me such a pleasant time and warm atmosphere when working together with them. Especially, I enjoyed the daily lunch time giving also room for interchange of nonphysical ideas.

I convey special acknowledgement to **Thomas Käsebier** and all members of the group's technical staff for their indispensable work on fabricating the grating samples. Without their wide expertise and active collaboration the success of this work would have been impossible. Over the years, Thomas Käsebier has probably spent several days on etching my gratings which would never have been existed without him. Thank you, Thomas!

Many thanks go to all the staff at the Institute of Applied Physics, especially to **Bodo Martin** and Dr. **Holger Hartung** for their assistance with technical problems - at all times.

Words fail me to express my appreciation to my wife **Maria** whose dedication, love and persistent confidence in me, has extraordinarily contributed to the accomplishment of my thesis. I gratefully thank **my parents** for their understanding, endless patience and encouragement when it was most required. It is my pleasure to thank my brother's father in law **Steve** for kindly reviewing my thesis in terms of grammar and spelling.

Finally, I would like to thank everybody who was important to the successful realization of this thesis, as well as expressing my apology that I could not mention personally one by one.

# Zusammenfassung

In den vergangenen Jahren hat sich ein großes wissenschaftliches Interesse an hochempfindlichen opto-mechanischen Systemen entwickelt, bei denen eine Lichtwelle über den Lichtdruck mit einem mechanischen Oszillator gekoppelt wird [1–6]. Dieser wird in der Regel durch einen hochreflektierenden Spiegel in einem optischen Hochfinesse-Resonator realisiert. Beispielsweise dienen solche Spiegel als Testmassen für die interferometrische Gravitationswellendetektion [6, 7], als Oszillatoren für die Untersuchung des Quantencharakters makroskopischer Körper [4, 8–10] und als wichtigste Bausteine für hochstabile Referenzresonatoren sowie hochpräzise optische Uhren zur Erforschung der Natur fundamentaler Konstanten [11–14]. Die Messempfindlichkeit solcher Experimente wird fundamental durch verschiedenste Rauscheinflüsse begrenzt, die sich dem gewünschten Messsignal überlagern [15–17]. Einen entscheidenden Anteil des thermischen Rauschens liefern hierbei die dielektrischen Vielschichtsysteme, die in den derzeitigen Aufbauten die hohen Reflektivitäten der Resonatorspiegel gewährleisten. Das hohe Rauschniveau der Schichtsysteme resultiert zum einen aus den hohen mechanischen Verlusten der alternierenden amorphen Schichtmaterialien und der damit verbundenen Energiedissipation und zum anderen aus der Herabsetzung der hohen mechanischen Güten der Spiegelsubstratmaterialien wie z.B. Kieselglas oder Silizium [15, 21–24]. Es skaliert dabei mit der Dicke der dielektrischen Beschichtung, die typischerweise 5 bis 7 $\mu$m beträgt [21].

Neben der Erforschung der Verlustmechanismen der Beschichtungsmaterialien mit dem Ziel der Reduzierung der mechanischen Verluste [25–27] sind veränderte bzw. alternative Spiegelkonzepte von großem Interesse, die die benötigte Dicke einer dielektrischen Beschichtung stark verringern oder diese gar gänzlich vermeiden. Einen viel versprechenden Ansatz bieten dabei sogenannte resonante Wellenleitergitter (RWG), welche mit Hilfe einer mikrostrukturierten hochbrechenden Schicht (mit einer typischen Dicke von wenigen

Hundert Nanometern) auf einem niedrigbrechenden Substrat hohe Reflektivitäten erreichen können [34–37]. Solche Strukturen wurden erstmals durch Bunkowski *et al.* für die Anwendung im Bereich der Hochpräzisions-Metrologie vorgeschlagen [38]; zuvor wurden diese hauptsächlich für die Funktion als optischer Filter oder Schalter untersucht [35].

Im Rahmen dieser Arbeit wurde das Potenzial dieser Gitterstrukturen im Hinblick auf die Realisierung maximaler Reflektivitäten bei gleichzeitiger Minimierung der dielektrischen Beschichtung erstmals experimentell untersucht. Dazu wurde zunächst ein RWG realisiert, das eine 400 nm dünne strukturierte Tantalpentoxid-Schicht auf einem Siliziumdioxidsubstrat aufwies. Die Material-Wellenlänge-Auswahl wurde hierbei an die derzeitige Generation an optischen Hochpräzisions-Experimenten angepasst. Das Gitter wurde als Einkoppelspiegel in einem Hochfinesse-Resonator charakterisiert, von deren Finesse-Wert eine Reflektivität von 99,08 % bei einer Arbeitswellenlänge des Lichtes von 1064 nm abgeleitet werden konnte [39]. Die erreichte Reflektivität stellt einen Rekordwert für resonante Reflexion bei 1064 nm dar. Außerdem wurde nie zuvor ein Hochfinesse-Resonator zur Bestimmung einer gitterbasierten Reflektivtät eingesetzt.

Den jüngsten Erkenntnissen auf dem Gebiet der Materialforschung folgend wurden des Weiteren siliziumbasierte RWGs sowohl theoretisch modelliert als auch experimentell demonstriert. Silizium wird aufgrund besserer mechanischer Eigenschaften als Kieselglas, speziell bei kryogenen Temperaturen, mit größter Wahrscheinlichkeit das Basismaterial zukünftiger Hochpräzisions-Aufbauten sein [40,41]. Die spektrale Reflektivität unter senkrechter Inzidenz ergab für ein hergestelltes Gitter einen Wert von größer 98 % für einen breiten Wellenlängenbereich von 1,52 $\mu$m bis 1,59 $\mu$m. Der Spitzenwert bei der Arbeitswellenlänge von 1,55 $\mu$m lag bei 98,9 %.

Obwohl die genannten RWGs die dielektrischen Beschichtungen erheblich reduzieren, ist mindestens noch eine Schicht aus einem substratfremden Material erforderlich, die ungewünschte mechanische Verluste induziert [24]. Vor diesem Hintergrund wurde im Rahmen dieser Arbeit ein völlig neuer Ansatz der Mikrostrukturierung einer dielektrischen Oberfläche entwickelt, der vollständig auf eine Beschichtung verzichtet und damit eine rein monolithische Implementierung resonanter Wellenleitergitter darstellt [44]. Die mechanische Güte des Substrats wird durch die Mikrostruktur nur minimal gestört [24]. Die notwendige Strukturierung der Oberfläche resultiert dabei in T-förmigen Stegen eines

Subwellenlängengitters und erreicht eine theoretische Reflektivität von 100 % [45]. Aufbauend auf der rigorosen Modellierung dieser Oberflächenstruktur wurde ein Demonstrator in Silizium experimentell realisiert [46]. Dieser wurde als Endspiegel ebenfalls in einen Hochfinesse-Resonator eingebaut. Die Finesse dieses Resonators wurde zu $F = 2784 \pm 100$ bestimmt, was einer Gitterreflektivität von (99,7945 ± 0,0086) % entspricht. Dies ist die höchste jemals erreichte auf resonanter Lichtkopplung basierende Reflektivität. Sie ermöglicht im Prinzip einen beschichtungsfreien Resonator mit einer Finesse von $\approx 1500$, welche den Finesse-Werten von derzeitigen Gravitationswellendetektoren entspricht. Diese Ergebnisse können als die wichtigste Errungenschaft dieser Arbeit angesehen werden. Der Resonatoraufbau spiegelt zudem die Ausgestaltung zukünftiger Experimente wider.

Mit dem Ziel einer praktikableren Handhabung wurde des Weiteren ein zweiter Ansatz für eine monolithische Implementierung von RWGs erarbeitet [47, 48]. Dieser beruht auf einem vergrabenen Subwellenlängengitter und liefert damit eine flache und robuste Gitteroberfläche. Das Gitter ist damit vor Kontamination und schneller Zerstörung geschützt. Zudem können zusätzliche Technologien für die Herstellung eingesetzt werden. Die theoretischen Betrachtungen zeigten auch hier, dass eine Reflektivität von 100 % möglich ist. Eine erste experimentelle Realisierung gelang wiederum in Silizium, wobei eine viel versprechende Reflektivität von 93 % unter senkrechter Inzidenz bei einer Wellenlänge von $\lambda = 1550\,\mathrm{nm}$ gemessen werden konnte.

Basierend auf dem derzeitigen Verständnis von beschichtungsinduziertem thermischen Rauschen stellen die im Rahmen dieser Arbeit entwickelten Ansätze mögliche Lösungen der oben beschriebenen Problematik in Aussicht. Nichtsdestotrotz müssen die gitterbasierten Reflektivitäten durch weitere Technologieentwicklung weiter erhöht werden. Im Hinblick auf einen Einsatz unter kryogenen Bedingungen muss hierbei auch die Temperaturabhängigkeit der optischen Parameter berücksichtigt werden. Auch ein direkter experimenteller Nachweis der Reduzierung des thermischen Rauschens der entwickelten Strukturen gegenüber herkömmlicher Spiegel ist geplant. In Anbetracht der viel versprechenden Ergebnisse und dem vorhergesehenen Fortschritt eröffnet diese Arbeit dennoch einen Weg zu einer neuen Generation von hochempfindlichen Experimenten zur Erforschung fundamentaler Fragen der modernen Physik.

# Publications in peer-reviewed journals

[1] F. Brückner, E.-B. Kley, and T. Clausnitzer. Monolithischer dielektrischer Spiegel. *German Patent Application*, DE 10 2007 047 681.9, 2007. Bibliography item [44]

[2] F. Brückner, T. Clausnitzer, O. Burmeister, D. Friedrich, E.-B. Kley, K. Danzmann, A. Tünnermann, and R. Schnabel. Monolithic dielectric surfaces as new low-loss light-matter interfaces. *Opt. Lett.*, **33**(3):264–266, 2008. Bibliography item [45]

[3] T. Clausnitzer, T. Kämpfe, F. Brückner, R. Heinze, E.-B. Kley, and A. Tünnermann. Reflection-reduced encapsulated transmission grating. *Opt. Lett.*, **33**(17):1972–1974, 2008. Bibliography item [103]

[4] F. Brückner, D. Friedrich, T. Clausnitzer, O. Burmeister, M. Britzger, E.-B. Kley, K. Danzmann, A. Tünnermann, and R. Schnabel. Demonstration of a cavity coupler based on a resonant waveguide grating. *Opt. Express*, **17**(1):163–169, 2009. Bibliography item [39]

[5] M. P. Edgar, B. W. Barr, J. Nelson, M. V. Plissi, K. A. Strain, O. Burmeister, M. Britzger, K. Danzmann, R. Schnabel, T. Clausnitzer, F. Brückner, E.-B. Kley , and A. Tünnermann. Experimental demonstration of a suspended diffractively coupled optical cavity. *Opt. Lett.*, **34**(20):3184–3186, 2009.

[6] C. Wirth, O. Schmidt, I. Tsybin, T. Schreiber, T. Peschel, F. Brückner, T. Clausnitzer, J. Limpert, R. Eberhardt, A. Tünnermann, M. Gowin, E. ten Have, K. Ludewigt, and M. Jung. 2 kW incoherent beam combining of four narrow-linewidth photonic crystal fiber amplifiers. *Opt. Express*, **17**(3):1178–1183, 2009.

[7] F. Brückner, D. Friedrich, M. Britzger, T. Clausnitzer, O. Burmeister, E.-B. Kley, K. Danzmann, A. Tünnermann, and R. Schnabel. Encapsulated subwavelength grating as a quasi-monolithic resonant reflector. *Opt. Express*, **17**(26):24334–24341, 2009.

Bibliography item [47]

[8] T. Schreiber, C. Wirth, O. Schmidt, T. V. Andersen, I. Tsybin, S. Böhme, T. Peschel, F. Brückner, T. Clausnitzer, F. Röser, R. Eberhardt, J. Limpert, and A. Tünnermann. Incoherent Beam Combining of Continuous-Wave and Pulsed Yb-Doped Fiber Amplifiers. *IEEE J. Sel. Topics Quantum Electron.*, **15**(2):354–360, 2009.

[9] F. Brückner, D. Friedrich, T. Clausnitzer, M. Britzger, O. Burmeister, K. Danzmann, E.-B. Kley, A. Tünnermann, and R. Schnabel. Realization of a Monolithic High-Reflectivity Cavity Mirror from a Single Silicon Crystal. *Phys. Rev. Lett.*, **104**(16):163903, 2010. Bibliography item [46]

[10] R. Schnabel, M. Britzger, F. Brückner, O. Burmeister, K. Danzmann, J. Dück, T. Eberle, D. Friedrich, H. Lück, M. Mehmet, R. Nawrodt, S. Steinlechner, and B. Willke. Building blocks for future detectors: Silicon test masses and 1550 nm laser light. *J. Physics: Conf. Ser.*, **228**:012029, 2010. Bibliography item [41]

[11] M. P. Edgar, B. W. Barr, J. Nelson, M. V. Plissi, K. A. Strain, O. Burmeister, M. Britzger, K. Danzmann, R. Schnabel, T. Clausnitzer, F. Brückner, E.-B. Kley, and A. Tünnermann. Experimental demonstration of a suspended, diffractively coupled Fabry-Perot cavity. *Class. Quantum Grav.*, **27**(8):084029, 2010.

[12] O. Burmeister, M. Britzger, A. Thüring, D. Friedrich, F. Brückner, K. Danzmann, and R. Schnabel. All-reflective coupling of two optical cavities with 3-port diffraction gratings. *Opt. Express*, **18**(9):9119–9132, 2010.

[13] F. Brückner, S. Kroker, D. Friedrich, E.-B. Kley, and A. Tünnermann. Widely tunable monolithic narrowband grating filter for near-infrared radiation. *Opt. Lett.*, **36**(4):436–438, 2011. Bibliography item [48]

[14] S. Kroker, F. Brückner, M. Britzger, D. Friedrich, K. Danzmann, E.-B. Kley, R. Schnabel, and A. Tünnermann. Enhanced angular tolerance of resonant waveguide grating reflectors. *Opt. Lett.*, **36**(4):537–539, 2011.

[15] R. Nawrodt, C. Schwarz, S. Kroker, I. W. Martin, F. Brückner, L. Cunningham, V. Große, A. Grib, D. Heinert, J. Hough, T. Käsebier, E.-B. Kley, R. Neubert, S. Reid, S. Rowan, P. Seidel, M. Thürk, and A. Tünnermann. Investigation of mechanical

losses of thin silicon flexures at low temperatures. *arXiv*:1003.2893v1, 2010.

[16] B. W. Barr, M. P. Edgar, J. Nelson, M. V. Plissi, K. A. Strain, O. Burmeister, M. Britzger, R. Schnabel, K. Danzmann, J. Hallam, A. Freise, T. Clausnitzer, F. Brückner, E.-B. Kley, and A. Tünnermann. Translational effects in diffractively coupled optical cavities. *submitted*, 2010.

[17] M. Britzger, D. Friedrich, S. Kroker, F. Brückner, O. Burmeister, E.-B. Kley, A. Tünnermann, K. Danzmann, and R. Schnabel. Pound-Drever-Hall error signals for the length control of 3-port grating coupled cavities. *submitted*, 2010.

# Conference contributions

[18] F. Brückner, T. Clausnitzer, O. Burmeister, D. Friedrich, E.-B. Kley, K. Danzmann, A. Tünnermann, and R. Schnabel. 100% reflectivity from a monolithic dielectric microstructured surface. In *Advanced Fabrication Technologies for Micro/Nano Optics and Photonics*, edited by T. J. Suleski, W. V. Schoenfeld, J. J. Wang, Proc. SPIE **6883**:68830X, 2008.

[19] T. Clausnitzer, T. Kämpfe, F. Brückner, R. Heinze, E.-B. Kley, A. Tünnermann, O. Parriaux, and A. T. Tishchenko. Highly-dispersive dielectric transmission gratings with 100% diffraction efficiency. In *Advanced Fabrication Technologies for Micro/Nano Optics and Photonics*, edited by T. J. Suleski, W. V. Schoenfeld, J. J. Wang, Proc. SPIE **6883**:68830U, 2008.

[20] O. Schmidt, S. Klingebiel, B. Ortac, F. Röser, F. Brückner, T. Clausnitzer, E.-B. Kley, and J. Limpert, and A. Tünnermann. Spectral combining of pulsed fiber lasers: scaling considerations. In *Fiber Lasers V: Technology, Systems, and Applications*, edited by J. Broeng, C. Headley, Proc. SPIE **6873**:687317, 2008.

[21] F. Brückner, T. Clausnitzer, E.-B. Kley, and A. Tünnermann. Monolithische dielektrische mikrostrukturierte Oberfläche mit 100% Reflektivität. *DPG-Frühjahrstagung*, Darmstadt, Germany, 2008.

[22] D. Friedrich, O. Burmeister, M. Britzger, T. Clausnitzer, F. Brückner, E.-B. Kley, A. Tünnermann, K. Danzmann and R. Schnabel. High reflectivity grating waveguide coatings. *DPG-Frühjahrstagung*, Darmstadt, Germany, 2008.

[23] D. Friedrich, O. Burmeister, M. Britzger, K. Danzmann, R. Schnabel, F. Brückner, T. Clausnitzer, E.-B. Kley, and A. Tünnermann. High-reflection grating mirrors without coatings. *The Gravitational Wave Advanced Detector Workshop*, Elba, Italy,

2008.

[24] F. Brückner, T. Clausnitzer, E.-B. Kley, and A. Tünnermann. Experimentelle Realisierung einer monolithischen dielektrischen mikrostrukturierten Oberfläche mit 99,9% Reflektivität. *DPG-Frühjahrstagung*, Hamburg, Germany, 2009.

[25] F. Brückner, D. Friedrich, T. Clausnitzer, M. Britzger, E.-B. Kley, A. Tünnermann, K. Danzmann, and R. Schnabel. Demonstration of a coating-free surface with a reflectivity of 99.8%. *The 8th Edoardo Amaldi Conference on Gravitational Waves*, New York City, USA, 2009.

[26] F. Brückner, T. Clausnitzer, T. Käsebier, E.-B. Kley, and A. Tünnermann. Demonstration of a Monolithic Dielectric Microstructured Surface with a Reflectivity of 99.8%. *Proc. IEEE/LEOS Int. Conf. Opt. MEMS Nanophotonics*, ThA3, 2009.

[27] S. Kroker, F. Brückner, E.-B. Kley, and A. Tünnermann. Konzepte für diffraktive Optiken mit geringem thermischen Rauschen. *DPG-Frühjahrstagung*, Hanover, Germany, 2010.

[28] D. Friedrich, F. Brückner, M. Britzger, S. Kroker, E.-B. Kley, A. Tünnermann, K. Danzmann, and R. Schnabel. Waveguide gratings as highly reflective mirrors without dielectric coatings. *DPG-Frühjahrstagung*, Hanover, Germany, 2010.

[29] F. Brückner, D. Friedrich, T. Clausnitzer, M. Britzger, E.-B. Kley, A. Tünnermann, K. Danzmann, and R. Schnabel. Coating-free surface mirrors for GW detectors. *Einstein Telescope International Workshop*, Jena, Germany, 2010.

[30] D. Friedrich, F. Brückner, M. Britzger, S. Kroker, K. Danzmann, R. Schnabel, E.-B. Kley, and A. Tünnermann. Waveguide coatings and thermal noise. *Gravitational-Wave Advanced Detector Workshop*, Kyoto, Japan, 2010.

[31] F. Brückner, D. Friedrich, S. Kroker, M. Britzger, E.-B. Kley, A. Tünnermann, K. Danzmann, and R. Schnabel. Mirrors with waveguide surfaces to fight coating thermal noise. *Rencontres de Moriond and GPhyS Colloquium*, La Thuile, Italy, 2011.

# Erklärung

Ich erkläre hiermit ehrenwörtlich, dass ich die vorliegende Arbeit selbständig, ohne unzulässige Hilfe Dritter und ohne Benutzung anderer als der angegebenen Hilfsmittel und Literatur angefertigt habe. Die aus anderen Quellen direkt oder indirekt übernommenen Daten und Konzepte sind unter Angabe der Quellen gekennzeichnet.

Die Durchführung und Auswertung der resonatorbasierten Reflektivitätsmessungen erfolgte in enger Kooperation mit der Arbeitsgruppe von Prof. Dr. Roman Schnabel der Universität Hannover im Rahmen des deutschen Sonderforschungsbereichs Transregio 7. Die Ergebnisse dieser Experimente wurden in gemeinsamen Veröffentlichungen publiziert.

Weitere Personen waren an der inhaltlich-materiellen Erstellung der vorliegenden Arbeit nicht beteiligt. Insbesondere habe ich hierfür nicht die entgeltliche Hilfe von Vermittlungs- bzw. Beratungsdiensten (Promotionsberater oder andere Personen) in Anspruch genommen. Niemand hat von mir unmittelbar oder mittelbar geldwerte Leistungen für Arbeiten erhalten, die im Zusammenhang mit dem Inhalt der vorgelegten Dissertation stehen.

Die Arbeit wurde bisher weder im In- noch im Ausland in gleicher oder ähnlicher Form einer anderen Prüfungsbehörde vorgelegt.

Teile dieser Arbeit wurden aus Prioritätsgründen bereits veröffentlicht oder wurden zur Veröffentlichung eingereicht.

Die geltende Promotionsordnung der Physikalisch-Astronomischen Fakultät ist mir bekannt. Ich versichere ehrenwörtlich, dass ich nach bestem Wissen die reine Wahrheit gesagt und nichts verschwiegen habe.

Jena, den 3. März 2011 ..................

Frank Brückner

# Lebenlauf

## Persönliche Daten

| | |
|---|---|
| Vorname | Frank |
| Name | Brückner |
| Geburtsdatum | 21.08.1981 |
| Geburtsort | Dresden |

## Ausbildung

| | |
|---|---|
| 1988 - 1990 | Grundschule Heilbad Heiligenstadt |
| 1992 - 2000 | Staatliches Gymnasium Johann-Georg-Lingemann Heilbad Heiligenstadt |
| 30.06.2000 | Abitur am Gymnasium Heilbad Heiligenstadt |
| 2001 - 2006 | Studium der Physik an der Friedrich-Schiller-Universität Jena |
| 2005 - 2006 | Diplomarbeit am Institut für Angewandte Physik der Friedrich-Schiller-Universität Jena |
| 18.12.2006 | Abschluss als Diplom-Physiker |

## Berufliche Tätigkeit

| | |
|---|---|
| 2000 - 2001 | Zivildienst |
| 2007 - 2011 | Doktorand am Institut für Angewandte Physik der Friedrich-Schiller-Universität Jena |
| 08.02.2011 | Abschluss als Dr. rer. nat. |

Jena, den 3. März 2011

..................

Frank Brückner